Jagiellonian University
Faculty of Physics, Astronomy and Applied Computer Science

Digital Pulse Shape Analysis with Neural Networks: Application to Flow Measurements in the ASY-EOS Experiment

Sebastian Kupny

PhD thesis written under the supervision of
dr hab. Janusz Brzychczyk
and co-supervision of dr Jerzy Łukasik

Cracow, 2016

Wydział Fizyki, Astronomii i Informatyki Stosowanej
Uniwersytet Jagielloński

Oświadczenie

Ja niżej podpisany *Sebastian Kupny* (nr indeksu: 1068418) doktorant Wydziału Fizyki, Astronomii i Informatyki Stosowanej Uniwersytetu Jagiellońskiego oświadczam, że przedłożona przeze mnie rozprawa doktorska pt. "Digital Pulse Shape Analysis with Neural Networks: Application to Flow Measurements in the ASY-EOS Experiment" jest oryginalna i przedstawia wyniki badań wykonanych przeze mnie osobiście, pod kierunkiem dr. hab. Janusza Brzychczyka. Pracę napisałem samodzielnie.

Oświadczam, że moja rozprawa doktorska została opracowana zgodnie z Ustawą o prawie autorskim i prawach pokrewnych z dnia 4 lutego 1994 r. (Dziennik Ustaw 1994 nr 24 poz. 83 wraz z późniejszymi zmianami).

Jestem świadom, że niezgodność niniejszego oświadczenia z prawdą ujawniona w dowolnym czasie, niezależnie od skutków prawnych wynikających z ww. ustawy, może spowodować unieważnienie stopnia nabytego na podstawie tej rozprawy.

Kraków, dnia 08.03.2016

.....
podpis doktoranta

Abstract

This work is devoted to the development of digital pulse shape analysis methods, including neural networks, for particle identification and background suppression, required for the analysis of experimental data provided by the KRATTA multi-detector system. The KRATTA detector was used in the ASY-EOS experiment conducted at the Heavy-Ion-Synchrotron SIS18 at the GSI laboratory in 2011. The experiment was dedicated to the study of the symmetry energy term in the nuclear equation of state (NEOS) at supra-saturation densities which is essential for understanding many aspects of nuclear physics and astrophysics. The collective flows of neutrons and light charged particles, measured with the Large Area Neutron Detector (LAND), are known to be sensitive probes of the symmetry energy. The measurements were performed for ^{197}Au+^{197}Au, ^{96}Ru+^{96}Ru, and ^{96}Zr+^{96}Zr collisions at incident energies of 400 MeV/nucleon. KRATTA was included in the setup for providing information on charged particle yields and flows with higher precision than available with LAND.

The KRATTA detector array consists of triple telescope modules with large-area silicon photodiodes and CsI(Tl) scintillation crystals. In this system a novel detection method was used, which exploits a single silicon chip (photodiode) for both ΔE measurement and scintillation light collection. The multi-component signals from photodiodes were digitized and stored for further off-line analysis. The application of complex detection techniques required the development of adequate digital pulse shape analysis methods, which was realized in this work. In particular, the work was focused on the important problem of recognition of background events in KRATTA modules. The developed fast and efficient background recognition method was based on a self-organizing neural network.

The elaborate data analysis procedures allowed obtaining the first experimental KRATTA results for the ^{197}Au+^{197}Au reaction. The directed and elliptic flows of light charged particles were found to agree with previously obtained results of the FOPI collaboration. It supports the soft nature of the symmetric-matter NEOS that was deduced from the FOPI data set. The provided precise experimental data are expected to aid in the development and test of transport theories required for the interpretation of the symmetry energy observables, and in particular for resolving existing ambiguities regarding the role of the nuclear effective mass and momentum dependent forces in the reaction process. Initial comparisons between the experimental results and the results of calculations performed with the UrQMD model showed a significant disagreement in the isobaric t/^{3}He yield ratio, indicating the need of improvements for the model.

From the analysis of the LAND data for the ^{197}Au+^{197}Au system, the elliptic flow ratio of neutrons versus charged particles was determined. Based on the comparison with UrQMD predictions, a new constraint for the symmetry energy at supra-saturation densities was obtained, indicating a moderately soft density dependence of the symmetry energy.

Streszczenie

Głównym zadaniem niniejszej pracy było opracowanie metod cyfrowej analizy kształtu impulsu z wykorzystaniem sieci neuronowych do identyfikacji cząstek i redukcji tła, niezbędnych do analizy danych eksperymentalnych dostarczanych przez system detekcyjny KRATTA. Detektor KRATTA został zastosowany w eksperymencie ASY-EOS przeprowadzonym w ośrodku badawczym GSI w 2011 roku. Eksperyment ten miał na celu uzyskanie informacji o energii symetrii w równaniu stanu materii jądrowej (NEOS) przy dużych gęstościach, mającej kluczowe znaczenie dla zrozumienia wielu aspektów fizyki jądrowej i astrofizyki. Kolektywne pływy neutronów i lekkich cząstek naładowanych, mierzone w eksperymencie przez detektor LAND, stanowią obserwable pozwalające wnioskować o wartościach energii symetrii. Pomiary przeprowadzono dla reakcji ^{197}Au+^{197}Au, ^{96}Ru+^{96}Ru, and ^{96}Zr+^{96}Zr przy energiach wiązki 400 MeV/nukleon. Zadaniem detektora KRATTA był pomiar lekkich cząstek naładowanych z precyzją znacznie większą od tej, jaką można uzyskać w pomiarach detektorem LAND.

System detektorowy KRATTA składa się z potrójnych teleskopów półprzewodnikowo-scyntylacyjnych zbudowanych z fotodiod o dużej powierzchni aktywnej i kryształów CsI(Tl). Zastosowana została innowacyjna technika detekcyjna, w której fotodioda pełni rolę przelotowego dektora krzemowego i jednocześnie rejestruje światło ze scyntylatora. Sygnały generowane przez fotodiody były rejestrowane w formie cyfrowej z przeznaczeniem do dalszej analizy. Wprowadzona zaawansowana technika detekcyjna wymagała opracowania odpowiednich metod analizy danych, co zostało wykonane w ramach niniejszej pracy. Szczególnie istotnym zagadnieniem było rozpoznawanie sygnałów tła pochodzących od wtórnych reakcji w materiale detektora. W tym celu opracowana została efektywna metoda bazująca na samoorganizującej sieci neuronowej, charakteryzująca się dużą szybkością obliczeń oraz możliwością bezpośredniego analizowania zarejestrowanych sygnałów.

Opracowane procedury analizy danych pozwoliły otrzymać pierwsze wyniki pomiarowe dla reakcji ^{197}Au+^{197}Au. Wyznaczone parametry pływu kierunkowego i eliptycznego dla cząstek naładowanych wykazują dobrą zgodność z wcześniejszymi rezultatami otrzymanymi z eksperymentu FOPI, potwierdzając wniosek o miękkiej charakterystyce równania stanu symetrycznej materii jądrowej. Otrzymane precyzyjne dane eksperymentalne mogą zostać wykorzystane do weryfikacji przewidywań modeli teoretycznych niezbędnych do interpretacji danych i uzyskania informacji o energii symetrii. Przeprowadzone wstępne porównania z wynikami obliczeń wykonanych przy użyciu modelu UrQMD pokazały znaczne rozbieżności dla stosunków izotopowych, wskazując na konieczność dalszego rozwoju modelu, a w szczególności metody identyfikacji klastrów.

Dane pomiarowe dla reakcji ^{197}Au+^{197}Au otrzymane przy pomocy detektora LAND pozwoliły określić pływ eliptyczny neutronów w relacji do pływu eliptycznego cząstek naładowanych. Na podstawie porównań z przewidywaniami modelu UrQMD wyznaczone zostało nowe ograniczenie na zależność części potencjalnej energii symetrii od gęstości, scharakteryzowane zależnością potęgową z wykładnikiem około 0.75.

Contents

Nomenclature

ANN Artificial Neural Network

ATOF ALADIN Time-of-Flight (Wall)

BMU Best Matching Unit

CHIMERA Charged Ion Mass and Energy Resolving Array

FAIR Facility for Antiproton and Ion Research

FPGA Field-Programmable Gate Array

GSI Gesellschaft für Schwerionenforschung

KRATTA KRAków Triple Telescope Array

LAND Large Area Neutron Detector

LCP Light Charged Particles

LVQ Learning Vector Quantization

MLP Multilayer Perceptron

NEOS Nuclear Equation of State

PSA Pulse Shape Analysis

SCT Single Chip Telescope

SOM Self-Organizing Map

STR Signal to Total Ratio

UrQMD Ultrarelativistic Quantum Molecular Dynamics (model)

Chapter 1

Introduction

The study of the nuclear equation of state (NEOS) is one of the major goals of research in nuclear physics. In recent years, great attention has been paid to the NEOS of isospin asymmetric nuclear matter, in particular the nuclear symmetry energy. The knowledge of the density dependent symmetry energy is essential for understanding many aspects of nuclear physics and astrophysics. The symmetry energy governs important properties of nuclei such as the structure of neutron-rich nuclei, their masses, drip lines, neutron skins, the neutron-proton pairing energy, giant and pygmy resonances, as well as it influences the dynamics of heavy-ion collisions, isospin diffusion and multifragmentation processes [1–5]. The density dependence of the symmetry energy is also crucial in the astrophysical models of neutron stars, supernova explosions and stellar nucleosynthesis [6–11]. Although significant progress has been made in constraining the symmetry energy around and below the saturation density [3, 12], it remains largely uncertain at supra-saturation densities which are relevant to neutron stars.

Near-relativistic heavy-ion collisions are the only means to study the symmetry energy at high densities in the laboratory. For this purpose, the ASY-EOS experiment has been proposed and carried out at the GSI laboratory in May 2011 [13, 14]. The flows of neutrons and light charged particles, which are expected to be sensitive probes of the symmetry energy, were measured for the ^{197}Au+^{197}Au, ^{96}Ru+^{96}Ru and ^{96}Zr+^{96}Zr reactions at 400 MeV/nucleon incident energies. The Large Area Neutron Detector (LAND) was used for the detection of neutrons and light charged particles. The KRATTA telescope array measured the isotopic composition and flow of light charged particles with a much better resolution than is achievable with LAND. The CHIMERA multidetector, the ALADIN Time-of-Flight Wall and the Washington-University μ-Ball scintillator array were used for the event characterization and reaction plane reconstruction.

The KRAków Triple Telescope Array KRATTA [15] is a broad-energy-range detection system for light charged particles, which was designed and built for the needs of the ASY-EOS experiment. Each KRATTA telescope module consists of two CsI(Tl) scintillation crystals read out by large area photodiodes. This system uses a novel detection method exploiting a single silicon chip (photodiode) for both ΔE measurement and scintillation light collection ("single-chip telescope"). An additional third photodiode placed in front of the crystals, serves as a ΔE silicon detector allowing to lower the identification threshold. The multi-component signals from photodiodes were digitized and stored for further off-line analysis.

The application of complex detection techniques, such as the single-chip telescope, required the development of adequate digital pulse shape analysis methods, which was the main objective of the research presented in this thesis. In particular, this work was focused on the

important problem of recognition of background events in KRATTA modules. In order to maximize the detection energy range, the CsI crystals are altogether 15 cm long, which causes substantial background, mainly due to secondary reactions and scatterings in these crystals. The proposed fast and efficient background recognition method is based on a self-organizing neural network. The detection efficiency which is largely affected by the loss of events due to the secondary reactions, was determined by means of Monte Carlo simulations.

The elaborate data analysis procedures allowed obtaining the first experimental KRATTA results concerning the isotopic yields and flow parameters of light charged particles, and subsequently making comparisons with transport model calculations. The results reported in this thesis refer exclusively to the ^{197}Au+^{197}Au reaction whose analysis has been completed.

This thesis is organized as follows.

Chapters 2 and 3 contain introductory information on the nuclear symmetry energy and the present status of theoretical and experimental investigations of the density dependence of the symmetry energy. The ASY-EOS experiment is presented in Chapter 4. The description of the KRATTA detector and its associated electronics is given in Chapter 5. Chapter 6 is devoted to the KRATTA data processing with the digital pulse shape analysis providing the isotope identification and energy calibration. The method developed for background reduction with the use of self-organizing neural networks is described and discussed in Chapter 7. This chapter is preceded by a brief introduction to artificial neural networks and their applications to pulse shape analysis. The determination of the KRATTA detection efficiency, based on performing Monte Carlo simulations with Geant4, is the subject of Chapter 8. The experimental estimates of global event characteristics such as the impact parameter and the reaction plane orientation are presented in Chapter 9. The method of recognition and rejection of non-target events is explained in Chapter 10. The results of the KRATTA measurements of the energy spectra, isotopic ratios and collective flows of light charged particles are given in Chapter 11, and compared with UrQMD model calculations in Chapter 12. Chapter 13 includes a brief description of results obtained from the flow analysis of the neutron data measured with LAND. Chapter 14 summarizes the results of the performed research and provides some prospects for future investigations. The KRATTA data analysis procedures have been implemented into the Asyeosroot framework which is described in the Appendix.

Chapter 2

Nuclear Equation of State and symmetry energy

The nuclear equation of state (NEOS) describes the relationship between energy, temperature, density and isospin asymmetry in nuclear matter which is an idealized infinite system consisting of protons and neutrons interacting only through the strong nuclear force. One of the most important ingredients of the NEOS is the density dependent symmetry energy that determines the basic properties of isospin-asymmetric nuclear systems, e.g. neutron stars.

The energy related to the neutron-proton (isospin) asymmetry was first introduced in 1935 by Weizsäcker [16] and in the present form by Bethe [17] as a part of the well known semi-empirical mass formula. This formula describes the ground state energy, E, of a nucleus with respect to the sum of the masses of the constituents as a function of the number of protons (atomic number), Z, the number of neutrons, N, and the mass number $A = Z + N$:

$$E(A, Z) = -a_V A + a_S A^{2/3} + a_C Z(Z-1)A^{-1/3} + a_{sym}(N-Z)^2/A + ... \qquad (2.1)$$

with the determined empirically parameters: $a_V = 15.835$, $a_S = 18.33$, $a_C = 0.714$, and $a_{sym} = 23.2$, all in the units of MeV. This formula is based on the liquid drop model. The first, volume term, is proportional to the number of nucleons, which arises from the short-range nature of nuclear forces leading to their saturation. The second term accounts for the presence of a surface at which nucleons have less neighbors and are loosely bound. The third (Coulomb) term represents the Coulomb repulsion of protons in the nucleus. The fourth term takes into account the neutron-proton asymmetry and is called the symmetry term. The Bethe-Weizsäcker's formula allows estimating the masses of nuclei with the accuracy of about 1%. Better estimates require additional terms such as the pairing, Wigner, shell correction or curvature energy terms, see e.g. [18].

The origin of the symmetry term can be understood as follows. Protons and neutrons are fermions which in the atomic nucleus can be described within a quantum mechanical approach. As a consequence of the Pauli exclusion principle, two identical fermions cannot occupy the same quantum state. It means that each energy level in a nucleus can be occupied only by two nucleons of one type, where the number two accounts for two possible spin orientations. When one considers a nucleus with a given mass number A, then for an asymmetric nucleus, e.g. assuming $N > Z$, valence neutrons will occupy higher energy levels than valence protons. The case of $A = 16$ is illustrated in Fig. 2.1. For a given number of nucleons, the asymmetry in proton and neutron numbers causes an increase of the total energy. The form of the symmetry term $\sim (N-Z)^2/A$ can be derived from a two component Fermi gas model [19].

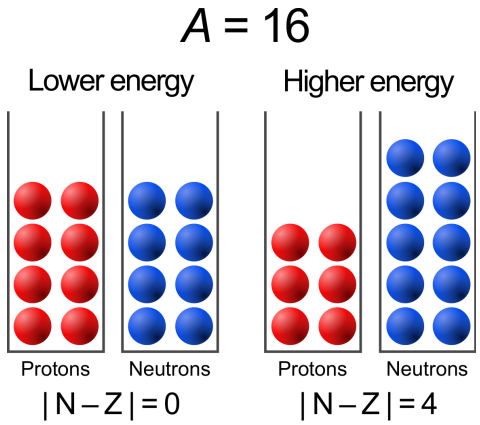

Figure 2.1: Schematic potential wells and energy levels occupied by two kinds of fermions: protons (red) and neutrons (blue) in the atomic nucleus with $A = 16$. Left side: symmetric nucleus case, right side: asymmetric case (figure taken from Wikipedia.org, licensed under the Creative Commons Attribution-Share Alike 3.0 Unported license).

After passing to the thermodynamic limit, neglecting the Coulomb interaction between protons, the energy per particle of asymmetric nuclear matter can be approximately expressed as

$$E(\rho, \delta) = E(\rho, \delta = 0) + E_{sym}(\rho)\delta^2, \tag{2.2}$$

where ρ_n and ρ_p are the neutron and proton densities, $\rho = \rho_n + \rho_p$ is the baryon density, and $\delta = \frac{\rho_n - \rho_p}{\rho_n + \rho_p}$ is the neutron-proton density asymmetry. The density dependent coefficient $E_{sym}(\rho)$ is called the symmetry energy. The quadratic form of this approximation is due to the charge symmetry of the nuclear forces. Its validity has been confirmed by theoretical calculations for a wide range of densities. The first, *isoscalar*, term refers to the energy in symmetric matter, while the second, *isovector*, term describes the increasing of the energy due to the unequal proton and neutron densities. As can be seen from Eq. 2.2, the symmetry energy can also be viewed as a difference between the energies of the pure neutron ($\delta = 1$) and of the symmetric ($\delta = 0$) nuclear matter:

$$E_{sym} = E(\rho, 1) - E(\rho, 0). \tag{2.3}$$

The above form of NEOS is applicable to cold nuclear matter ($T \simeq 0$). In the case of momentum independent interactions, the NEOS at finite temperatures can be simply obtained by modifying its kinetic part [20].

The isoscalar part of the NEOS has its minimum at the normal nuclear density $\rho_0 \simeq 0.16$ fm^{-3} with a value of about -16 MeV [21], see Fig. 2.2. This term is commonly described in terms of a Taylor expansion around the normal density. As the energy attains a minimum at normal density the first non-vanishing term corresponds to the second derivative and is usually expressed using the incompressibility parameter, K:

$$E(\rho, 0) = -a_V + \frac{K}{18}\left(\frac{\rho - \rho_0}{\rho_0}\right)^2 + ... \tag{2.4}$$

The parameter K was originally introduced to characterize the curvature of the energy with

respect to the nuclear radius:

$$K = R^2 \left.\frac{\partial^2 E}{\partial R^2}\right|_{R=R_0} = 9\rho_0^2 \left.\frac{\partial^2 E}{\partial \rho^2}\right|_{\rho=\rho_0} . \tag{2.5}$$

Analogically, the isovector term of Eq. 2.2 can be expressed as

$$E_{sym}(\rho) = E_{sym}(\rho_0) + \frac{L}{3}\left(\frac{\rho-\rho_0}{\rho_0}\right) + \frac{K_{sym}}{18}\left(\frac{\rho-\rho_0}{\rho_0}\right)^2 + ... \tag{2.6}$$

where L is the slope parameter defined as

$$L = 3\rho_0 \left.\frac{\partial E_{sym}}{\partial \rho}\right|_{\rho=\rho_0} , \tag{2.7}$$

and K_{sym} is the curvature defined similarly as K. Parameters a_V, K, $E_{sym}(\rho_0)$, L and K_{sym} are commonly used as quantities characterizing the NEOS in the vicinity of ρ_0.

Figure 2.2 presents the energy per nucleon in symmetric nuclear matter as a function of the density, assuming two versions of NEOS: soft with K=210 MeV and stiff with K=380 MeV, and also a stiff version including a transition to quark-gluon plasma at high densities [21, 22]. As can be seen, the knowledge of the incompressibility K may not be sufficient to estimate the energy at higher densities (by parabolic extrapolation) due to significant modifications arising, e.g., from a phase transition. In such a case the higher order expansion terms have to be taken into account.

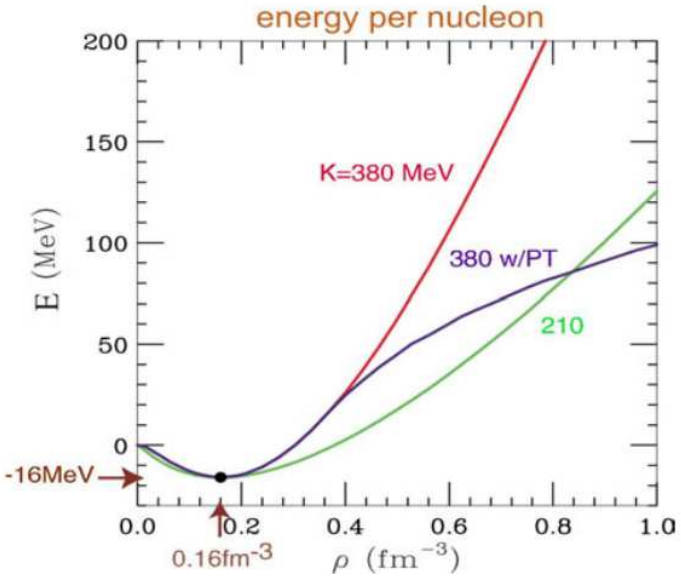

Figure 2.2: Energy per baryon versus the baryon density at $T = 0$ from a stiff NEOS (K=380 MeV), a soft NEOS (K=210 MeV), and a NEOS with a phase transition (K=380 MeV w/PT). Reprinted from [21].

The systematics of experimental results imply that the symmetric nuclear matter is soft with the incompressibility K within the range of 200 - 240 MeV. For example, the analysis of

the directed and elliptic flow measurements [23] yields the value of K between 167 and 300 MeV. The subthreshold K^+ production indicates the NEOS to be soft with $K \simeq 200$ MeV [24], see also [25] for the BQMD and [26, 27] for the IQMD analysis. The analyses of the isoscalar giant monopole resonances using the relativistic mean field (RMF) model [28] and the Skyrme Hartree-Fock (SHF) model [29] yield the values of K of about 250 and 230 MeV, respectively.

The isovector term of Eq. 2.2 is much less known. Recently, various theoretical predictions appeared for the symmetry energy, however, they give ambiguous predictions, especially in the high density region. Models which make predictions on the NEOS can be divided into three classes: phenomenological density functionals, effective-field theory (EFT) models and ab initio approaches [30]. The models belonging to the first class are based on the density dependent interactions such as Gogny or Skyrme forces or on relativistic mean-field approaches [31]. The left panel of Fig. 2.3 shows the density dependence of the symmetry energy calculated within the Skyrme Hartree-Fock approach for various parametrizations of the Skyrme interaction. All the parametrizations give similar results close to the saturation density since they were constrained to reproduce the ground state properties of stable and exotic nuclei [2]. However, as one can see, these parametrizations give completely divergent predictions at high densities. Models based on the EFT, e.g. the chiral perturbation theory, have the advantage that they have a smaller number of free parameters as compared to the phenomenological approaches. An example of the chiral perturbation theory predictions is shown in the right panel of Fig. 2.3 with the label ChPT. This figure also shows predictions of ab initio approaches: DBHF and var AV_{18} + δv+3-BF. Although such models are expected to be more precise, they also give inconsistent results at high densities. The discrepancies are due to poor knowledge of the isovector part of the in-medium nuclear interaction and to difficulties in solving the quantum nuclear many-body problem.

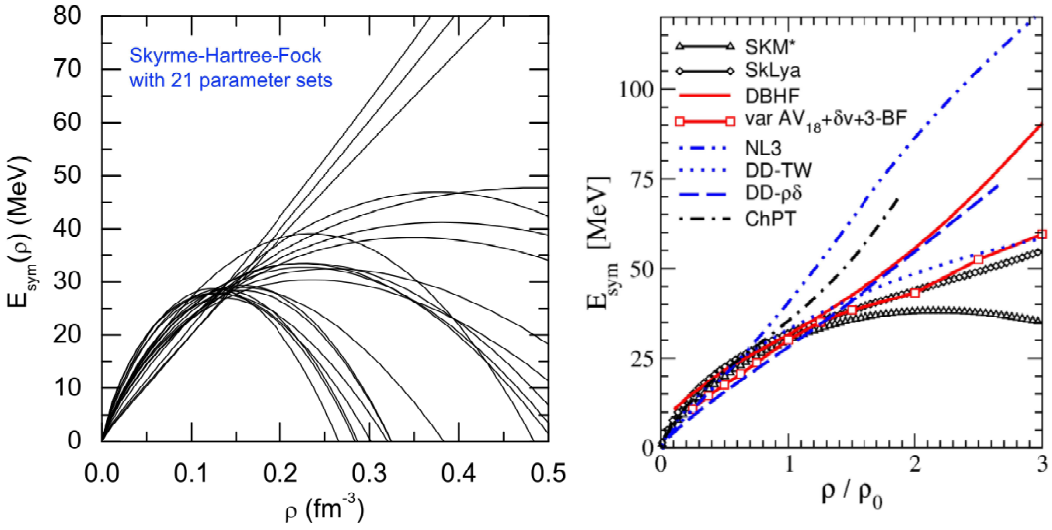

Figure 2.3: The symmetry energy as a function of density from various theoretical models. Left panel: Skyrme Hartree-Fock predictions (reprinted from [2]). Right panel: various phenomenological, microscopic and ab initio model predictions (reprinted from [30]).

In order to constrain the symmetry energy, as well as to test the validity of theoretical models, experimental data from laboratory experiments and astrophysical observations are necessary. The symmetry energy is not a directly measurable quantity and must be deduced from observables which are sensitive to it. The interpretation of experimental data is based on comparisons with model calculations assuming different parametrizations of the density-dependent symmetry energy.

So far, most of the experimental constraints have been obtained for densities near and below the saturation density $0.3\rho_0 \lesssim \rho \lesssim \rho_0$. They have been extracted from analyses of atomic masses (see, e.g., Refs. [12] and references therein), investigations of giant and pygmy dipole resonances [4, 32–34], neutron-skin thicknesses of neutron-rich nuclei [35, 36], electric dipole polarizability in ^{208}Pb [37], and heavy-ion reactions using observables such as fragment isotopic ratios, double neutron-proton ratio, isoscaling parameters, and isospin diffusion transport ratios, see, e.g., Refs. [3, 5, 38, 39]. Some constraints on the symmetry energy have also been derived from neutron star observations, such as the mass-radius relation, binding energies, r-mode instability, and torsional crust oscillations [6–8, 10, 12].

Li and Han [12] have compiled the results on the symmetry energy E_{sym} and its slope L at the normal nuclear density, deduced from various experimental data. The compilations are presented in Figs. 2.4 and 2.5. According to the recent results from laboratory experiments and from astrophysical observations, the values of $E_{sym}(\rho_0)$ and $L(\rho_0)$ fall in the ranges of 32 ± 1 MeV and 59 ± 17 MeV, respectively. The low density constraints obtained from heavy-ion collisions are shown in Fig. 2.6 as the shaded region.

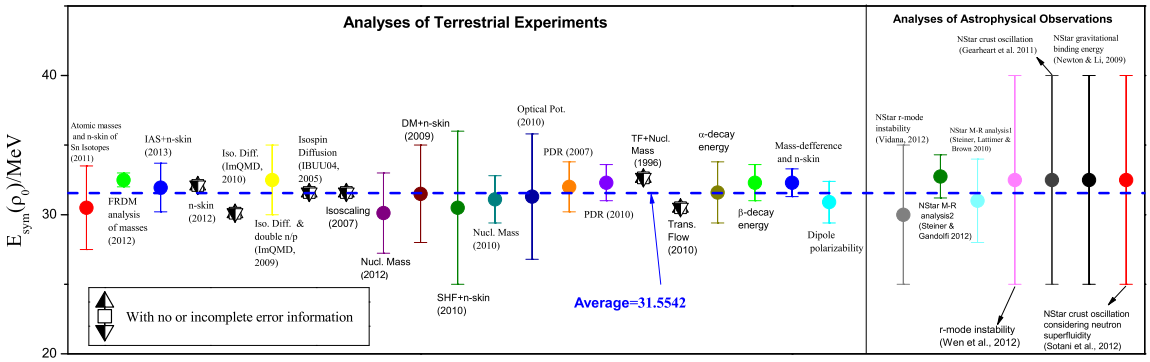

Figure 2.4: Nuclear symmetry energy at normal density from analyses of nuclear laboratory experiments and astrophysical observations. Reprinted from [12].

The information on symmetry energy at very low densities $0.01 < \rho/\rho_0 < 0.2$ has been extracted from the isoscaling analysis of light clusters emitted in heavy-ion collisions at intermediate energies [40, 41]. As it is shown in Fig. 2.7, the experimental values of E_{sym} at such ultra-low densities are much higher than those predicted by mean-field calculations which do not take into account the cluster formation. On the other hand, it has been shown that the obtained values of 8-10 MeV can be explained by quantum statistical calculations that include cluster correlations in nuclear medium and are supported by the virial equation of

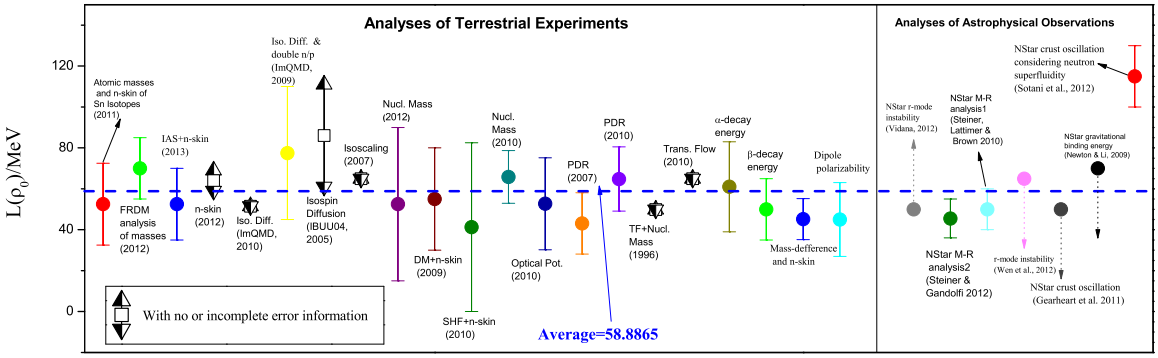

Figure 2.5: Experimental constraints on the symmetry energy slope L at normal density. Reprinted from [12].

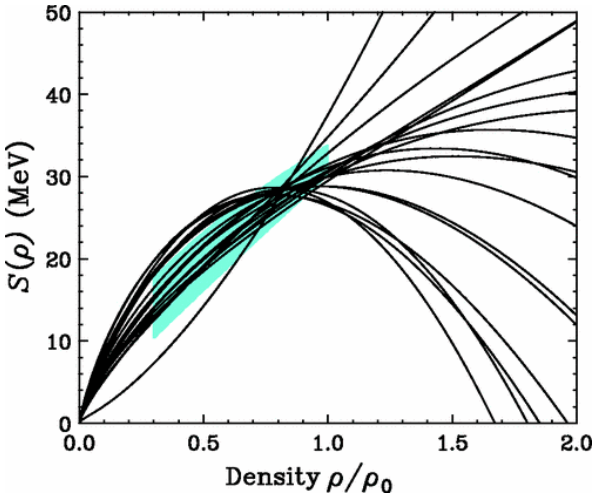

Figure 2.6: Density dependence of the symmetry energy for several Skyrme parametrizations. The shaded region is obtained from heavy-ion collision experiments. Reprinted from [3].

state obtained from nucleon-nucleon scattering phase shifts [42]. These results indicate the importance of clusterization, which causes the symmetry energy not to vanish at low densities.

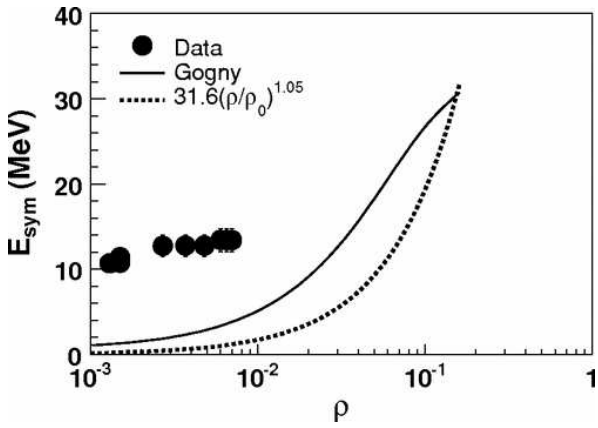

Figure 2.7: Experimental results for the symmetry energy at very low densities. The solid line indicates the result of calculations with the Gogny interaction. The dotted line represents the function $31.6(\rho/\rho_0)^{1.05}$. Reprinted from [40].

Chapter 3

Symmetry energy investigations at supra-saturation densities

The properties of the nuclear symmetry energy at high densities can only be explored in laboratories by using heavy-ion collisions of isospin asymmetric nuclei at energies ranging from several hundreds MeV to few GeV per nucleon. Transport model calculations have shown that the density of about $2\rho_0$ can be reached for a short time when the system is compressed in the early stage of such a collision. For example, Fig. 3.1 presents the average central density predicted by molecular dynamics calculations for the ^{197}Au + ^{197}Au collisions at different incident energies as a function of time. Several observables have been proposed as sensitive probes of the high density behavior of the symmetry energy, such as directed and elliptic flows of nucleons and light charged particles, neutron/proton and t/^{3}He yield ratios, π^-/π^+ ratios and flows, K^+/K^0 and Σ^-/Σ^+ ratios (see Refs. [11, 13, 23] and references therein).

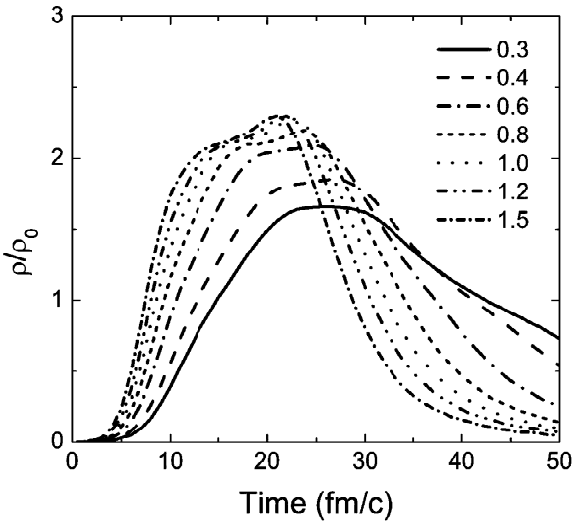

Figure 3.1: Time evolution of the average central density in Au+Au collisions at different incident energies (indicated in GeV/A), obtained from the ImIQMD model. Reprinted from [43].

Of particular interest, in the context of our studies, is the collective flow of particles emitted in the early stage of the reaction. The pattern of particle emission, observed in collisions with incident energies between about 0.1 and 4 GeV/nucleon, is visualized in Fig. 3.2. Particles emitted perpendicular to the reaction plane (squeeze-out effect), originate mainly from the hot and compressed reaction zone.

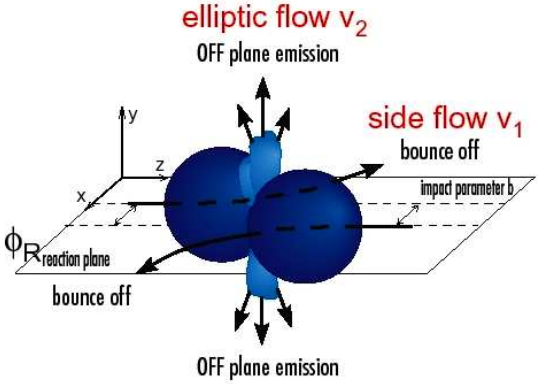

Figure 3.2: Perspective view of the in-plane bounce-off and off-plane squeeze-out of nuclear matter.

The azimuthal distribution of particles emitted from non-central collisions, measured with respect to the reaction plane orientation, can be described in terms of a Fourier expansion

$$\frac{dN}{d\left(\phi-\phi_R\right)} = \frac{N_0}{2\pi}\left(1+2\sum_{n\geqslant 1} v_n \cos n\left(\phi-\phi_R\right)\right), \tag{3.1}$$

where ϕ and ϕ_R are the azimuthal angles of the emitted particle and of the reaction plane, respectively, and v_n are the expansion coefficients. The sine terms in this expansion vanish due to the reflection symmetry with respect to the reaction plane. The first two terms v_1 - *directed flow* and v_2 - *elliptic flow* are dominant characteristics of the azimuthal distribution. The directed flow is observed at small angles to the beam direction and vanishes at midrapidity. The elliptic flow describes the most dominant modulation of the azimuthal distribution at midrapidity. These parameters depend on the particle type, rapidity y, transverse momentum p_t, and impact parameter. They can be calculated as

$$v_1(y,p_t) = \langle\cos(\phi-\phi_R)\rangle\,, \tag{3.2}$$
$$v_2(y,p_t) = \langle\cos 2(\phi-\phi_R)\rangle\,, \tag{3.3}$$

or

$$v_1(y,p_t) = \left\langle\frac{p_x}{p_t}\right\rangle, \tag{3.4}$$
$$v_2(y,p_t) = \left\langle\frac{p_x^2-p_y^2}{p_t^2}\right\rangle, \tag{3.5}$$

where p_x and p_y are the scalar components of the transverse momentum $\vec{p}_t$, with the x-axis along the impact parameter vector (see Fig. 3.2). The brackets denote the average over the particles from all events in the (y,p_t) bin under study.

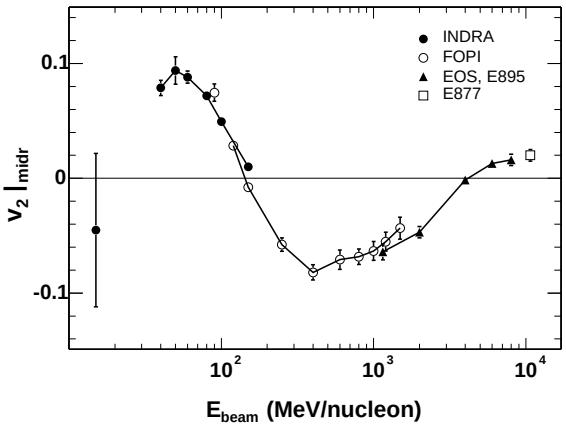

Figure 3.3: Elliptic flow parameter v_2 at mid-rapidity for collisions with intermediate impact parameters (about 5.5-7.5 fm) as a function of incident energy. The filled and open circles represent the INDRA and FOPI [44] data, respectively, for $Z = 1$ particles. The triangles represent the EOS and E895 [45] data for protons and the square represents the E877 data [46] for all charged particles. Reprinted from [47].

Figure 3.3 summarizes some of the experimental results on the elliptic flow as a function of the incident energy. Negative (positive) values of elliptic flow indicate preferential out-of-plane (in-plane) emissions. As can be seen, the squeeze-out effect attains a maximum for collisions at energies of about 400 MeV/nucleon. The observed changes of the emission pattern are related to a complex interplay between fireball expansion and spectator shadowing.

The first experimental information on the symmetry energy at high densities from flow measurements of neutrons and charged particles was obtained by the FOPI collaboration [48]. The results have been interpreted using the extended version of the UrQMD model [49] assuming different stiffnesses of the symmetry energy [50, 51]. The density dependence of the symmetry energy potential was parametrized using a power law formula: $(\rho/\rho_0)^\gamma$, where the exponent γ was assumed to be 0.5 and 1.5 for the soft and stiff versions. From the comparison to the experimental data the exponent γ has been estimated to be 0.9 ± 0.4. This value of γ corresponds to $L \simeq 83$ MeV, which indicates a stiffer symmetry energy as compared to the results for lower densities (see Fig. 2.5). The FOPI measurements provided also information on the π^- and π^+ production in the ^{197}Au + ^{197}Au collisions at various relativistic energies [52]. The obtained data have been interpreted by theoretical groups using different transport models, and the results turned out to be very model dependent. For instance, the ImIBL [53] and IBUU04 [31] models were able to describe the experimental data relatively well using the super soft symmetry energy, while the ImIQMD [43] model required the stiff symmetry energy to describe the same data. Moreover, the calculations of Hong and Danielewicz [54] indicate the lack of sensitivity of net pion ratios to the symmetry energy. Thus, further theoretical studies are needed before pion yield ratios can be reliably applied to investigations of the symmetry energy at high densities. The apparent discrepancies between various experimental results call for dedicated high energy experiments aiming at providing more precise constraints on the symmetry energy at high densities.

Chapter 4

ASY-EOS experiment

The ASY-EOS experiment has been designed to study the behavior of the symmetry energy at supra-saturation densities by measuring flows of neutrons and light charged particles in heavy ion collisions at near-relativistic energies [13, 14]. The symmetric collision systems ^{197}Au+^{197}Au, ^{96}Ru+^{96}Ru and ^{96}Zr+^{96}Zr at 400 MeV/nucleon incident energy have been chosen for the measurements. Neutron and proton flows for the ^{197}Au+^{197}Au ($N/Z = 1.49$) system at the same projectile energy were previously measured in the FOPI-LAND experiment, using the LAND neutron detector and the FOPI forward wall [55]. However, the analysis of the FOPI data has shown that additional measurements are necessary to improve the statistical accuracy of the experimental flow parameters. The ^{96}Ru+^{96}Ru ($N/Z = 1.18$) and ^{96}Zr+^{96}Zr ($N/Z = 1.40$) systems allow to compare neutron-rich and neutron-deficient systems of the same mass, enhancing the isospin effects.

The ASY-EOS measurements were performed at the SIS facility of GSI, Darmstadt, in May 2011 (S394 experiment). The experimental setup is shown schematically in Fig. 4.1.

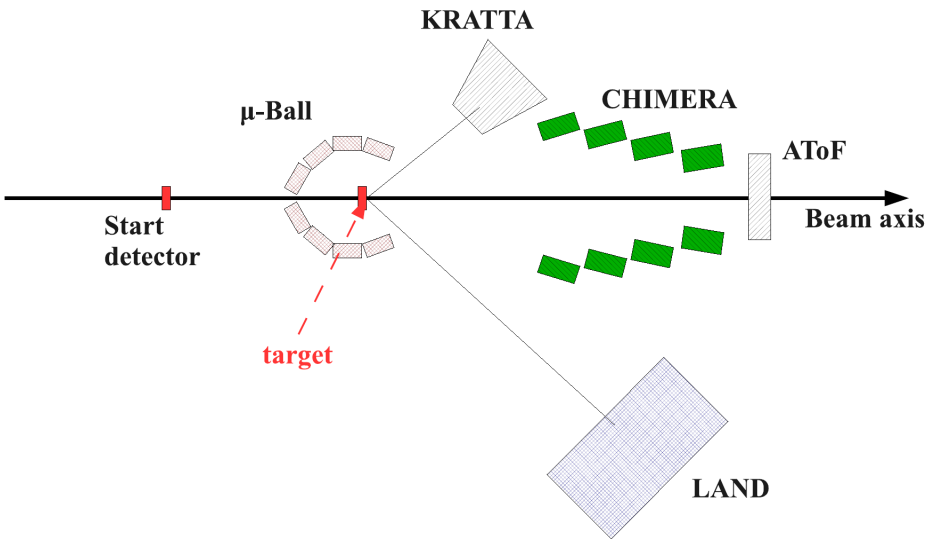

Figure 4.1: Schematic view of the ASY-EOS experimental setup (not to scale).

The beam directed to the target was passing through a thin plastic scintillator foil, which served as a start detector for the time-of-flight measurements. Neutrons and light charge particles were measured by the LAND detector [56], which was centered at a polar angle of $\theta_{LAB} \sim 45^\circ$ with respect to the beam axis to efficiently cover the mid-rapidity kinematic region. A veto-wall of plastic scintillators (VETO) was mounted in front of LAND in order to discriminate neutrons and charged particles. The KRATTA array [15], located on the opposite side of the beam with respect to LAND, was used to measure yields and flows of isotope-resolved charged particles. It covered approximately the same solid angle and range of polar angles as the LAND detector, performing the complementary measurements under the same experimental conditions. For event characterizations such as the impact parameter and the orientation of the reaction plane, three additional detector systems were installed. The CHIMERA detector [57] and the ALADIN Time-of-Flight Wall [58] were used to detect charged reaction products emitted in forward directions. The μ-Ball scintillator array [59], surrounding the target, was used to identify non-target events and to provide additional multiplicity and trigger information. Figure 4.2 shows the acceptance of the setup for protons in the representation of the transverse momentum per unit mass versus the rapidity.

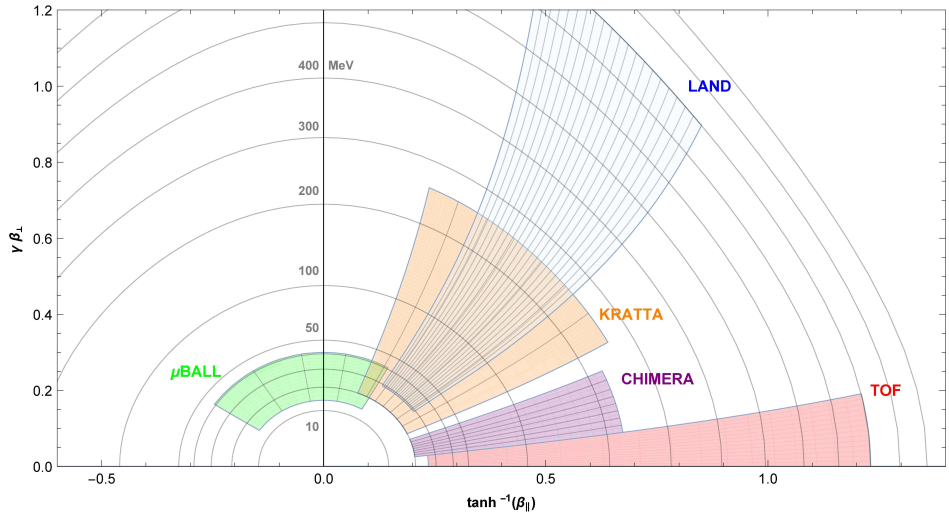

Figure 4.2: Acceptance of the detectors used in the ASY-EOS experiment for protons in the $\gamma\beta_\perp$ vs rapidity $\tanh^{-1}(\beta_\parallel)$ representation. The contours represent the constant proton energies specified at the inner vertical axis in MeV.

The Large Area Neutron Detector (LAND) was constructed and used in many experiments at the GSI laboratory to measure the momenta of neutrons from near-relativistic heavy-ion collisions [56]. The detector consists of 200 modules (paddles) of 2 m length and 10x10 cm^2 cross section. They are arranged in 10 consecutive layers, alternating between horizontal and vertical orientations, forming a block having a front area of 2x2 m^2 and a depth of 1 m. The modules have a multilayer structure of passive iron converters and active plastic scintillators. Each paddle is equipped with two photomultipliers attached to its ends. A neutron interacting with the detector material produces secondary charged particles that generate scintillation light pulses (hits) in one or more paddles. The scintillation light created in a paddle propagates to both paddle ends and is detected by photomultipliers, providing information on the

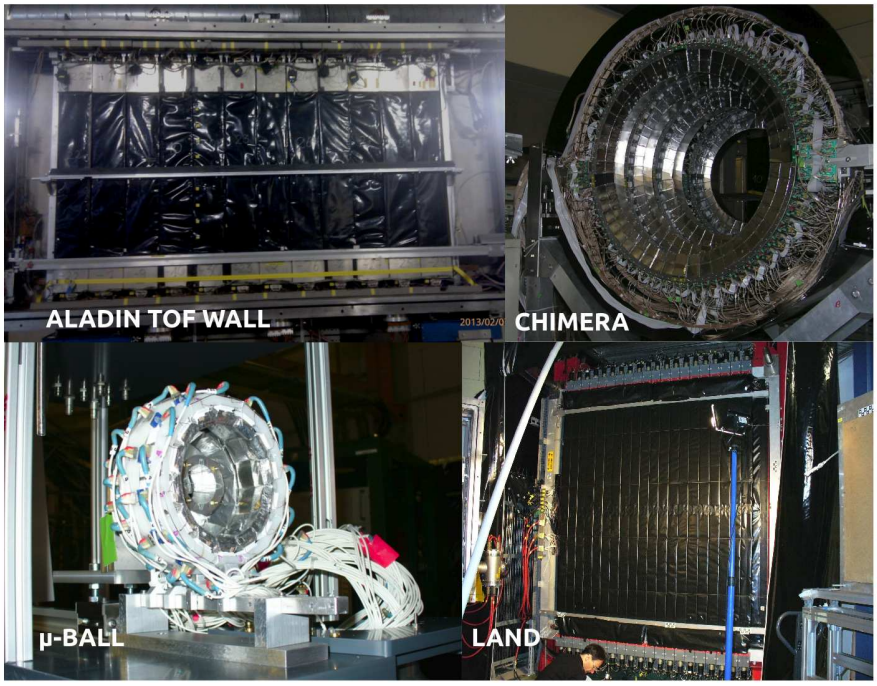

Figure 4.3: Detectors used in the ASY-EOS experiment: top left: ALADIN Time-of-Flight Wall, top right: four double rings of CHIMERA, bottom left: μ-Ball, bottom right: LAND.

time and spatial location of the hit. The internal time resolution is approximately 250 ps and the position resolution derived from the timing signals is about 3 cm. Additional calorimetric information of the energy deposit can be obtained from the measured signal amplitudes. Within an event, incoming neutrons and charged particles may produce several hits. Special algorithms analyzing the time-spatial hit distribution are used to determine the number of neutrons and their velocity vectors [60]. A veto scintillator array (VETO) installed in front of LAND allows to discriminate charged particles from neutrons. Charged particles are recognized on the basis of coincident hits in VETO, matching the corresponding tracks in LAND. The identification of the atomic number Z of light charged particles can be achieved from the measured energy loss in VETO and time-of-flight. During the S394 experiment the LAND detector was operated with new TACQUILA GSI-ASIC electronics and was placed at a distance of 5 m from the target, covering polar angles 37.7°- 56.5° with respect to the beam direction. The VETO wall consisted of 10 cm wide and 0.5 cm thick plastic scintillator paddles covering the front area of LAND. The paddles were vertically oriented, parallel to those in the first plane of LAND.

The KRATTA detector (KRAków Triple Telescope Array) was built to measure the energy, emission angle and isotopic composition of light charged reaction products within a broad energy range [15]. In the ASY-EOS experiment, 35 modules of KRATTA were arranged in a 7x5 array and located opposite to LAND at a distance of 40 cm from the target. They covered a solid angle of about 160 msr at polar angles between 24° and 68°. A detailed description of the KRATTA array will be presented in the next chapter.

CHIMERA (Charged Ion Mass and Energy Resolving Array) is a 4π multidetector for charged particles dedicated to studies of heavy ion collisions at intermediate energies (10-100 MeV/nucleon) [57]. CHIMERA was constructed and operates at the INFN - Laboratori Nazionali del Sud in Catania. Its main features are: high angular coverage and granularity, low detection threshold and high dynamical range as well as good particle identification capabilities. The CHIMERA detector consists of 1192 telescope modules arranged in 35 rings. The forward 18 rings cover the polar angles between 1° and 30° and are placed at a distance from the target decreasing from 350 to 100 cm with increasing angle. The remaining 17 rings, covering polar angles from 30° to 176°, form a sphere of a radius of 40 cm. The overall detection solid angle is about 94% of 4π. Each telescope module consists of a 300 μm thick silicon detector, providing also a fast timing signal for time-of-flight measurements, and a CsI(Tl) scintillation crystal whose thickness decreases from 12 to 3 cm with increasing polar angle. During the ASY-EOS experiment, only 8 forward-angle rings were used, covering polar angles between 7° and 20°.

A central square part of the ALADIN Time-of-Flight (ATOF) Wall [58] of an area of about 1 m^2 was placed in the beam direction at a distance of 3.7 m from the target. It consists of two layers (front and rear) of vertically oriented plastic scintillator paddles which are 110 cm long, 2.5 cm wide, and 1cm thick. The scintillation light was read out by photomultipliers mounted at both ends of the paddles. This Wall was used to detect forward emitted charged particles and fragments at polar angles smaller than 7°. The fast timing signals were also used to generate a reaction trigger.

The μ-Ball is a 4π multidetector for low energy light charged particles and fragment detection [59]. In total it consists of 95 CsI(Tl) scintillators arranged in 9 rings, which cover an polar angular range of 4°-172°. The scintillation light is collected by silicon photodiodes. Only 4 rings (50 CsI segments) were used during the ASY-EOS experiment, covering the polar angle range of 60°-147°. Due to a small diameter of the device, the detection solid angle was nearly negligible for reactions occurring in the air downstream from the target, allowing for their suppression.

Typical beam intensities of about 10^5 pps and targets of 1-2% interaction probability allowed to collect about $5{\cdot}10^6$ events for each system during about two weeks of measurements. The experiment has been conducted in air which caused a significant background mainly due to reactions in air and in other non-target materials. In order to evaluate this background, additional runs without the target have been performed. High statistics background runs were also taken with an iron shadow bar placed in front of the LAND detector to shield it from the neutrons coming directly from the target.

Chapter 5

KRATTA detection system

5.1 Detector construction

KRATTA (KRAków Triple Telescope Array) [15] is a versatile low threshold broad energy range detection system for the light charged reaction products. It was designed and built for the needs of the ASY-EOS experiment, however it also suits well the needs of the cyclotron facility at IFJ-PAN in Kraków. KRATTA has modular construction, it consists of 38 independent, identical modules. Such a design allows to arrange the detector into various configurations. Figure 5.1 presents the configuration used during the ASY-EOS experiment.

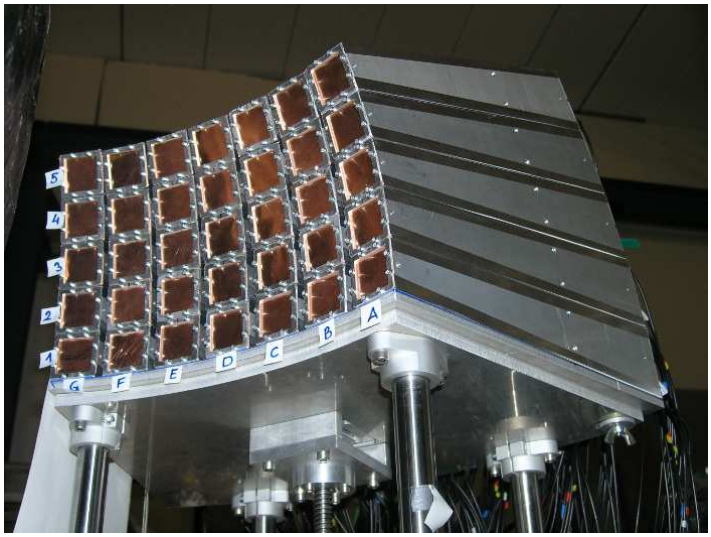

Figure 5.1: The KRATTA detector during the ASY-EOS experiment (May 2011).

Each module contains three large area PIN silicon photodiodes and two cesium iodide crystals enriched with thallium, CsI(Tl). The arrangement of these active elements in the module is presented in Figs. 5.2 and 5.3. The first photodiode (PD0) works as a ΔE silicon detector providing the ionization signal alone. The second photodiode (PD1) works in a *Single Chip Telescope* [61] (SCT) configuration and provides a combined signal of the direct (silicon ionization) component and of the scintillation components from the first, 2.5 cm long crystal (CsI1). This novel detection technique will be described in details in Section 5.3. The third

photodiode (PD2) detects the light produced in the thick, 12.5 cm long crystal (CsI2) and, in addition, provides an ionization signal for particles punching through the crystal and hitting the photodiode. The photodiodes of the thickness of 500 μm and the active area of 28 mm x 28 mm were produced by HAMAMATSU. The CsI crystals were polished and wrapped with a highly reflective foil (Enhanced Specular Reflector). The crystals were optically decoupled and the windows for photodiodes were protected with 6 μm thick Mylar foils. The active elements were placed inside aluminum boxes together with charge preamplifiers (see Fig. 5.2). The entrance window was made of a 100 μm thick copper foil.

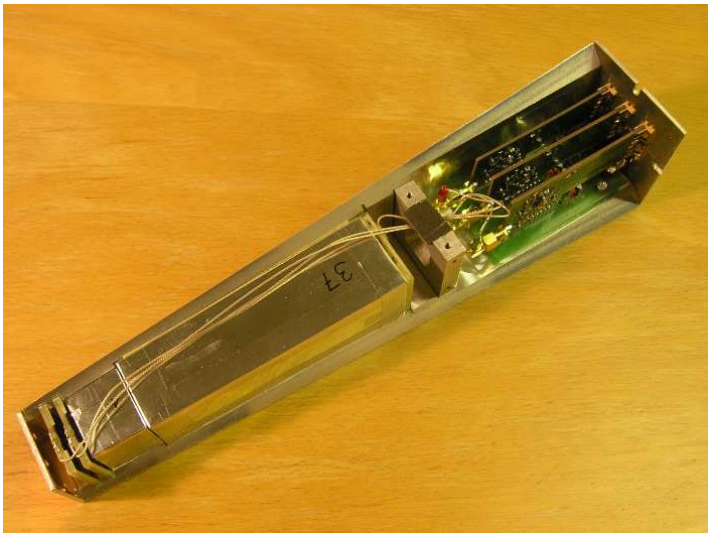

Figure 5.2: Single KRATTA module content: two CsI crystals wrapped in a foil and three Si photodiodes connected to preamplifiers.

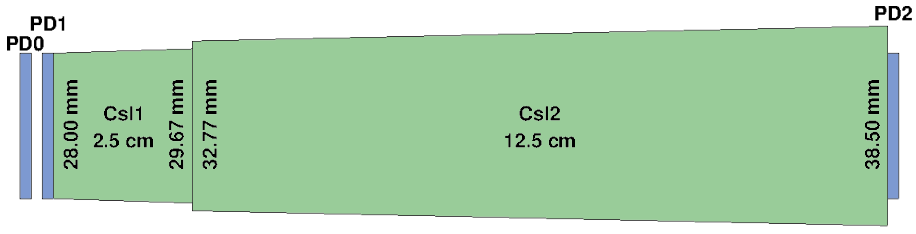

Figure 5.3: Layout of the KRATTA module's active elements. Two CsI crystals (CsI1, CsI2) and three Si photodiodes: from the left: PD0, PD1, PD2, respectively.

Due to the presence of the photodiode frames and the aluminum housing the geometric acceptance of a single module was reduced to about 54% of the subtended solid angle. The KRATTA was designed to operate at the distance of 40.2 cm from the target. The active solid angle of the single module amounts to 4.5 msr. The detection energy ranges for various particle species are given in Table 5.1.

Table 5.1: Lower, E_{low}, and intermediate, E_{int}, thresholds and upper limits, E_{up}, for selected species (in MeV/nucleon). The thresholds and upper limits correspond to the energy losses in 500 μm of Si, in 1000 μm of Si + 2.5 cm of CsI and in 1000 μm of Si + 15 cm of CsI, respectively.

Fragment	E_{low}	E_{int}	E_{up}
^{1}H	8.3	89.6	254.4
^{4}He	8.3	89.4	253.9
^{7}Li	9.5	103.6	296.5
^{20}Ne	19.9	231.3	719.0
^{43}Ca	26.7	339.7	1134.2
^{91}Zr	34.0	513.9	1911.8
^{197}Au	38.6	775.8	3550.9

5.2 Electronics and data acquisition

The photodiodes have been reverse biased at 120 V by using the custom made 120-channel remote controlled, high voltage power supplies. The signal converted in the preamplifier to the voltage-pulse was digitized with the 100 MHz, 14-bit Flash Analog-to-Digital Converters [62] (FADC). The digitized signal was stored for the further off-line analysis using the GSI acquisition system MBS [63] (Multi Branch System). This system controlled the whole data acquisition during the ASY-EOS experiment. The diagram of the signal flow is presented in Fig. 5.4.

The waveforms were registered in 5.12 or 10.24 μs time windows (512 or 1024 time bins). The first 2 μs pre-trigger part of the waveform was preserved for a precise baseline estimation. The shorter time window with the length of 5.12 μs was used for the first photodiode (PD0) signals. It was sufficient for recording the fast ionization signal. For 1 kHz single hit rate, the data throughput is expected to amount to about 5 MB/s. During the ASY-EOS experiment, the data flow was about 0.14 MB/s. The detectors were "slow controlled" with the Go4 system [64] using the implemented procedures, which allowed monitoring some observables defined for the registered events, such as the hit rate per photodiode, the base-line stability over time, as well as the ΔE-E identification maps. This monitoring system allowed to react in case of unexpected detection system behavior.

5.3 Single Chip Telescope technique

In a Single Chip Telescope [61] a single large area photodiode is placed in front of the scintillator, preferably a slow one e.g. CsI(Tl). Such a single photodiode plays a double role, serving as a passing-through silicon ΔE detector and a light sensor. Thus, two signals from the standard ΔE-E telescope technique are replaced by a single one at the expense of complication of its shape. In the case of CsI(Tl) scintillator, the produced pulse is the sum of three components: the fast direct silicon ionization component and the fast and slow scintillation components.

The principle of operation of the SCT in KRATTA is depicted in Fig. 5.5. An incident

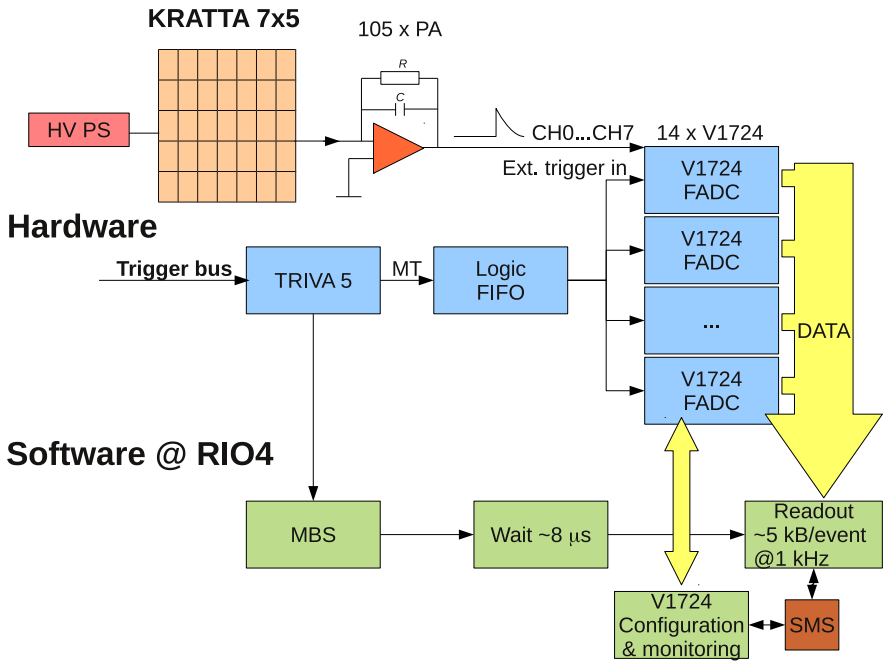

Figure 5.4: The signal flow chart for KRATTA data acquisition during the ASY-EOS experiment. HV PS is the high voltage power supply, PA - charge sensitive preamplifier, V1724 - CAEN digitizers, TRIVA5 - VME Trigger Synchronization Module, MT - master trigger, FIFO - logical Fan-In Fan-Out module, RIO4 - VME controller board, MBS - Multi Branch System, a GSI acquisition standard, SMS - Shared Memory Segment. Reprinted from [15].

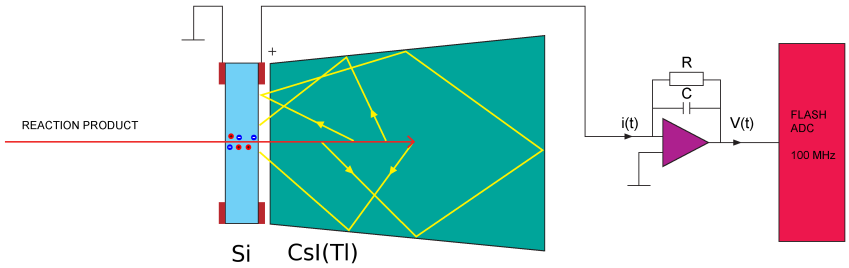

Figure 5.5: A Single Chip Telescope in KRATTA. Si - silicon photodiode, CsI(Tl) - scintillation crystal, $i(t)$ - current pulse, $V(t)$ - voltage pulse, RC - time constant of the preamplifier feedback loop.

charged particle punches-through the silicon photodiode and stops in the CsI crystal. The signal produced in the silicon photodiode is created in the ionization process. The electron-hole pairs are produced as a result of charged particle transition. The carriers drift in the external electric field and induce current in the electrodes. The induced current as a function of time is schematically presented in Fig. 5.6. It was obtained using a simple model based on the Bragg peak parametrization and using the Ramo theorem (for details see [65]). When the incident particle enters the crystal, it generates a scintillation light. The light propagates in the crystal and finally falls on the photodiode surface and generates the electron-hole pairs. Both the ionization and the scintillation signals sum up. The current signal from the photodiode is integrated in a charge sensitive preamplifier and finally digitized with a Flash ADC. Due to the difference in time characteristics of the ionization and scintillation processes, such a composite signal can be deconvoluted by off-line pulse shape analysis.

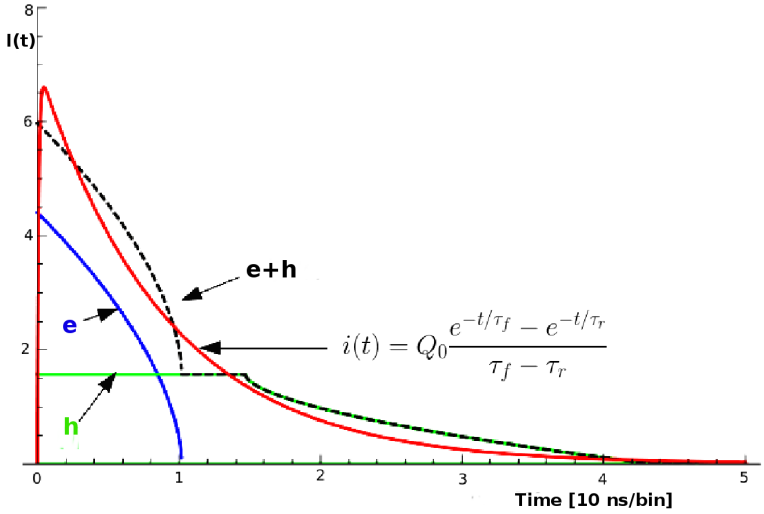

Figure 5.6: The current induced in the photodiode electrodes by a charged particle consists of the electron (e) and the hole (h) components. The red line shows an approximate parametrization of the total current with the indicated functional form of $i(t)$.

The main advantage of the SCT method is reducing the number of read-out channels from two to one. Moreover, the photodiode is an active part of the telescope, and thus the detection threshold is lowered. On the other hand, it requires the application of an effective pulse shape analysis procedure to extract the ionization and scintillation components from the measured waveform.

Chapter 6

KRATTA data reduction and processing

The processing of the KRATTA data has been performed in several steps, starting from the lower, hardware level, up to having the desired physical event representations which open a wide area for physical investigations and analysis. The first stage of the data processing, which is described in this chapter, includes:

- raw data decoding and preprocessing
- pulse shape parametrization and decomposition
- particle identification
- energy calibration.

Further steps of the KRATTA data analysis such as the background reduction, corrections for detection efficiency and rejection of non-target events will be presented in the next chapters.

6.1 Raw data characteristics

During the ^{197}Au+^{197}Au measurements nearly half of the volume of the collected data was produced by the KRATTA detector. It was caused by the fact that in the case of KRATTA the whole waveforms were stored. They were needed for the off-line pulse shape analysis. The data were stored in a format that was specific for the digitizer [62], and an algorithm for decoding the KRATTA raw events was implemented.

Figure 6.1 presents an example of signals detected by the three photodiodes for the case of an alpha particle stopped in the thick crystal (CsI2). Various baseline and amplitude levels can be noticed. The relatively small PD0 signal allows to see noise fluctuations.

The KRATTA module operates as a three-fold ΔE-ΔE-E telescope. It allows plotting identification maps with the use of signal amplitudes from the first two photodiodes: PD0 vs PD1 or from the second pair i.e. PD1 vs PD2, which are presented in Figs. 6.2 and 6.3, respectively. They reveal isotopic lines, and starting from the left bottom corner they correspond to p, d, t, ^{3}He, α, ^{6}He, ^{6}Li, ^{7}Li and so on. The map in Fig. 6.2 shows a complex spectrum with each isotopic line composed of an ordinary Si-Si hyperbolic part at low energies for particles stopped in PD1, and a more curved part for particles punching through the PD1 photodiode and stopped in the CsI1 crystal. Due to the complex structure and line crossing, this kind

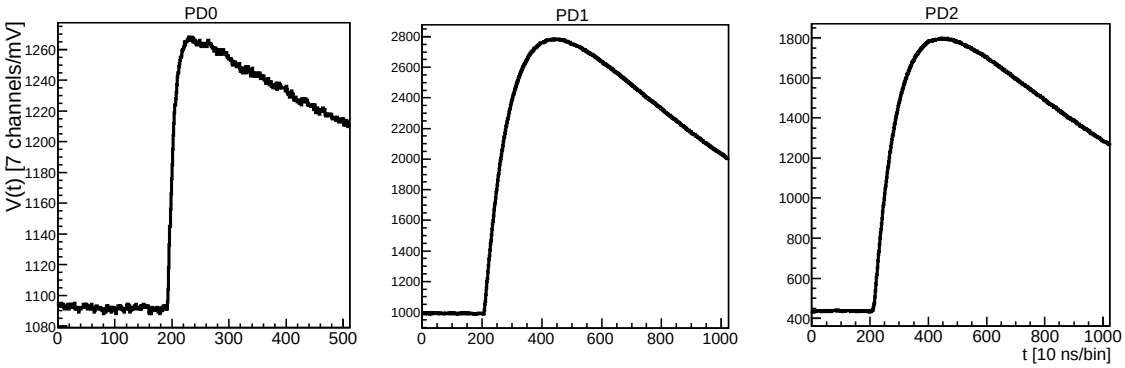

Figure 6.1: Pulses measured with PD0, PD1 and PD2 photodiodes, which were generated by an α particle of kinetic energy of about 500 MeV. Full time scale corresponds to 5 (PD0) or 10 (PD1, PD2) μs.

of a map is not well suited for identification, however, the presence of many characteristic punch-through points and curvatures makes it particularly useful for the energy calibration purpose. In the map 6.3, apart from the very well separated isotopic lines, one can also see a substantial background and back-bendings corresponding to particles punching through the thick crystal.

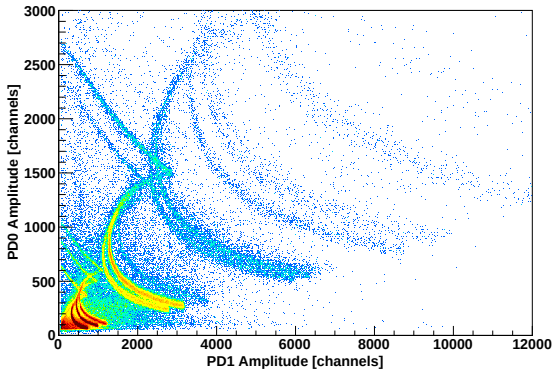

Figure 6.2: ΔE-E identification map for the first two photodiodes, PD0 vs PD1 (SCT) with veto on PD2 signals.

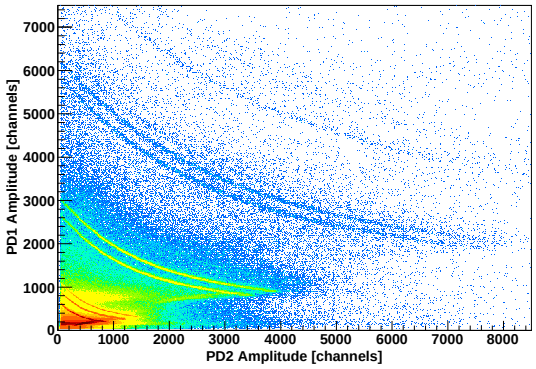

Figure 6.3: ΔE-E identification map of signals from PD1 and PD2.

6.2 Digital pulse shape analysis

In order to simplify and speed up the analysis, it was necessary to reduce the amount of data associated with the KRATTA detector. Operating with the raw pulse shapes would have been ineffective and resource-expensive. Three kinds of the pulse shape representations were introduced: the pulse shape samples, the waveform moments and the parameters obtained from a pulse shape fitting and decomposition procedure. However, firstly, for each of the pulses the following basic characteristics were extracted: the baseline voltage (offset), the signal starting time, t_0, and the value and time of the maximum of the waveform.

6.2.1 Preanalysis

The baseline offset was determined as the average of the voltage values within a time interval preceding the signal. The starting time of the pulse, t_0, was extracted from the crossing point of the baseline and of the straight line fitted to the early part of the rising slope. The amplitude maximum and its position were estimated with a local parabolic fitting procedure in order to smooth noise fluctuations.

6.2.2 Signal sampling

The most straightforward way of reducing the amount of the data is a pulse shape sampling with smoothing. In our approach the waveform was probed at ten intervals along the rising slope with a constant voltage step of 10% of the amplitude, and at ten equal time intervals within the falling slope, between the maximum and the end of the waveform (see Fig. 6.4). The impact of local signal fluctuations was reduced with a smoothing procedure applied before taking a sample. This procedure was based on a local second-order polynomial fitting in the vicinity of the sampling point. As a result, the waveform is characterized by a set of 21 parameters: ten time values (from the rising slope and for the position of a maximum) and eleven voltage values (the amplitude and the samples within the falling slope), measured with respect to the beginning of the pulse.

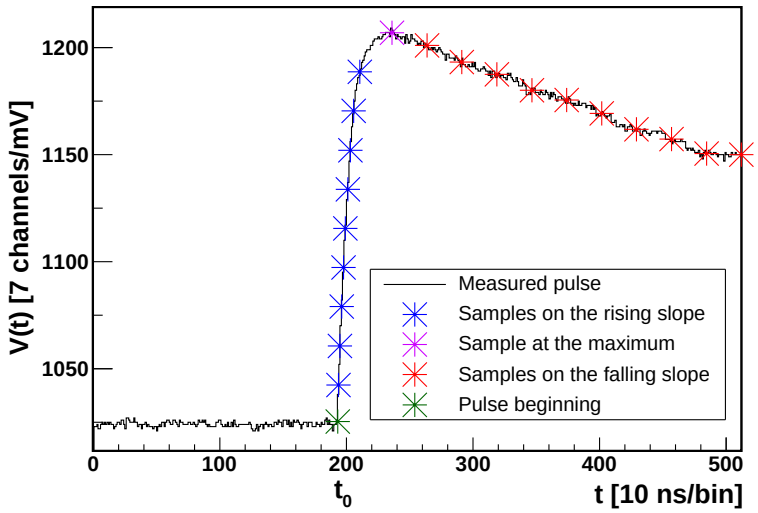

Figure 6.4: Illustration of the waveform sampling.

6.2.3 Waveform moments

Another set of quantities characterizing the pulse shape consists of the waveform moments. We have used the ten lowest order moments calculated according to the following definitions:

$$\begin{aligned} M_0 &= \sum_i V(t_i), \\ M_k &= \frac{1}{M_0} \sum_i \left(\frac{t_i - t_0}{t_{max}} \right)^k V(t_i), \qquad k \in \{1, .., 9\}, \end{aligned} \tag{6.1}$$

where $V(t_i)$ is the baseline-subtracted signal value at the time instant t_i. As stated before, t_0 is the pulse beginning time, and t_{max} is the signal end time. The zero-th moment, when multiplied by the time bin width, is the pulse integral. This moment was used as a normalization factor for the moments of higher order.

6.2.4 Pulse shape parametrization and decomposition

The most refined method used for describing pulse shapes is the parametric fitting and decomposition procedure. This procedure assumes an analytical form of the current pulse shapes of the ionization and scintillation components generated by a photodiode. Then, the preamplifier voltage response to the entire current signal is calculated and fitted to the measured waveform. The best fit provides a set of parameters characterizing the individual components.

For each component, the current signal, $i(t)$, was parametrized using the following function:

$$i(t) = Q\frac{e^{-t/\tau_1} - e^{-t/\tau_2}}{\tau_1 - \tau_2}, \tag{6.2}$$

where Q is the integral of the pulse i.e. the total induced charge, τ_1 and τ_2 are the time constants representing the signal rise and fall times. The preamplifier response, $V(t)$, was calculated using a simple parallel RC circuit approximation [66]:

$$\frac{dV(t)}{dt} + \frac{1}{RC}V(t) = \frac{i(t)}{C}, \tag{6.3}$$

where RC is the feedback coupling time constant. This approximation assumes an ideal operational amplifier with infinite open-loop gain, a negligible small detector capacitance and a zero rise time of the charge integrator. Such an idealization enables an analytical approach. Solving the above differential equation for the assumed $i(t)$ in the form 6.2 one obtains the following voltage output for each individual component:

$$V_i(t) = Q_i RC\left(\frac{e^{-\Delta t/RC}RC}{(RC-\tau_{1,i})(RC-\tau_{2,i})} + \frac{e^{-\Delta t/\tau_{1,i}}\tau_{1,i}}{(\tau_{1,i}-RC)(\tau_{1,i}-\tau_{2,i})} + \frac{e^{-\Delta t/\tau_{2,i}}\tau_{2,i}}{(\tau_{2,i}-RC)(\tau_{2,i}-\tau_{1,i})}\right). \tag{6.4}$$

The index i refers to a particular component. Let $i = 1$ be for the ionization component, while $i = 2$ and $i = 3$ for the fast and slow scintillation components, respectively. The three component function

$$V(t) = V_1(t) + V_2(t) + V_3(t) \tag{6.5}$$

was fitted to the baseline-subtracted waveforms from PD1 and PD2. For the PD0 signals only one component (ionization) was used. Overall, the model contains 11 parameters that are listed in Table 6.1.

In the fitting procedure, constraining some of the parameters was found inevitable to avoid the local minima problem and obtain a global agreement between the reconstructed amplitudes and the predictions based on the ATIMA range-energy tables [67]. The RC time constant was determined individually for each preamplifier by examining pulses with the fast ionization component alone. The resulting RC constants were somewhat smaller than the nominal ones due to small leakage currents. Some of the rise and fall time parameters were fixed to the values found from the overall fit, as it is shown in Table 6.1. In the case of PD0, the two parameters $\tau_{1,1}$ and $\tau_{2,1}$ were fitted in order to precisely describe the shapes for particles stopped in this photodiode.

Table 6.1: Parameters of the model waveforms.

Parameter		Value	
Ionization			
Q_1	Amplitude		fitted
$\tau_{1,1}$	Rise time	∼90 ns	fixed/fitted
$\tau_{2,1}$	Fall time	<300 ns	fixed/fitted
Scintillation			
Q_2	Fast component amplitude		fitted
Q_3	Slow component amplitude		fitted
$\tau_{1,2}$	Fast rise time	∼140 ns	fixed
$\tau_{1,3}$	Slow rise time	∼140 ns	fixed
$\tau_{2,2}$	Fast fall time	∼650 ns	fitted
$\tau_{2,3}$	Slow fall time	∼3.2 μs	fixed
Common			
RC	Preamp. fall time constant	∼6 μs	fixed
t_0	Time offset	∼2 μs	fitted
V_0	Baseline		fitted

The fitting method provides the actual charges Q for each component, irrespectively of the substantial ballistic deficit (reduction of the amplitude) due to a relatively short discharge time of the preamplifiers ($RC \simeq 6$ μs) which was chosen as a compromise between the probability of pile-ups, the baseline variation, and the ballistic deficit. Due to this advantage, for example, the sum $Q_2 + Q_3$ is a proportional measure of the total light produced in the scintillators.

Exemplary results of the fitting procedure are shown in Figs. 6.5, 6.6 and 6.7. The signals from PD0 contain only the ionization component. For particles penetrating into the CsI1 crystal, the PD1 (SCT) signals have all the three components (Fig. 6.6). In the case when particles are stopped in PD1 (not shown), the signals do not contain, obviously, any scintillation components. However, the fitting may produce for such particles a small artificial scintillation contribution of about 3.8±0.6% of the total amplitude. Similarly, the waveforms fitted to the PD2 signals for particles which do not hit the photodiode show a small artificial ionization component (see Fig. 6.7). It amounts, on average, to 1.7±0.5% of the total amplitude. These quoted numbers specify the quality of the parametrization and the systematic uncertainty of the decomposition into different components.

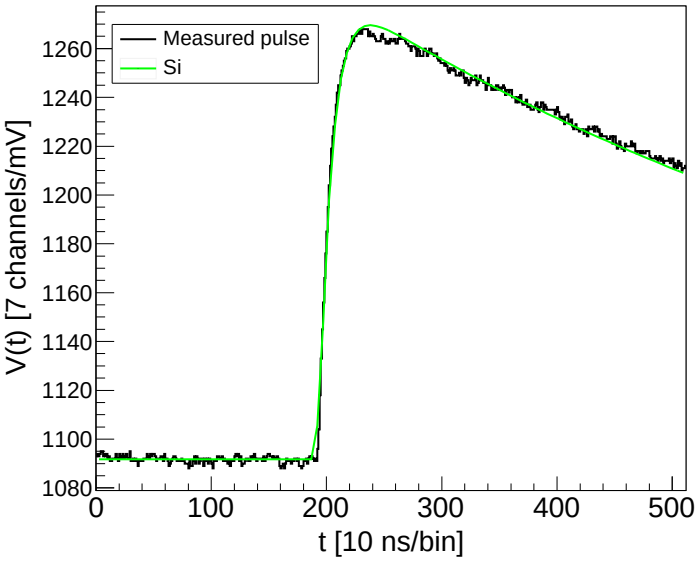

Figure 6.5: A waveform from the PD0 photodiode with the fitted ionization component.

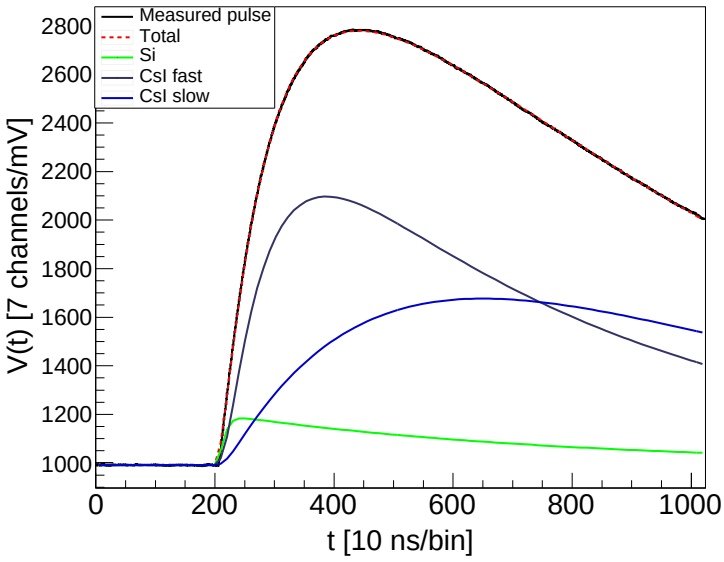

Figure 6.6: A waveform from PD1 and its decomposition.

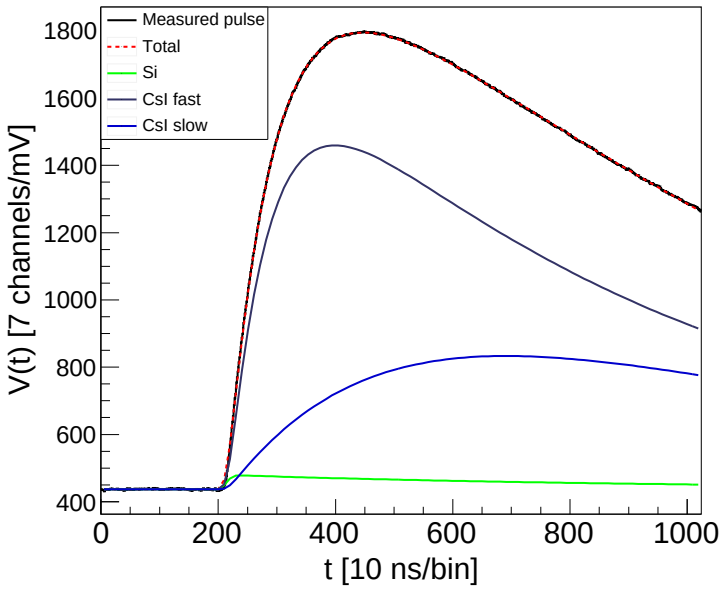

Figure 6.7: A waveform from PD2 and its decomposition.

6.3 Isotope identification maps

The obtained parameters of the reconstructed waveform components allow constructing various types of more refined identification maps. The most useful for the purpose of isotope identification are the ΔE-E maps. Examples of such maps are displayed in Figs. 6.8, 6.9, 6.10, and 6.11.

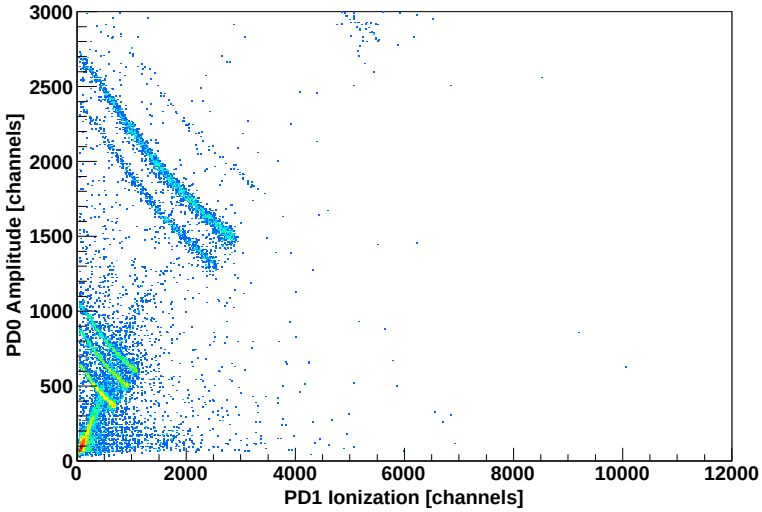

Figure 6.8: PD0 vs ionization signal from PD1 for particles stopped in PD1 (producing no light).

The map shown in Fig. 6.8 is the low energy part of the map of Fig. 6.2 i.e. for particles stopped in PD1. This extraction was possible by imposing the condition that the scintillation

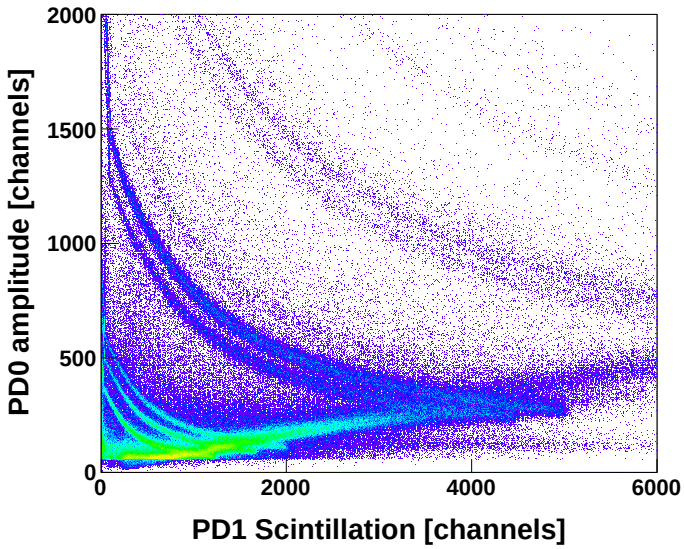

Figure 6.9: PD0 vs scintillation total light detected by PD1.

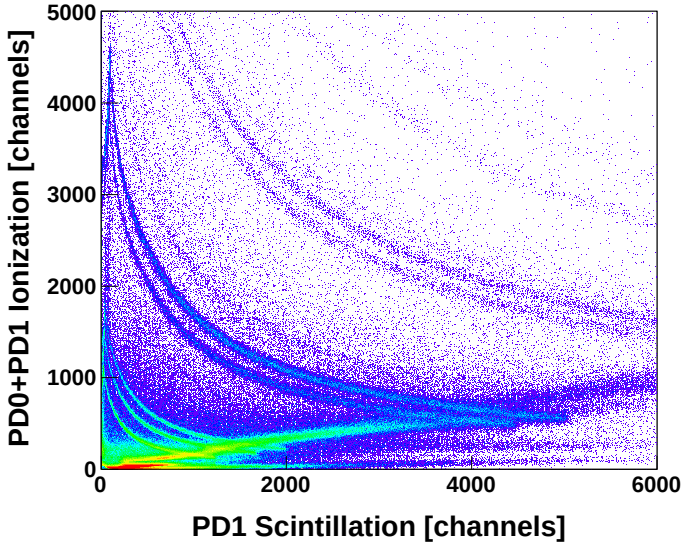

Figure 6.10: Summed PD0+PD1 ionization components vs scintillation total light in PD1.

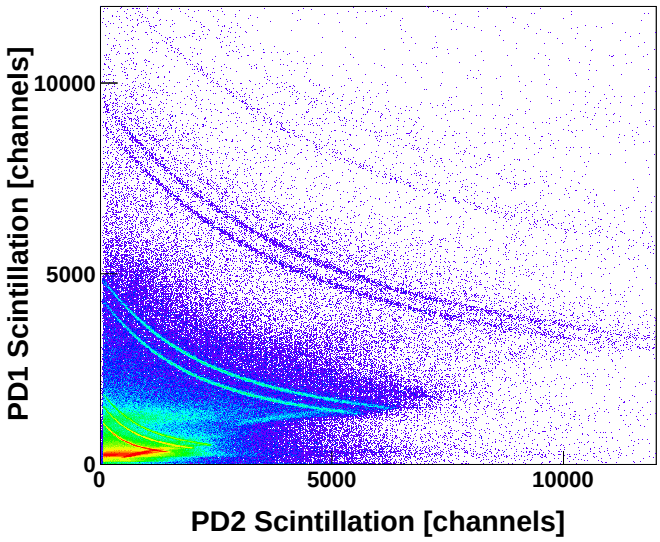

Figure 6.11: Map of scintillation signals for CsI1 vs CsI2 detected by PD1 and PD2.

component in PD1 is not present or negligibly small. The particles punching through PD1 and stopped in the CsI1 crystal can be identified with the map shown in Fig. 6.9. This map contains the punch-trough lines but they can be easily removed by the veto condition on PD2. Quite a similar map was obtained for the PD1 ionization versus scintillation components with about the same isotope resolution (not shown). This resolution can be improved by summing up the ionization components from PD0 and PD1, and thus, doubling the effective thickness of the first ΔE layer to 1 mm of Si, which is shown in Fig. 6.10. Particles which punch through the thin crystal and enter the thick one were identified with maps in which the total scintillation light from CsI1 is plotted against the total scintillation light from CsI2, as shown in Fig. 6.11. The visible back-bendings corresponding to particles punching through the thick crystal can be reduced, since the particles hitting the photodiode at the back of the thick crystal generate an ionization component in PD2.

The ΔE-E identification maps provide very good isotopic resolution, however, they contain a substantial background, particularly in the case of the thick scintillator (Fig. 6.11). The relative level of background can be better seen in Figs. 6.12 and 6.13 obtained by projection of the ΔE-E distributions (Figs. 6.10 and 6.11) along the isotope identification lines. The background originates mainly from the secondary reactions/scatterings in the crystals. The background contribution to the p, d, t peaks in Fig. 6.12 is about 6%. For energetic $Z = 1$ particles traversing the thick crystal (12.5 cm of CsI) the secondary reaction probability amounts to about 46% (Fig. 6.13). These probabilities agree reasonably well with the estimates obtained from the Geant simulations presented in Chapter 8. Some contribution to the background, particularly in the low energy region of the ΔE-E maps, arises also from accidental coincidences with the signals generated by γ-rays or neutrons, as well as from particles crossing the module at an angle and not originating from the target. In addition, the multi-hit events appear in those maps as background hits.

The amplitudes of the fast and slow scintillation components can be used for plotting additional identification maps. Examples are given in Figs. 6.14 and 6.15. Such Fast-Slow

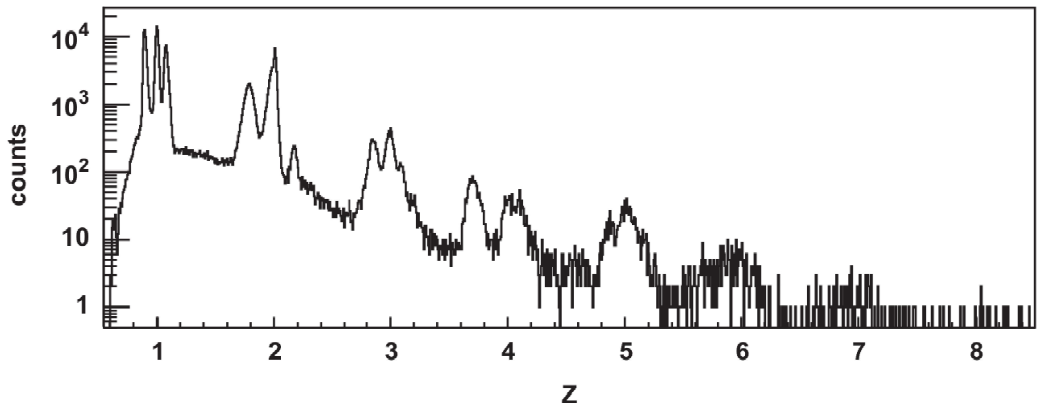

Figure 6.12: Particle identification spectrum (charge distribution) obtained from the map of Fig. 6.10, for particles stopped in the thin crystal.

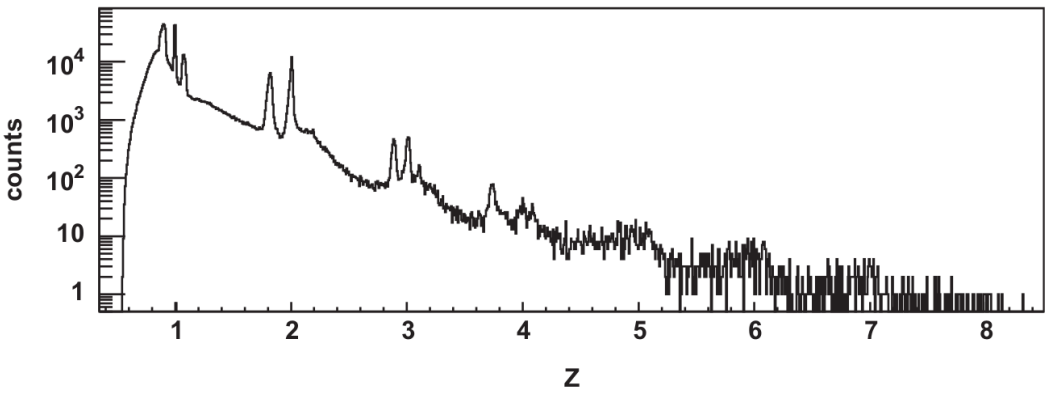

Figure 6.13: Same as Fig. 6.12, but obtained from the map of Fig. 6.11, for particles stopped in the thick crystal.

representations are often used for particle identification in the case when a scintillator (with a light sensor) is used alone. Figure 6.14 presents the standard Fast-Slow map for CsI1, in which the strong lowest-lying line is produced by γ-rays. This line can be precisely isolated and used for identification of the coincident background hits in the ΔE-E map. Figure 6.15 displays the sum of the scintillation components (the total light) versus the Slow to Fast ratio. In this representation, the punch through lines/segments do not cross the lower lying isotope lines in a way they do in the case of ΔE-E maps. Thus, such maps allow to isolate the punch through segments in a much more precise way. The map of Fig. 6.15 also shows a clear double-alpha line located above the ^{6}He line, which is hidden in the ΔE-E representation behind the Li isotope lines.

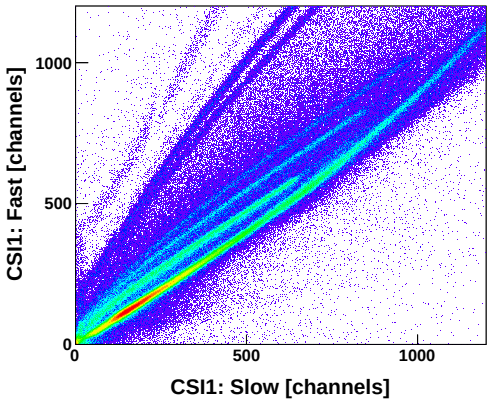

Figure 6.14: Fast versus Slow components of the scintillation in CsI1.

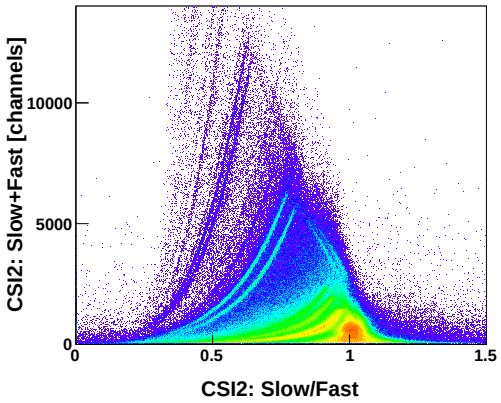

Figure 6.15: Total light versus Slow over Fast components of the scintillation in CsI2.

Another useful feature of the pulse shape analysis is demonstrated in Fig. 6.16. It allowed performing an identification of the majority of light particles stopped in the first photodiode by plotting the amplitude versus its position (mode) of the reconstructed current signal. The parametric fitting to the PD0 signal permitted to derive both, the rise and fall time parameters, and then calculate the mode value according to

$$mode = \frac{\tau_{1,1}\,\tau_{2,1}}{\tau_{1,1} - \tau_{2,1}} \log \frac{\tau_{1,1}}{\tau_{2,1}}. \tag{6.6}$$

This method permitted to reduce the identification thresholds, e.g. from 8.3 to about 2.5 MeV for protons, where they are still resolvable from deuterons (see the two bottom lines in Fig. 6.16).

6.4 Energy calibration

In order to perform the calibration of the energy loss in the silicon photodiodes one has to identify channels corresponding to the punch-through events. Knowing the thickness of the photodiodes and thus the punch-through energy as well as assuming a linear response of the silicon, one can assign the punch-through energy to the punch-through channels. The idea of the energy calibration of the energy loss in CsI crystals is presented in Figs. 6.17

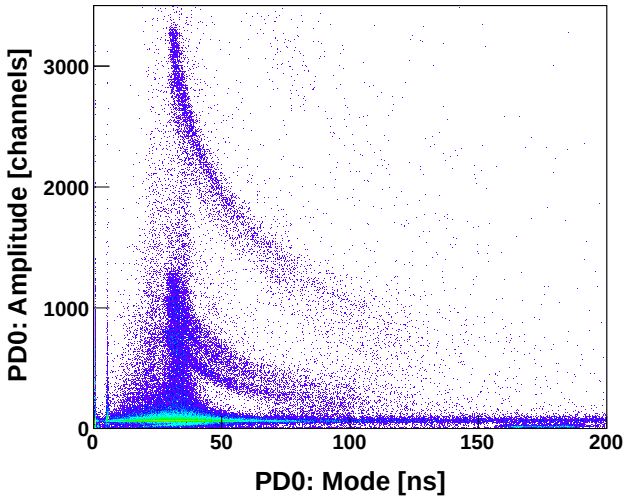

Figure 6.16: The maximum amplitude versus its occurrence time (mode) for particles stopped in PD0.

and 6.18. Figure 6.17 presents the amplitudes of raw signals from PD0 vs PD1 while Fig. 6.18 shows the scintillation components in thin vs thick crystals. The lines in these figures have been calculated using the ATIMA range-energy tables [67] and the light-energy conversion formula:

$$\text{Light} = a_1 \left(E - a_2 A Z^2 \log \left[1 + \frac{E}{a_2 A Z^2} \right] \right) \tag{6.7}$$

which has been obtained by integrating the Birks' formula [66] and assuming the specific energy loss $dE/dx \propto AZ^2/E$. In this formula, E denotes the particle energy loss in the crystal, A, Z its mass and atomic number and a_1, a_2 are the gain and quenching parameters. Two sets of the calibration parameters (one set for thin and one for thick crystal) have been determined by simultaneous fits of the ATIMA lines to the isotope identification lines in both experimental maps. The map in the Fig. 6.17 is especially useful because of its richness in characteristic punch-through points and curvatures. It was also used to verify the calibration of the energy loss in the silicon photodiodes.

In addition, the developed calibration procedure allowed to adjust the thicknesses of the dead and active layers. With the calibrated energy loss in each active element of KRATTA, one can calculate the energy of a given particle in the middle of the target, knowing the thicknesses of all the materials between the active element and the target. An example of the calibrated energy spectrum for the alpha particles is shown in Fig. 6.19. The arrows indicate the punch-through energies corresponding to consecutive layers of materials penetrated by an alpha particle i.e. the Au target, the air, the entrance Cu window and the active and passive elements of the detector such as the first and the second silicon photodiodes (PD0 and PD1) and their dead layers, the thin and thick scintillators (CsI1 and CsI2) and the wrapping foil. As can be seen, the effective energy threshold for alpha particles amounts to about 75 MeV and the upper energy limit is about 1 GeV.

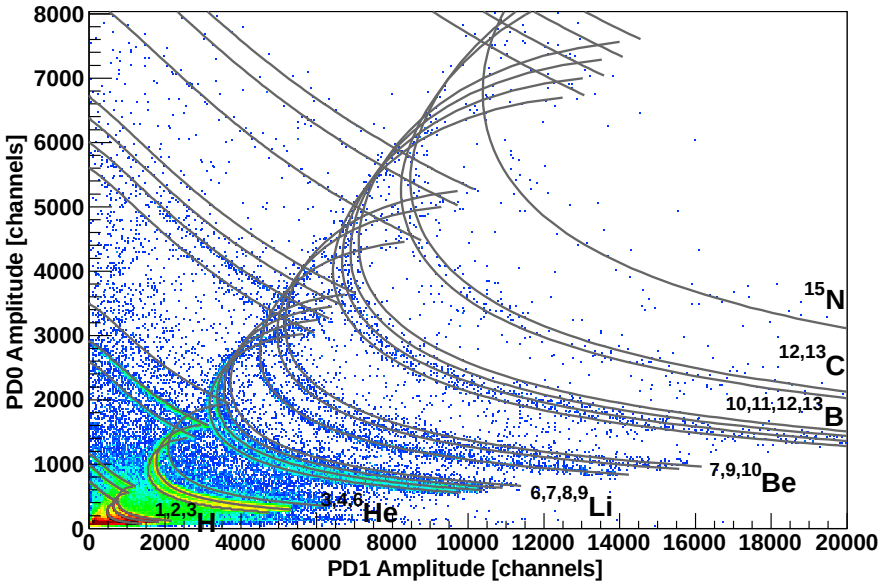

Figure 6.17: ΔE-E identification map for the amplitudes of raw signals from PD0 and PD1 with the superimposed lines calculated using the ATIMA tables.

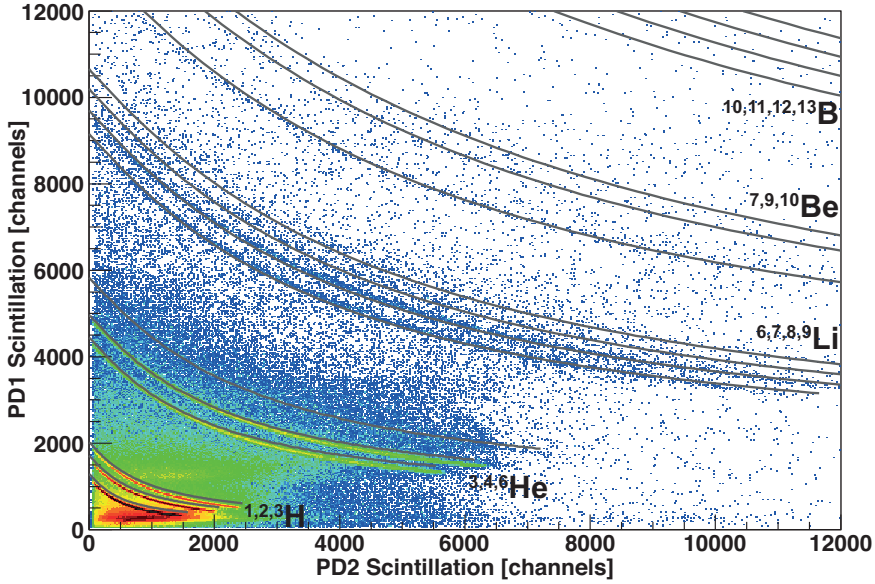

Figure 6.18: ΔE-E identification map for the scintillation signals from CsI1 and CsI2 with the superimposed isotope lines calculated using the ATIMA tables.

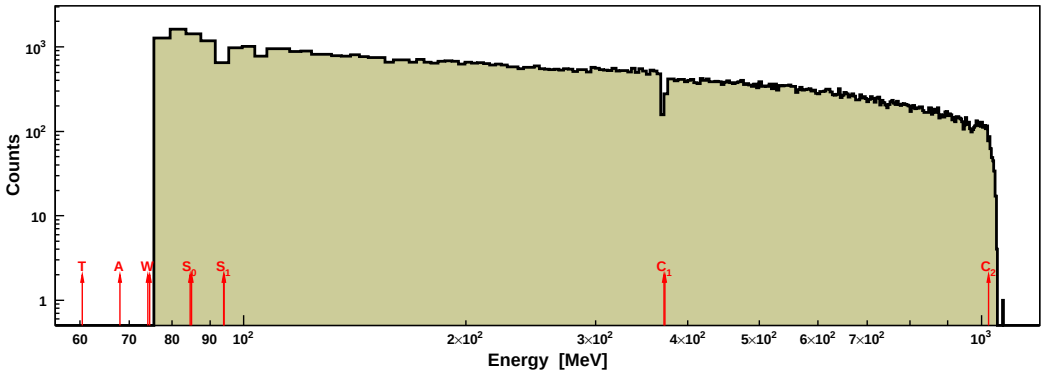

Figure 6.19: Energy spectrum of alpha particles. The arrows indicate the punch-through energies for a given absorber: T - target, A - air, W - window, S_0 - first silicon diode (PD0), S_1 - second silicon diode (PD1), C_1 - thin scintillator (CsI1), C_2 - thick scintillator (CsI2). Note the logarithmic scales on both axes.

Chapter 7

Background recognition with neural networks

7.1 Introduction

7.1.1 Artificial neural networks

Artificial neural networks (ANN) are adaptive statistical models for information processing inspired by the structure and operation of biological nervous systems. They consist of a set of processing units (neurons) with modifiable weighted connections between them. ANN learn their input-output mapping from relationships intrinsically present in training data sets. Neural networks show remarkable ability to derive meaningful information from complicated or imprecise data. They were used to solve many complex problems in science, engineering, medicine, business and finance. The power and usefulness of ANN have been demonstrated in various applications such as signal processing, pattern recognition, classification, function approximation, time series prediction, clustering, robotic control, etc. Neural networks can be classified according to the type of used units, the architecture and the learning method.

The most common type of artificial neuron is schematically depicted in Fig. 7.1. The neuron receives a number of inputs x_i coming from original data or from outputs of other neurons in the neural network. Each input channel has an associated weight, i.e. the incoming signal x_i is multiplied by the corresponding weight w_i. The weighted inputs are summed and the bias subtracted to create the neuron activation, y, which is passed through an activation function (transfer function) producing the output of the neuron. Such a model with the step activation function (binary threshold unit) was first proposed by McCulloch and Pitts in 1943 [68]. If the weighted input sum is greater than a certain threshold θ the neuron will "fire". In a recent applications, a majority of ANN uses sigmoid functions which are differentiable (needed for learning algorithms), smoothed versions of the step function. The bias may alternatively be introduced as an additional input with a fixed input value of -1 and a weight equal to the value of the bias. It allows for adjusting the actual bias value during the training process in which the input weights are modified to better approximate the desired function.

The architecture of the neural network defines the connectivity of neurons and their dynamics. There are two basic classes of architecture in neural network modeling: feed-forward and recurrent (feed-back). In feed-forward networks the signals are processed in one direction from input to output units. In the graph representing the connection pattern there are

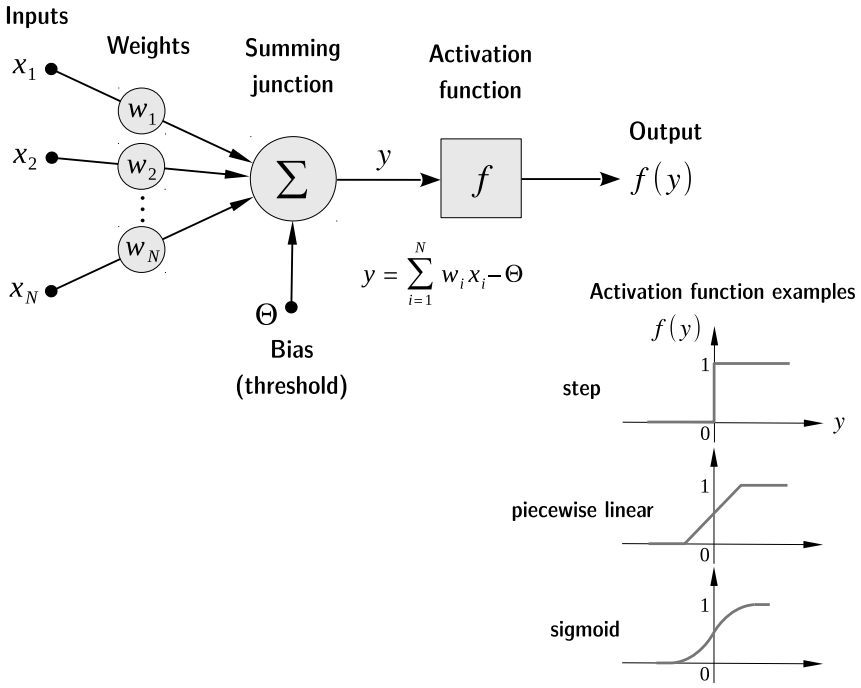

Figure 7.1: Working principle of an artificial neuron.

no loops. Neurons are usually arranged in layers and connections only exist from one layer to the next one. Inputs of the network are often also referred to as neurons even though they play no active role in the information processing. In recurrent networks the connections are bidirectional, the information flows not only in one direction from input to output but also in opposite direction. In particular, in the fully connected network, each neuron is connected to every other neuron. The topology of such networks contains loops due to feed-back connections.

Learning is the most important feature of artificial neural networks. There are three main paradigms of network learning: supervised, unsupervised, and hybrid learning [69]. In a supervised training the neural network is provided with inputs and the desired outputs. Response of the network to the inputs is measured. The weights are modified to reduce the difference between the actual and desired outputs (error signal). In a unsupervised training the network is supplied with only inputs and the desired output is unknown. The network adjusts its weights so that similar inputs generate similar outputs. The network identifies similarities and differences in the input data in a self-organizing manner, without external assistance. Hybrid learning is a combination of supervised and unsupervised learning. Different network architectures require appropriate training algorithms. The learning algorithm specifies how the weights and/or the connectivity between neurons are determined from the training data. One can distinguish four basic types of learning methods: error-correction, competitive, Hebbian, and Boltzmann learning [69].

Among the many neural networks that have been developed, the most popular are the perceptron and its generalization the multilayer perceptron (MLP). The perceptron, invented

by Frank Rosenblatt in 1958 [70], was the first neural network with the learning ability. It is a feed-forward network which consists of an input layer and an output layer of neurons (such as that described above). In the multilayer perceptron, between the input and output layers, there is an arbitrary number of neuron layers called hidden layers. An example of MLP structure is shown in Fig. 7.2.

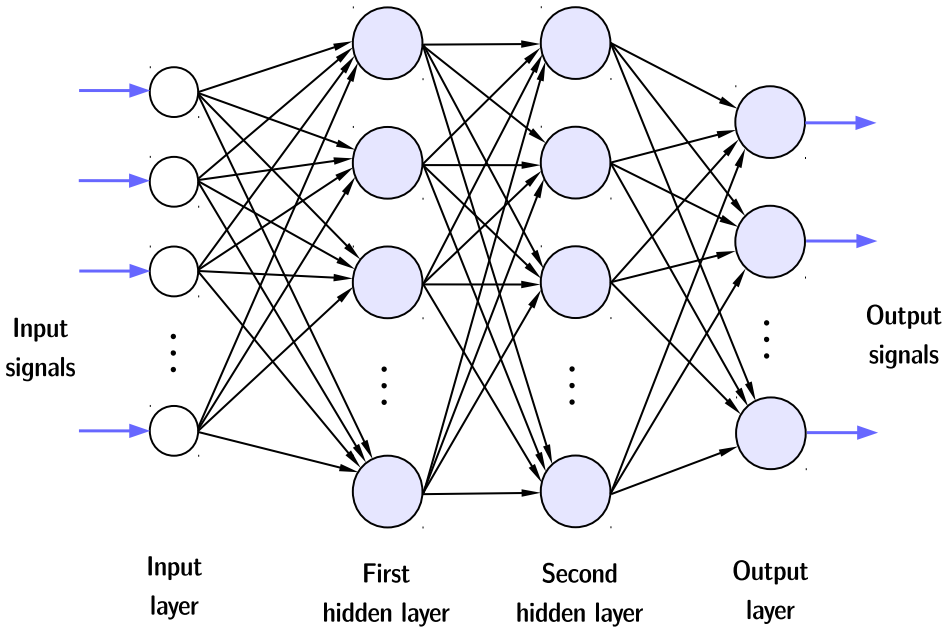

Figure 7.2: Architectural graph of a multilayer perceptron with two hidden layers.

Each single neuron of a given layer is fully connected to the neurons from the adjacent layers. There is no connection between nodes which are in the same layer. The training of MLP is performed with a supervised learning method. The backpropagation learning algorithm, based on the error-correction rule, is commonly applied to find the appropriate connection weights. It performs gradient descent to minimize the sum squared error between the actual and desired output values.

An example of self-organizing networks which use unsupervised learning is the Kohonen self-organizing map (SOM) [71]. Such a network is a valuable tool for clustering the input patterns into groups with similar features. It has been used in this work for the discrimination between signal and background events in the KRATTA telescopes. An introductory description of SOM features is given in the next section.

7.1.2 Self-organizing maps

The Kohonen self-organizing map performs nonlinear, topology preserving, projection from high-dimensional input space into a discrete low-dimensional feature space (cluster space) represented by a lattice of neurons. It is based on a single layer of neurons organized in a lattice of usually one or two dimensions. Exemplary neuron lattices are shown in Fig. 7.3.

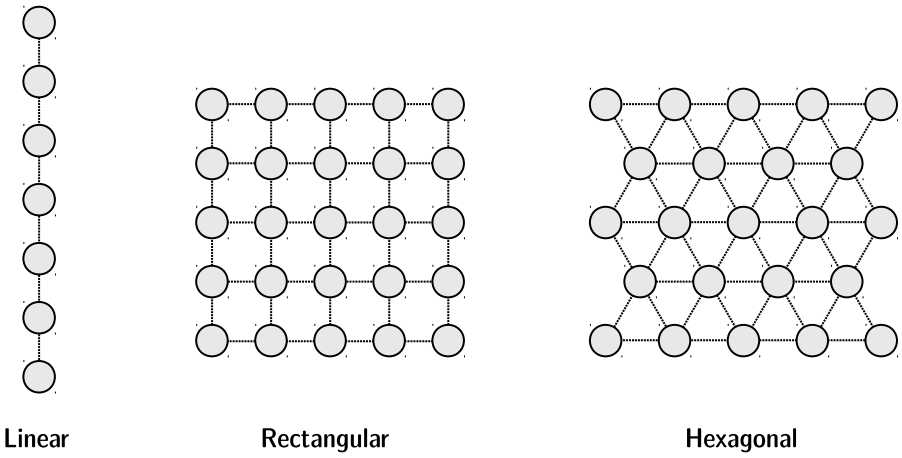

Figure 7.3: Typical neuron arrangements in self-organizing maps.

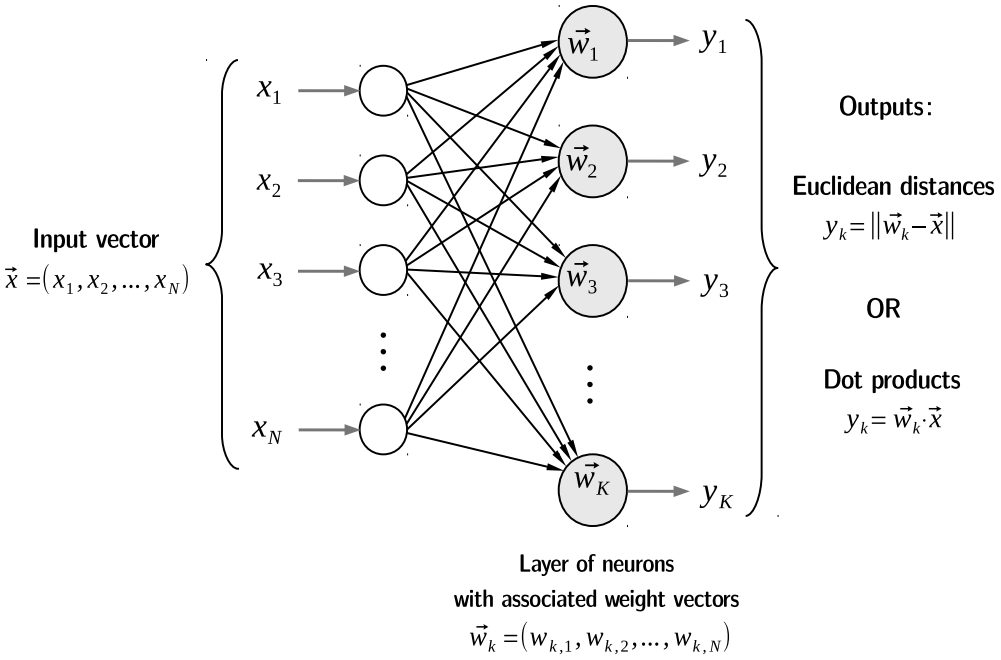

Figure 7.4: Schematic architecture of a one-dimensional self-organizing map.

Figure 7.4 illustrates the structure of a self-organizing map. Each neuron is only connected to the inputs and has an associated weight vector, $\vec{w}_k$, of the same dimension as the input vector, $\vec{x}$. The neuron output is a measure of similarity between the input vector and the weight vector. There are usually two methods to determine it. The first method uses the Euclidean distance between the two vectors. The second method uses the dot product and can be applied if the input and weight vectors are normalized.

The weights are tuned in the process of learning to organize them into a map representing similarities and differences between the input data items. The learning procedure can be briefly described as follows:

1 Initialize the weight vectors $\vec{w}_k$ to random numbers.

2 Present a randomly selected input vector $\vec{x}$ to the network and evaluate the network outputs.

3 Select the neuron with the weight vector most similar to the input (the winning neuron).

4 Update the weights of the winning neuron and neurons in its neighborhood by shifting them closer to the input vector according to $\vec{w}_k(i+1) = \vec{w}_k(i) + \eta(i)\delta(i,d)\,(\vec{x} - \vec{w}_k(i))$, where i is the iteration number, $\eta(i)$ is the learning rate, and $\delta(i,d)$ is a distance function on the lattice (the neighborhood function).

5 Repeat steps 2 through 4 until the results are sufficient or a maximum number of iterations is reached.

In such competitive learning, the output neurons compete among themselves to be activated (fired) in response to a given input pattern. A neuron which wins the competition is called the winning neuron or the best matching unit (BMU). The winning neuron is selected as the one whose weight vector is at the smallest Euclidean distance from the input vector (or the dot product of the two vectors is maximum). The weights of the BMU and neurons close to it are adjusted towards the input vector by forming a new weight vector which is a linear combination of the old weight vector and the input vector. The amount of adjustment depends on the degree of similarity between a neuron and the input, $(\vec{x} - \vec{w}_k(i))$, scaled by the learning rate $\eta(i)$ and the neighborhood function $\delta(i,d)$. The neighborhood function depends on the lattice distance from the BMU, d. In the simplest form, it may be assumed 1 for all neurons close enough to BMU and 0 for others. Usually, as the learning progresses, the learning rate decreases and the neighborhood function shrinks the neighborhood size.

After learning, neurons that are sensitive to similar input patterns are clustered together. When a new input data item is presented to the network, the location of the firing (winning) neuron in the lattice will indicate the dominant feature characteristic of the input.

7.1.3 Applications of neural networks to pulse shape analysis

Artificial neural networks have numerous applications in nuclear and particle physics, such as particle identification, track and vertex reconstruction, event selections, impact parameter (vector) determination in heavy ion collisions, energy calibration, reconstruction of invariant masses and and many others [72–82]. In particular, ANN have been especially useful for pulse shape analysis of detector signals. Pulse shape analysis (PSA) methods are usually used to discriminate between different types of radiations (γ rays, neutrons, electrons and heavier charged particles) by exploiting the dependence of the pulse shape on the ionization density

distribution. Other PSA applications include decomposition of complex signals (multiple hit events, signals from phoswich detectors and single chip telescopes), background noise rejection, and determining interaction points in the detector volume. Recently developed methods that are based on full digitization of the pulses with a fast waveform digitizer, provide more flexibility and precision than conventional analog pulse shape discrimination techniques. However, they are often very complex and time consuming. For this reason, it is desirable to use fast and efficient computational procedures such as, for instance, artificial neural networks. Below, some examples of neural network applications to digital PSA are shortly presented.

For the Heidelberg-Moscow-Experiment searching for neutrinoless double-beta decay, a background reduction method on the basis of multilayer perceptron was developed to distinguish between single interaction and multiple scattered events in germanium detectors [83]. The neural network consisted of three layers: an input layer with 180 neurons, a hidden layer with 90 neurons, and an output layer with a single neuron which serves as a pattern identifier. A supervised learning was performed using signal-like and background-like samples obtained with a ^{228}Th calibration source. A similar method for the same purpose was used within the GERDA project searching for the neutrinoles double-beta decay of ^{76}Ge [84, 85]. Identification efficiencies of $80 - 90\%$ were achieved for both event categories.

Another example concerns the possibility of using ANN to extract physical quantities from the signals coming from a liquid argon time projection chamber build for the ICARUS experiment located at the Laboratori Nazionali del Gran Sasso (LNGS, no longer operating) [86]. This work was motivated by the need of a fast analysis algorithm for on-line event selection. A previously used procedure, based on a least-squares fit of the signal using a theoretical analytical function, required a long time to minimize χ^2 over the free parameters. The applied neural network was a three-layer perceptron whose response to the input waveform samples consisted of the three quantities (pulse height, rise time, position in time) relevant for the analysis. Performed tests have shown that this approach provides satisfactory results, being one order of magnitude faster than the best-fit procedure.

Several investigations have been carried out on the digital pulse shape discrimination between neutrons and γ rays detected with organic scintillators, using methods based on a multilayer perceptron with back-propagation learning algorithm. [87–90]. They have achieved better discrimination accuracy (falling between $85 - 99\%$) and much faster performance than other PSA techniques. They also allow to recognize and reject fast-superimposed (pile-up) events, or to analyze them and recover the original superimposed components. In a recent article [91] concerning the same discrimination problem, the potential of two types of Kohonen neural networks, the linear vector quantization (LVQ) [92] and the self-organizing map, was investigated. Both networks are based on the Kohonen's competitive layer, but they differ in training procedures: the LVQ uses a supervised learning algorithm. They have shown high discrimination accuracy even at the lowest energy levels, however, the SOM is more accurate at classifying novel patterns from a data set.

An example of ANN hardware implementation for digital pulse shape analysis is reported in [93]. A neural network has been implemented in a FPGA device for fast on-line signal processing to provide information on isotope identification. Such a method allows to reduce the amount of data transfer and storage typical of PSA techniques.

The pulse shape analysis based on neural networks has been demonstrated as a valuable method for the discrimination of detector signals. Therefore, such a method has been intended for the recognition of background events in the KRATTA data.

7.2 Recognition of background events in KRATTA modules

The presence of background events (hits) in the KRATTA data and their origin was discussed in Sec. 6.3. The most substantial amount of background is observed in the ΔE-E identification map of scintillation signals for CsI1 vs CsI2, detected by PD1 and PD2. The background hits are distributed over a large area of the map and some of them lie on the isotope lines. The fraction of those hits within graphical cuts used for particle identification is significantly large, e.g., 43% for protons, 17% for α particles, and 79% for the weakly abundant ^{6}He. Thus, the recognition and rejection of such background events is of special importance.

The possibility of discrimination between the background and signal events by means of digital pulse shape analysis with the use of ANN was the subject of the present investigation. The most popular neural network used for pulse shape discrimination is the multilayer perceptron with a supervised backpropagation learning algorithm. Supervised learning requires a set of examples for which the desired network response is known, such as "background event" or "valid (signal) event". In our case, the hits adjacent to the isotope contours may be used as samples of background events. However, samples of signal events cannot be extracted from this identification map because of their overlapping with background hits. It has, therefore, been decided to employ the self-organizing map which learns in an unsupervised manner.

7.2.1 Pulse shape analysis with self-organizing map

Several preliminary tests have been performed to establish a possibly simple network structure suitable for this particular application. The chosen architecture of self-organizing map is presented in Fig. 7.5.

The network consists of neurons arranged linearly that calculate the similarity between the inputs and weights. The number of neurons was arbitrary set to $K = 1000$ in order to represent a large number of possible input patterns. The input vector $(x_1, x_2, ..., x_N)$ consists of a set of parameters describing the two PD1 and PD2 waveforms. Three alternative sets of parameters have been used: the signal samples, the waveform moments or the fitting parameters, all of which were defined in Sec. 6.2. The inputs are supplemented with an additional input x_0 with a constant value of 1. The input vector with this additional component is called the extended input vector and has been introduced for the following reason. In the applied procedure, the similarity between an input vector and a weight vector is measured by the difference in their directions (cosine similarity), which is insensitive to the vector magnitudes. However, to avoid ambiguities, different similarity values are required for different input vectors and the same weight vector, as well as for different weight vectors and the same input vector. This is ensured when the input and weight vectors are normalized. In our case the weight vectors are normalized but the input vectors should be left unnormalized to avoid reducing the feature variability in the input data set. Original (unnormalized) input vectors of the same direction but of different magnitudes may present different features, and this information would be lost after normalization. Using the extended input vectors allows to solve the problem of the contradictory requirements, since each extended input vector contains the original input vector and has a unique direction. This can be seen with the help of Fig. 7.6. Each input data point (x_1, x_2) can be fully specified only by the direction of its associated extended input vector $\vec{x}$.

The applied training procedure can be described as follows:

1 Initialize all weights $w_{k,n}$ with random values between 0 and 1 and normalize the weight

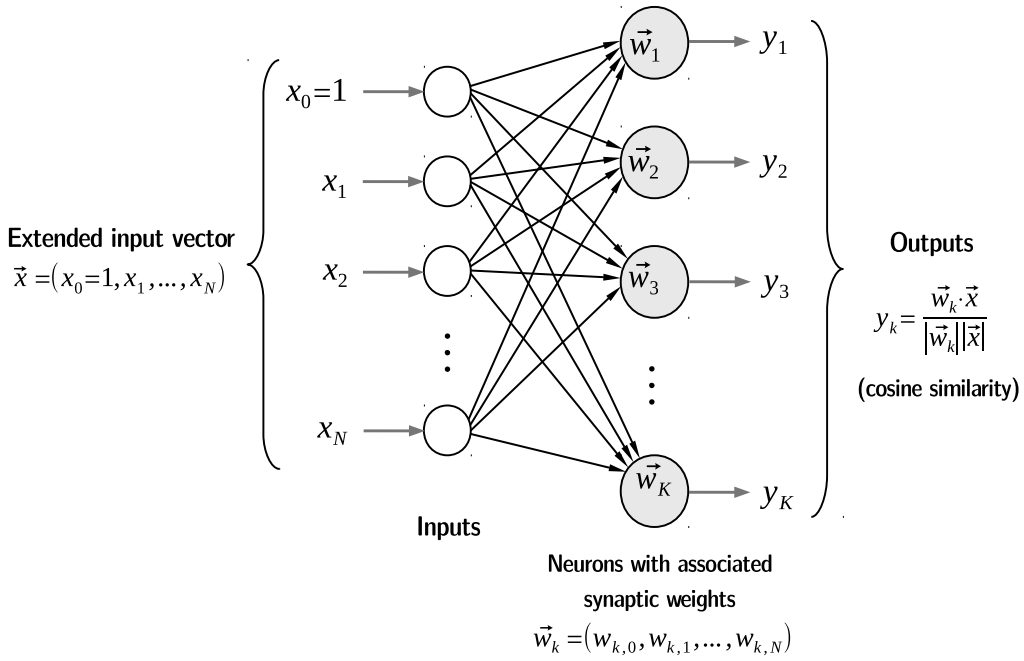

Figure 7.5: Scheme of the self-organizing map used for background recognition.

vectors $\vec{w}_k$.

2 Present an input vector $\vec{x}$ from the training data set to the network and compute the network outputs: $y_k = \frac{\vec{w}_k \cdot \vec{x}}{|\vec{x}|}$.

3 Select the neuron with the largest output value (winning neuron).

4 Update the weights of the winning neuron and neurons in its neighborhood according to
$\vec{w'}_k(i+1) = \vec{w}_k(i) + \eta(i)\delta(i,d)y_k(i)\frac{\vec{x}}{|\vec{x}|}$,
$\vec{w}_k(i+1) = \frac{\vec{w'}_k(i+1)}{|\vec{w'}_k(i+1)|}$,
where i is the iteration number, $\eta(i)$ is the learning rate, and $\delta(i,d)$ is the neighborhood function.

5 Repeat steps 2 through 4 until a maximum number of iterations is reached.

During the learning iterations the weight vectors of the BMU and its neighbors are adjusted towards the input vector. The amount of adjustment is controlled by the $\eta(i)$ and $\delta(i,d)$ parameters, which were kept constant (independent of i). The learning rate η was fixed at 0.6. The neighborhood function was set to the following values: $\delta(d=0)=1$ for the BMU, $\delta(d=1)=0.66$ for the nearest neighbors of the BMU, $\delta(d=2)=0.33$ for the second-nearest neighbors, $\delta(d=3)=0.08$ for the third-nearest ones, and zero for the others, $\delta(d>3)=0$.

The neural network model was trained for one million iterations using representative training samples from a given input data set. The procedure has been applied separately

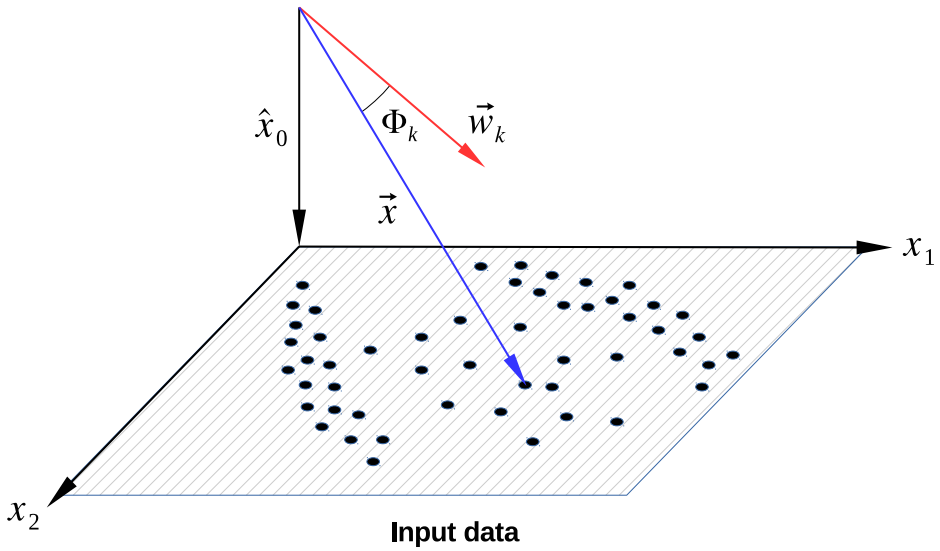

Figure 7.6: Illustration of the role of the additional input vector component, $\hat{x}_0$, presented for the case of two dimensional input vectors (x_1, x_2). Input data are represented by points located in the $x_1 - x_2$ plane. Each extended input vector $\vec{x} = (x_0 = 1, x_1, x_2)$ has a unique direction. When a data item is presented to the SOM, each neuron calculates the cosine similarity between its (normalized) weight vector $\vec{w}_k$ and the given extended input vector $\vec{x}$, which is equal to $\cos \Phi_k$.

for two subsets of the input events located in the $Z = 1$ and $Z = 2$ regions on the ΔE-E map with various parametrizations of the input waveforms. The left upper diagram of Fig. 7.7 shows the $Z = 2$ area which includes the ^{3}He, ^{4}He, ^{6}He isotope lines and adjacent background hits. The diagram below shows the mass identification spectrum obtained as the projection of events along the isotope identification lines.

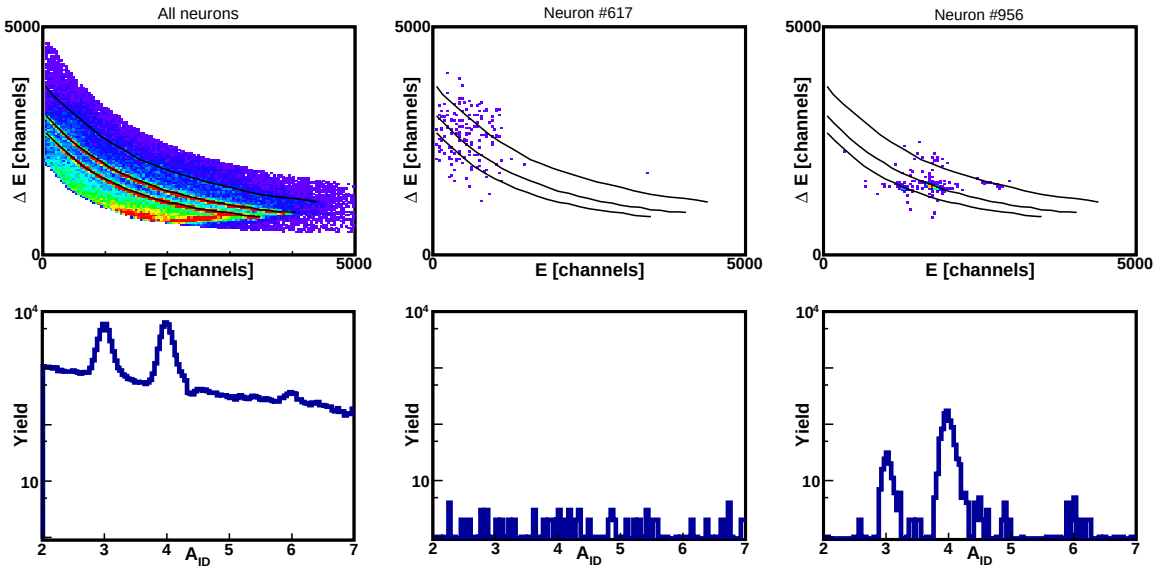

Figure 7.7: Distributions of events on the ΔE-E map (the upper panel) and their projections along the helium isotopic lines (the bottom panel). The left column presents all the examined data events, the middle column - events which activate a background sensitive neuron, the right column - events which activate a signal sensitive neuron.

After training, some neurons are expected to be sensitive to background hits and some others to relevant signals. Usually, as in our case, a perfect separation between different classes is not achieved. There are also neurons responding to events from the two different categories. Identification of neurons with particular activity patterns was performed by examining their corresponding mass identification spectra. As an example, the middle column in Fig. 7.7 presents the distribution of events which activated one particular neuron. Since the distribution shows no significant enhancements along the isotope calibration lines, this neuron was classified as exclusively sensitive to the background. Another example, shown in the right panel, concerns a neuron sensitive to signal events. Its mass spectrum exhibits distinct isotope peaks.

The background reduction method in our analysis relies on the rejection of events that activate only the neurons identified as exclusively sensitive to the background. Such a criterion was used in order to minimize valid event losses. Figure 7.8 presents the effect of the background reduction for the case when the SOM was trained with events from the $Z = 2$ region (as shown in Fig. 7.7) and the input vectors were specified as the amplitude ratios of the slow component to the fast component of light from CsI1 and CsI2. Although the network was trained with the $Z = 2$ events, it is instructive to see the result of the background reduction when all the input data are presented to the network. The distribution of those events on the ΔE-E map is displayed in the diagram (a) of Fig. 7.8. The diagram (b) shows the

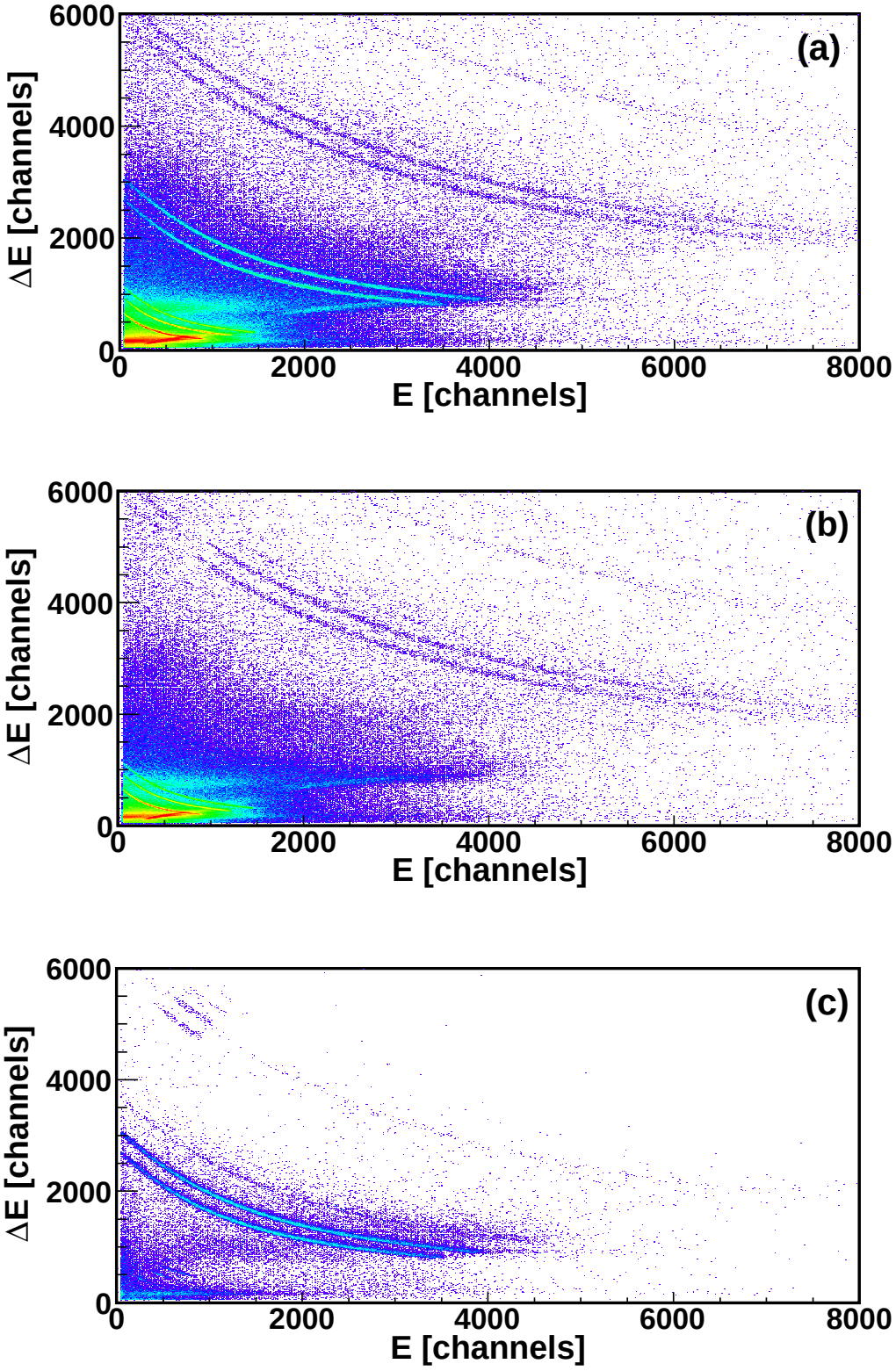

Figure 7.8: Distributions of events on the ΔE-E (CsI1 vs CsI2) identification maps: (a) events presented to the SOM, (b) events recognized as background, (c) remaining events after the background rejection. The network was trained with event samples from the $Z = 2$ area of the map (see text for details).

distribution of events recognized as background, while the diagram (c) is the map of events left after subtracting the background. This map reveals an efficient background reduction for the helium isotopes, which was the aim of the SOM with such training. In particular, the ^{6}He line becomes clearly visible. In the entire map (a), on the lower right of the $Z = 2$ lines, one can see a line with punch-through events. These events were removed together with background events, which is a valuable feature of the method. Another observation is that most of the $Z = 1$ and $Z = 3$ events (not represented in the training set) were recognized as background. This confirms the desirability of dividing the input data into smaller groups for a better discrimination between background and signal patterns.

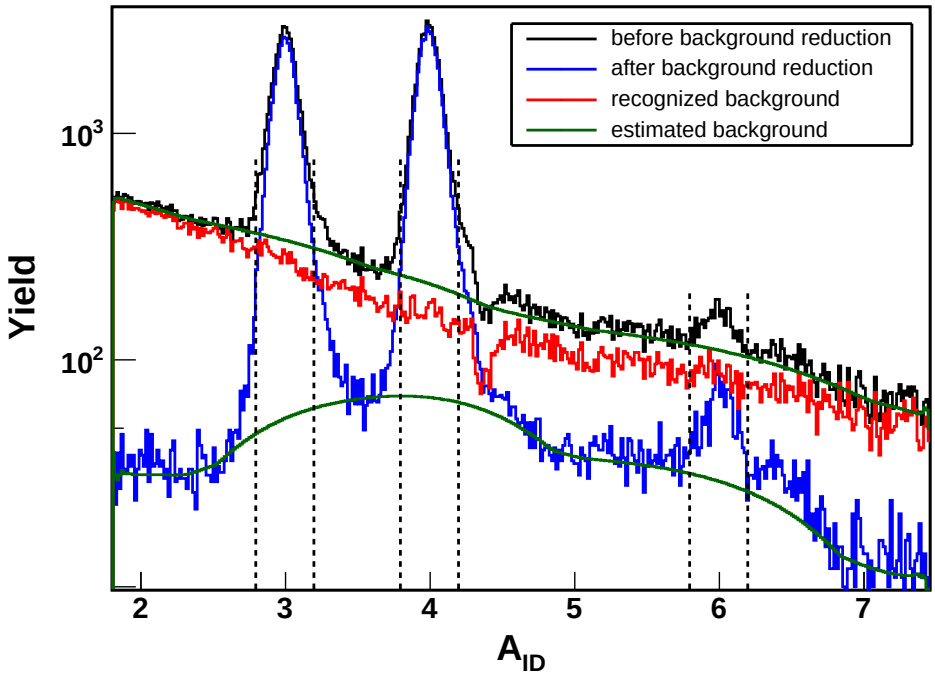

Figure 7.9: Mass identification spectra of helium isotopes before and after the background reduction. The smooth lines show the estimated background continuum.

Figure 7.9 shows the mass identification spectra of He isotopes before and after the background reduction. The background contribution to each peak can be quantitatively characterized by the background fraction $BF = B/(B+S)$ or the signal to total ratio $STR = 1-BF = S/(B+S)$, where B is the estimated number of background events and $(B+S)$ is the total number of events within the peak area. The background spectra were estimated with the `TSpectrum` procedure from the ROOT library [94] which is based on the Statistics-sensitive Nonlinear Iterative Peak-clipping algorithm, SNIP [95]. This algorithm uses a digital filter to approximate the background continuum underneath peak regions, simultaneously smoothing the spectrum. The widths of the peak areas were set to their double FWHM and are indicated in the figure by the vertical lines. In the presented case, the STR values for the ^{3}He, ^{4}He, ^{6}He peaks were 0.75, 0.83, 0.21 in the measured spectrum and 0.95, 0.94, 0.46 after the

background reduction, respectively. It means that the local background level was reduced by a factor of 6.3 for ^{3}He and about 3.2 for ^{4}He, ^{6}He isotopes, which is a satisfactory result.

7.2.2 Performance tests and discussion

The learning effectiveness and performance of the SOM depends on the form of representing the input data (PD1 and PD2 waveforms). The results of tests for He isotopes with various input data characterizations are collected in Table 7.1. The input vectors were composed of the waveform samples (Test 1), the waveform moments (Test 2), the parameters of the fitted scintillation components i.e. the fast and slow component amplitudes and the fast fall time (Test 3), and the fast component to slow component amplitude ratios (Test 4). The best results were obtained with the fast to slow amplitude ratios. In this case the background was reduced by 85% for ^{3}He and by about 70% for the other isotopes.

Table 7.1: Signal to total ratio (STR) obtained with the SOM for He isotopes using various characteristics of the input waveforms.

	STR [%]			
	^{3}He	^{4}He	^{6}He	Mean
Initial value	75	83	21	60
Test 1 - Waveform samples	84	86	23	64
Test 2 - Waveform moments	90	91	35	72
Test 3 - Fit parameters	93	92	39	75
Test 4 - Fast/Slow amplitude ratios	**95**	**94**	**46**	**78**

Similar tests were also performed for $Z = 1$ isotopes. Again, the best results were obtained with the fast to slow amplitude ratios (Table 7.2). The background contribution was reduced by about 60% for protons, and 45% for deuterons and tritons. The effectiveness of the SOM for these species is significantly lower than for He isotopes. Presumably, the reason is that this low energy region of the ΔE-E map contains strong contributions from various types of background and punch-through events. Consequently, it is more difficult to differentiate between them and the signal patterns.

Table 7.2: Exemplary results from the SOM tests performed for hydrogen (p,d,t) isotopes.

	STR [%]			
	p	d	t	Mean
Initial value	57	65	65	62
Test 5 - Waveform moments	70	75	76	74
Test 6 - Fast/Slow amplitude ratios	77	77	77	77

For the above tests, the self-organizing map was trained with samples representative of either the $Z = 1$ or $Z = 2$ area of the ΔE-E map. Such a training set contains events

from the isotopic lines and from the surrounding neighborhood. The option with learning sets restricted to events lying on the isotope lines was also checked. The obtained results were generally somewhat worse - the STR values dropped by $1-3\%$.

It has also been investigated whether the random initialization of neuron weights has an influence on the network performance. The Test 2 was repeated four times by varying the initial weight values. The results of these calculations are summarized in Table 7.3. The variations of the obtained STR values are negligible, so that one can conclude that the results are stable with respect to the choice of initial weights.

Table 7.3: Repetitions of the Test 2, each test carried out with a different set of initial weights.

	STR [%]			
	^{3}He	^{4}He	^{6}He	Mean
Initial value	75.3	83.3	20.8	59.8
Test 2-1	90.4	91.0	35.2	72.2
Test 2-2	89.9	90.6	34.2	71.6
Test 2-3	90.8	91.3	36.1	72.7
Test 2-4	90.4	91.0	35.6	72.3

The tests have shown that an efficient recognition of background events (together with punch-through events) can be obtained by using the amplitudes of the scintillation components as the waveform characteristics. In particular, the input vector can be reduced to only two variables, the Fast/Slow amplitude ratios. It indicates that an alternative method of background reduction may be based on examining two-dimensional correlations between combinations of the amplitudes. Such a possibility has been investigated and it was found that the correlation map displayed in Fig. 7.10 is especially useful for the purpose of background discrimination [96]. It shows the logarithm of the amplitude from the thin crystal as a function of the Slow-to-Fast amplitude ratio in the thick crystal. In this representation the punch-through events are grouped in clusters located in the right part of the map. Applying the shown graphical cuts permits to isolate them, as well as a substantial amount of background hits, from the regular hits of particles stopped in the thick crystal. This procedure presents a performance similar to that provided by the SOM. It has been used as a supplementary method for heavier isotopes and particles stopped in the thin crystal. The latter application uses the correlation between the summed PD0+PD1 ionization components and the Slow over Fast component of light in CsI1.

The simple and efficient method of background reduction based on the correlation maps can be used if the measured waveforms are decomposed by using the fitting procedure described in Sec. 6.2.4 However, this multidimensional minimization procedure requires a very long computation time. In addition, some supervision is necessary due to the local minima problem - unphysical results must be identified and corrected. In this context, the major advantage of the self-organizing map is the possibility of using raw waveform characteristics (e.g. the waveform moments) for the pulse shape analysis. It opens the perspective of eliminating the time consuming fitting procedure, since the isotope identification and energy calibration can also be performed with the raw data. It would reduce the processing time by at least an order of magnitude. Moreover, instead of acquiring the whole waveforms, a fast on-line

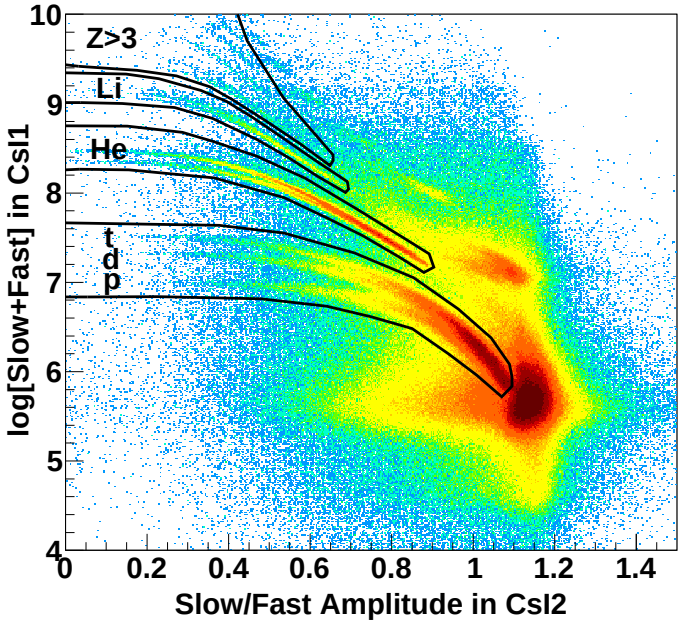

Figure 7.10: Logarithm of the total light in the thin crystal vs Slow over Fast component of light in the thick crystal. The lines define borders of the regions of well identified particles (inside the cuts).

preprocessing can be applied to extract relevant information in the form of a small set of waveform parameters. It will greatly reduce the amount of data transferred to the acquisition system and the storage volume.

Although the SOM performance is worse in the case of using the raw waveform parameters, it can be improved in many aspects. In particular, the tests have shown that the performance decreases with an increasing number of input components. This seems to be an evidence that the learning process is not fully effective. For a better learning outcome, the learning rate and the neighborhood range should decrease gradually with the training iterations. Also, changing the neuron arrangement into a two-dimensional lattice may lead to more refined feature selection. Another improvement is possible by applying the SOM to individual isotopes separately. These issues should be addressed in further investigations.

In the present studies the number of neurons in the SOM was set to a large value of 1000 for all the input data sets and input vector characterizations. Such a choice was motivated by the fact that too few neurons in a large dataset may result in a loss of some patterns. On the other hand, a too large value of neurons increases the computation time without revealing any new information. In order to minimize the number of neurons for a specified input data set, additional tests will also be required.

For the needs of the present data analysis the SOM results, obtained with the support of the fitting and decomposition procedure, were sufficiently satisfactory. A significant background reduction was achieved on the event-by-event basis. Corrections for the remaining background were estimated and used in further steps of the data analysis for determining the isotope yields.

Chapter 8

Secondary reactions and scatterings in detector material

Secondary reactions in the scintillation crystals, as well as scatterings (Coulomb multi-scattering) leading to particle escape from the crystal, constitute the main contribution to the background observed in the KRATTA identification maps. Such background events have to be rejected, with the effect that the particle yields are significantly underestimated. The required correction factors were calculated on the basis of Monte Carlo simulations performed with the Geant4 toolkit [97] within the FairRoot framework [98].

The detection of particles with solid state detectors is possible due to the interaction between the measured particle and the material of active elements of the detector. There are two main features which characterize the passage of charged particles through the matter: the energy lost by the particle and the deviation from its initial direction of motion. Both effects are caused by the particle interaction with the material along its track. The main interaction processes are inelastic collisions with the atomic electrons of the material and elastic scattering from nuclei [99], and also nuclear reactions in the case of energetic particles. The electronic energy loss is exploited for the detection and identification, while nuclear scatterings and reactions are the disturbing effects that are of special interest here.

Figure 8.1 presents the visualization of the experimental setup with tracks of reaction products emerging from the target. Figure 8.2 presents a geometrical model of the KRATTA single module active elements. For the purpose of determining the probabilities of secondary reactions and scatterings in KRATTA scintillation crystals, the simulations were performed with a single module for different particles generated at the target location and directed to the module. The particle directions were randomly distributed over the detector solid angle. Only the scintillation crystals were enabled in the simulations, and the following processes have been taken into account: the electronic energy loss, multiple scattering and hadronic interactions. The simulations were performed separately for hydrogen and helium isotopes ($p, d, t, {}^3\mathrm{He}, \alpha$), for 20-30 values of the particle kinetic energy, E_{kin}, in the relevant energy range. For each particle type and each energy, 10^4 events were simulated.

As a result of such simulations one gets the value of the energy deposited in each scintillator. For particles stopped without any reaction along its path, the sum of the energies deposited in both scintillators should be equal to the entrance kinetic energy, $E_{kin} = \Delta E + E$. Other cases indicate abnormal energy loss due to a secondary reaction or scattering leading to escape from the crystal. The ratio of the number of reaction and scattering events with respect to the total number of simulated events represents the reaction/scattering probability

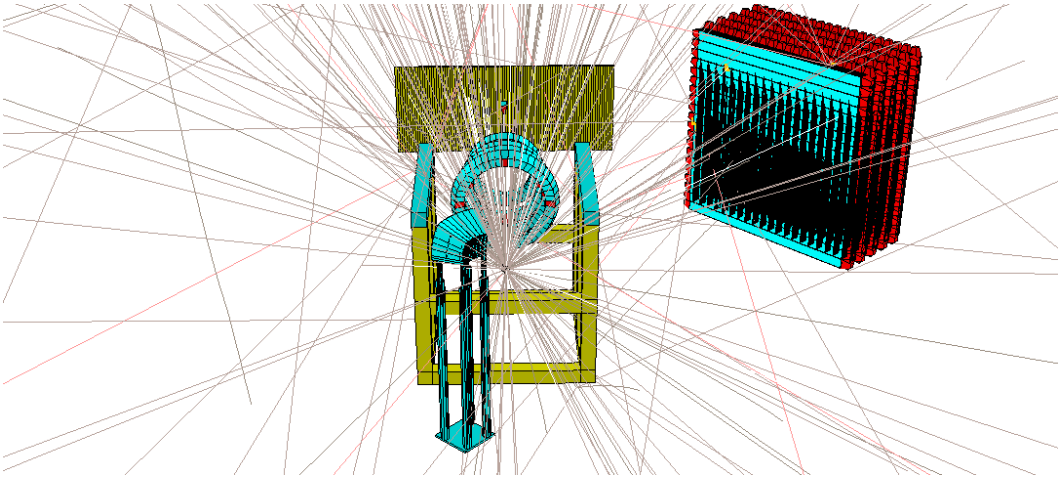

Figure 8.1: Model of the ASY-EOS experimental setup used in the Monte Carlo simulations. The light color lines show the paths of simulated reaction products coming from the target. The KRATTA detector with its support is visible on the left of the interaction point, the CHIMERA rings and ATOF Wall are along the beam direction, and the LAND detector is on the right-hand side.

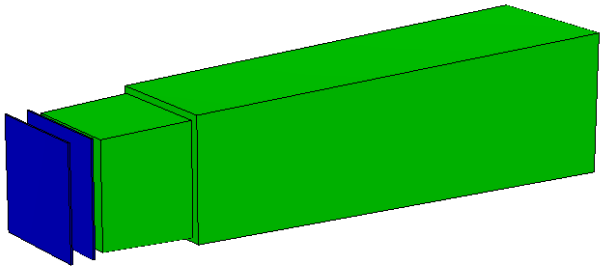

Figure 8.2: Geometrical model of the KRATTA module active elements - silicon photodiodes (blue) and CsI crystals (green).

in the CsI crystals, $P = P(E_{kin})$, for a given initial kinetic energy.

The results of simulations for deuterons with incident kinetic energies $E_{kin} = 200$ MeV are presented in Fig. 8.3. Each point in the ΔE-E representation in the top panel corresponds to one simulated event. Three main groups of points can be distinguished. The points located on the vertical line represent particles that have reacted in the thin crystal and did not deposit energy in the thick crystal ($E = 0$). The points forming the horizontal line represent deuterons that reacted in the thick crystal or escaped from it due to scattering without depositing their total initial energy. The group of events in which deuterons were stopped in the crystal without reactions is indicated by the red arrow. These events are somewhat spread along a line due to energy straggling in the first crystal. The projection of the distribution onto the E axis is presented in the panel below. The three panels on the right show exemplary events corresponding to the three cases discussed, together with a geometrical view of the crystals. Secondary reactions and scattering affect the ΔE-E plot by forming a contribution to the background.

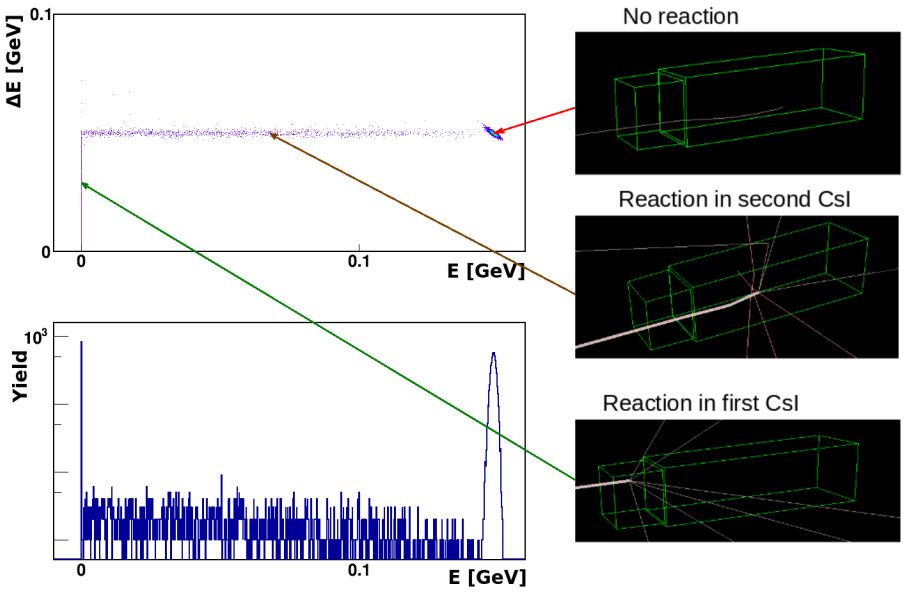

Figure 8.3: ΔE-E plot obtained as a result of simulations (10^4 entries) for deuterons with initial energy $E_{kin} = 200$ MeV and its projection onto the axis of the energy E deposited in the second crystal.

Figure 8.4 shows the estimated reaction/scattering probability $P = P(E_{kin})$ for light charged particles. The results were parametrized by fitting a second-order polynomial:

$$P(E_{kin}) = p_0 + p_1 E_{kin} + p_2 E_{kin}^2, \tag{8.1}$$

with parameters p_0, p_1 and p_2. Obviously, the parameter p_0 should be zero, however, better fit results (χ^2) were obtained for relevant energy ranges when this parameter was introduced. The results of the parametrizations are presented in Table 8.1.

The experimental energy spectra were corrected according to the obtained $P(E_{kin})$ distributions. As an example, Fig. 8.5 shows the effect of the corrections of the energy distribution

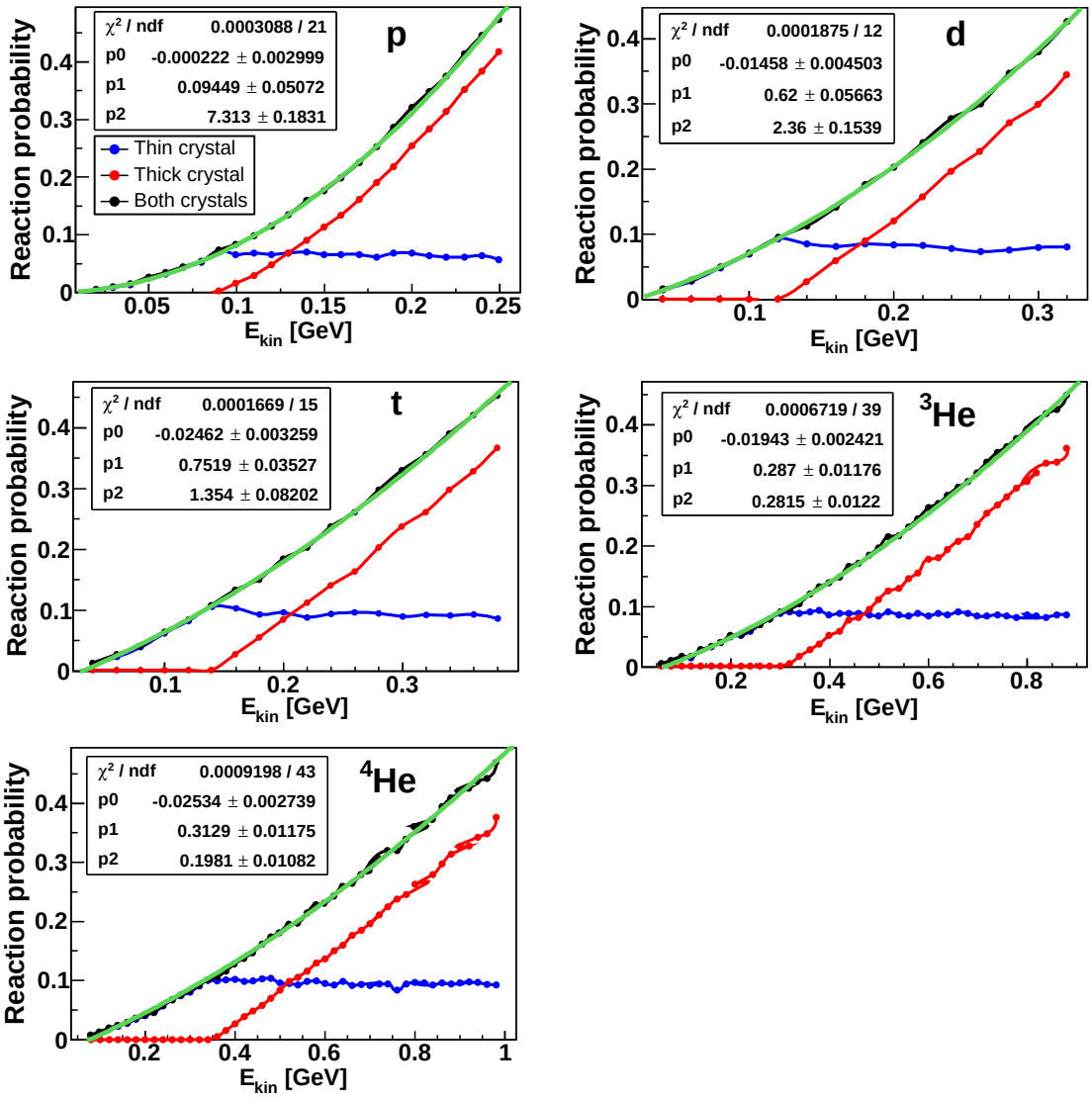

Figure 8.4: The reaction/scattering probability as a function of the particle entrance kinetic energy for light charged particles. The green lines are fits with a second order polynomial.

Table 8.1: The second order polynomial coefficients obtained from the fitting procedure for the reaction/scattering probability parametrizations.

particle	p_0	$\Delta\ p_0$	p_1	$\Delta\ p_1$	p_2	$\Delta\ p_2$	Valid up to E_{kin}/A [MeV]
proton	-0.0002	± 0.0030	0.095	± 0.051	7.31	± 0.19	250
deuteron	-0.0146	± 0.0046	0.620	± 0.005	2.36	± 0.16	160
triton	-0.0246	± 0.0033	0.752	± 0.036	1.354	± 0.083	126
^{3}He	-0.0194	± 0.0025	0.287	± 0.012	0.282	± 0.013	213
α	-0.0253	± 0.0028	0.313	± 0.012	0.192	± 0.011	245

of alpha particles. The correction factor $(1 - P(E_{kin}))^{-1}$ is systematically growing with the kinetic energy, reaching a value of about 2 at 1 GeV.

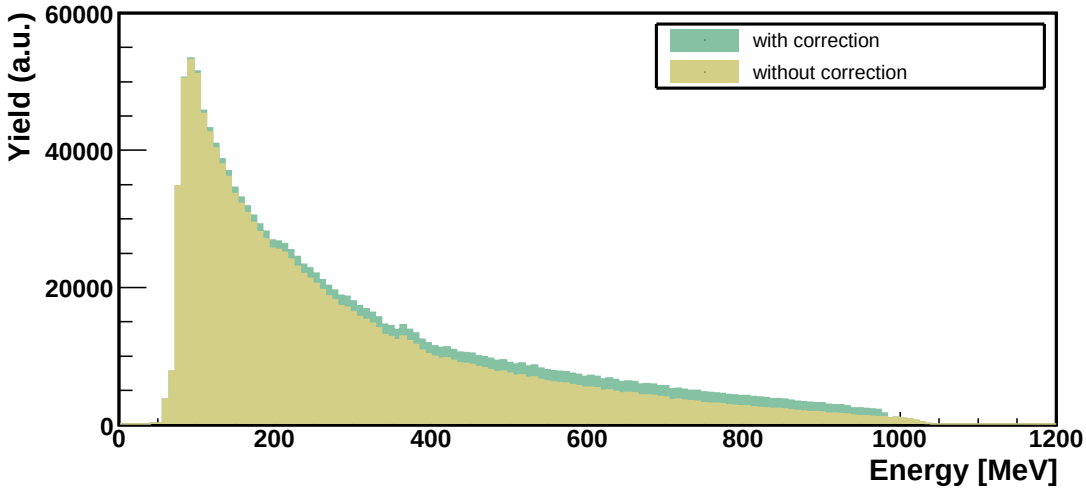

Figure 8.5: Energy spectrum of alpha particles before and after applying corrections for secondary reactions and scattering.

The simulations also allowed to determine the total energy deposition, i.e. the sum of the energy deposited by the primary particle and by all the secondary reaction products. The average total energy deposit for incident neutrons and light charged particles as a function of their entrance kinetic energy, E_{kin}, is shown in Fig. 8.6. For charged particles, the relation is nearly one-to-one at low incident energies. As the incident energy increases the dependence becomes flatter because the reaction probability increases, and near the punch-through energy a sudden drop is observed. The left-top panel presents the results of simulations performed for neutrons to establish how these neutral particles can affect the KRATTA data. The energy deposition even for fast neutrons is relatively small, which indicates that the background events generated by neutrons are located on the ΔE-E plot below the proton line near the bottom of the map.

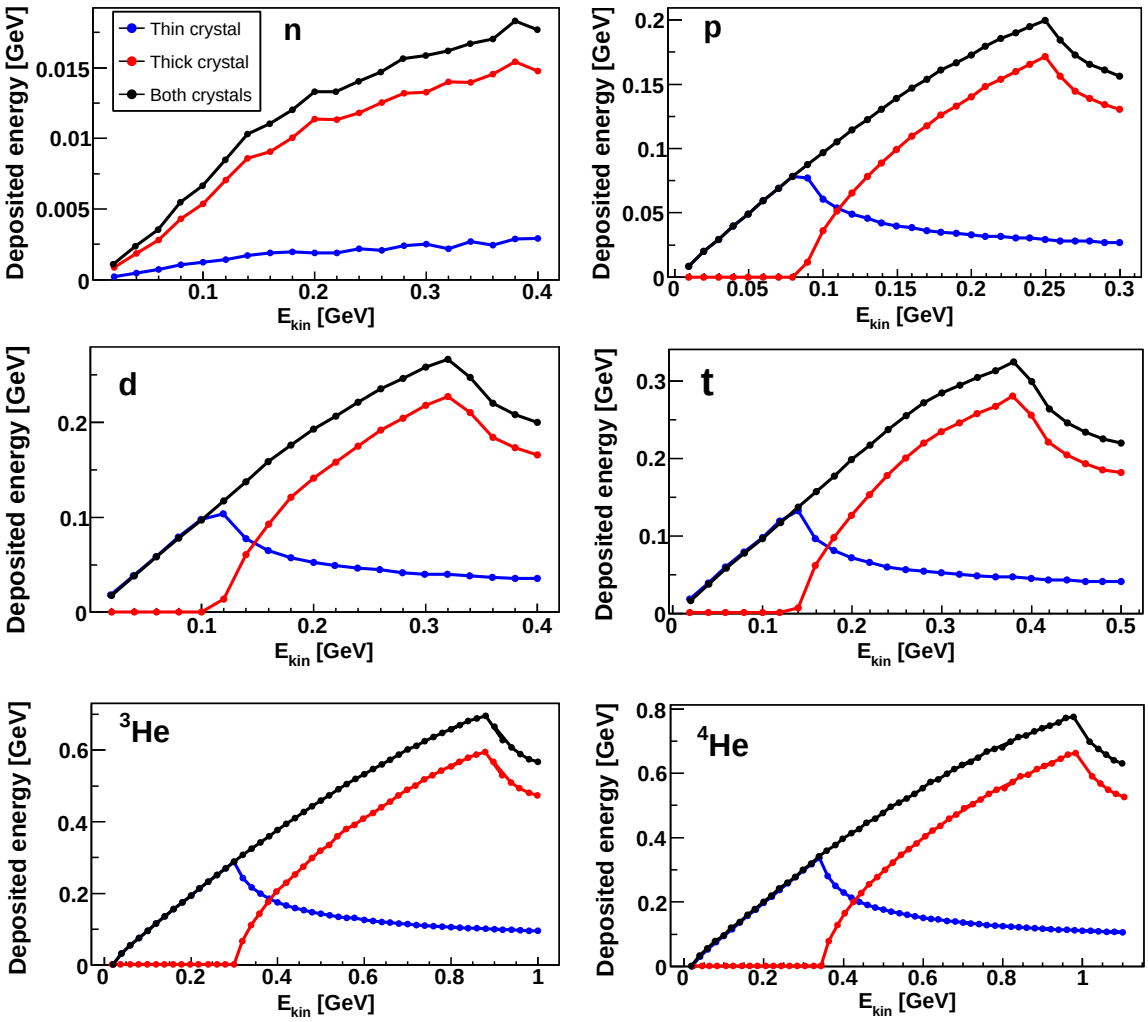

Figure 8.6: The average total energy deposit in CsI crystals for neutrons and light charged particles as a function of the entrance particle kinetic energy.

By applying the experimental inverse energy calibration, the simulated spectra can be represented in raw experimental channels. This allows for direct comparisons between the simulated and experimental distributions and is particularly useful in identifying various sources of background in the experimental maps. Comparing the right panel of Fig. 8.7 with its experimental counterpart in Fig. 6.15 one can see that a substantial amount of background observed in the experimental map can be reproduced with the simulations by taking into account the secondary reactions/scatterings in the CsI crystals. A similar conclusion can be drawn by comparing the left panel of Fig. 8.7 with the lower left quarter (up to $Z = 2$) of the experimental map in Fig. 6.11. The simulations reproduce not only the isotopic lines but also the punch-through segments as well as the background events. The characteristic points (punch-through) are located almost at the same positions.

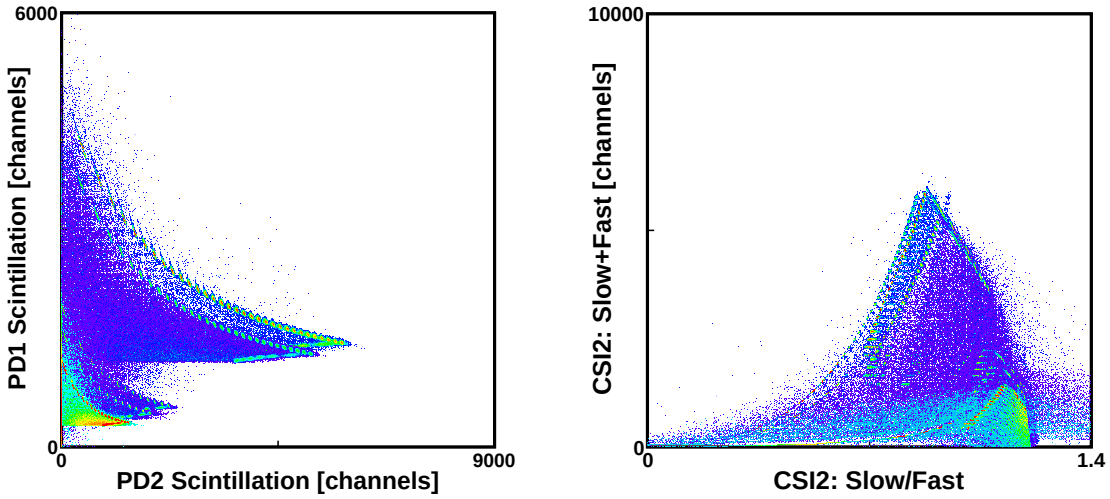

Figure 8.7: Identification maps obtained from Monte Carlo simulations after converting the energy losses into the experimental channels using the inverse energy calibration and the light-energy conversion formula. The left panel presents the simulated ΔE-E map, to be compared with its experimental counterpart in Fig. 6.11. The right panel shows the simulated total light versus the slow over fast ratio identification map, to be compared with the experimental map of Fig. 6.15.

Chapter 9

Global event characteristics

The data analysis requires information on some global event characteristics, such as the impact parameter and the reaction plane orientation. Their experimental estimates were based on the data provided by the CHIMERA and ATOF detectors. The impact parameter permits to classify events according to the collision centrality. The knowledge of the reaction plane orientation is necessary to determine the flow parameters.

9.1 Impact parameter

The performed simulations with the UrQMD model have shown, that the two global variables, Z_{Bound} and Z_{Rat}, constructed from the CHIMERA and ATOF data, can serve as impact parameter selectors [14]. The total bound charge, Z_{Bound}, and the ratio of transverse to longitudinal charge, Z_{Rat}, are defined as:

$$Z_{Bound} = \sum_{i=1}^{N} Z_i \quad \text{for} \quad Z_i \geqslant 2, \tag{9.1}$$

$$Z_{Rat} = 10 \cdot \frac{Z_{Trans}}{Z_{Long}}, \tag{9.2}$$

with

$$\begin{aligned} Z_{Trans} &= \sum_{i=1}^{N} Z_i \cdot \sin^2(\theta_i), \\ Z_{Long} &= \sum_{i=1}^{N} Z_i \cdot \cos^2(\theta_i), \end{aligned}$$

where Z_i and θ_i are the charge (atomic number) and the laboratory polar angle of the i^{th} particle, respectively.

The experimental distribution of Z_{Bound} versus Z_{Rat} for the Au+Au collisions at 400 MeV/nucleon is presented in panel (a) of Fig. 9.1. As expected, these two quantities are anti-correlated: Z_{Bound} increases while Z_{Rat} decreases with increasing impact parameter. The corresponding distribution obtained from UrQMD simulations is given in panel (c). For comparison, the ridge line of this distribution (with black stars) is drawn into the experimental distribution. The patterns of the two distributions are very similar. Some of the observed

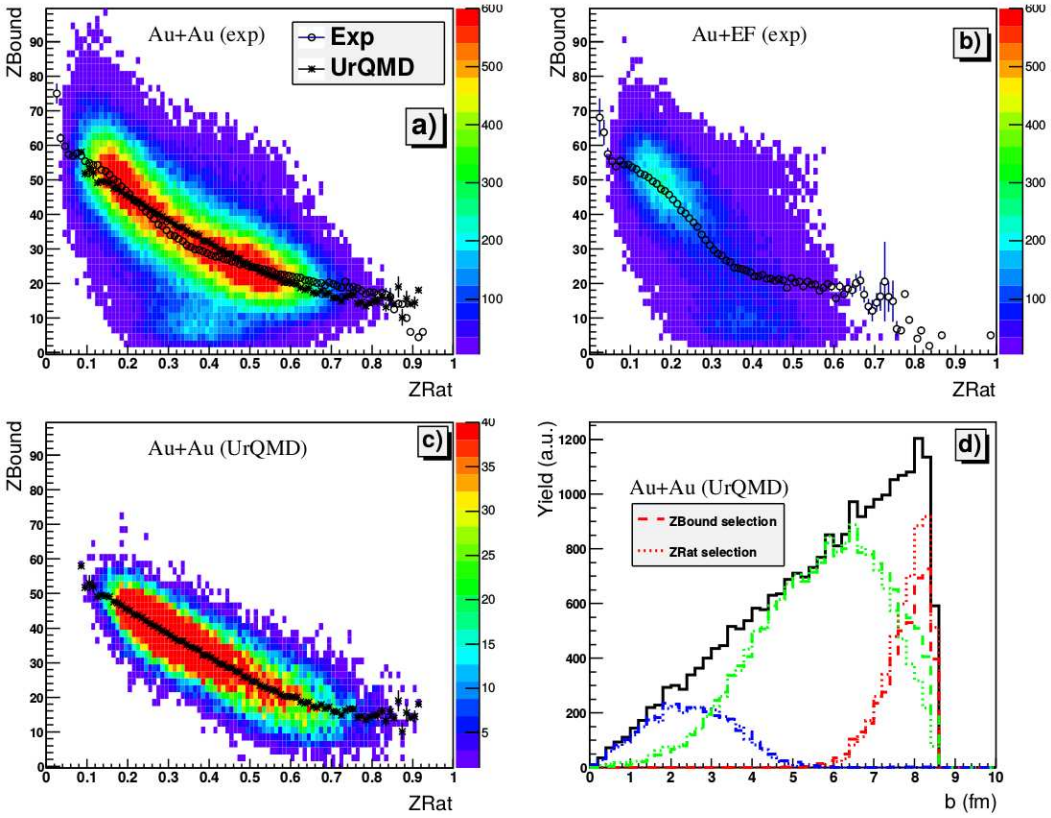

Figure 9.1: Top row: Experimental Z_{Bound} vs Z_{Rat} correlation for data taken with (a) and without (b) a target (EF - Empty Frame). Bottom row: UrQMD calculations for Au+Au collisions at 400 MeV/nucleon, filtered by the experimental acceptance. The correlation of Z_{Bound} vs Z_{Rat} for the impact parameter $b < 8.5$ fm is shown in panel (c). The black histogram in panel (d) shows the impact parameter distribution for all the simulated events. The blue, green and red lines show impact parameter distributions when selecting $b < 3$ fm, $3 < b < 7.5$ fm, and $b > 7.5$ fm, respectively, by gating on Z_{Bound} (dashed) and Z_{Rat} (dotted). The ridge line of the simulated distribution (c) is superimposed onto the experimental distribution (a). Reprinted from [14].

differences can be explained by the fact that the experimental distribution contains a contribution from non-target events, which come from reactions of Au on light nuclei such as N and O from the air and possibly Al from the target frame. The Z_{Bound} versus Z_{Rat} correlation for such events is shown in panel (b). The estimated efficiencies of the impact parameter selections are illustrated in panel (d). Some of the impact parameter windows and the corresponding Z_{Bound} and Z_{Rat} limits are given in Table 9.1.

Table 9.1: Impact parameter b and its selectors Z_{Bound} and Z_{Rat}.

b interval [fm]	Z_{Bound}^{Min}	Z_{Bound}^{Max}	Z_{Rat}^{Min}	Z_{Rat}^{Max}
(0, 3)	0.0	18.0	0.600	2.000
(0, 7.5)	0.0	44.5	0.245	2.000
(0.25, 0.45)	18.5	34.0	0.365	0.585
(5.5, 7.5)	31.0	44.5	0.245	0.420

9.2 Reaction plane orientation

The experimental estimate of the azimuthal orientation of the reaction plane was constructed from the CHIMERA and ATOF data using the Q-vector method [100]. The Q-vector was calculated as

$$\vec{Q} = \sum_{i=1}^{N} Z_i \vec{\beta}_{\perp i} \gamma_i, \tag{9.3}$$

where Z_i is the atomic number, $\vec{\beta}_{\perp i}$ is the transverse velocity vector, and γ_i is the Lorentz factor of the i^{th} particle. The vector Q represents a direction in the plane perpendicular to the beam axis, which is strongly correlated with the azimuthal orientation of the reaction plane. In the analysis of CHIMERA events, at least four identified particles with rapidities $y_i^{CM} > 0.1$ were required. The ATOF detector covered forward angles ($\theta < 7°$) and thus it was able to register projectile-like fragments from peripheral collisions. Such heavy fragments are expected to have the best memory of the entrance channel reaction plane.

The red histogram in Fig. 9.2 shows the inclusive distribution of the estimated azimuthal angle of the reaction plane (Q-vector azimuthal angle) obtained from the data of both detectors, i.e. by summing over recorded hits in CHIMERA and ATOF. Some deviations from the azimuthal uniformity are observed. They are related to azimuthal asymmetries in the detection system, particularly in the ATOF detector. For the purpose of the flow analysis, the distribution was corrected by weighting events with appropriate factors.

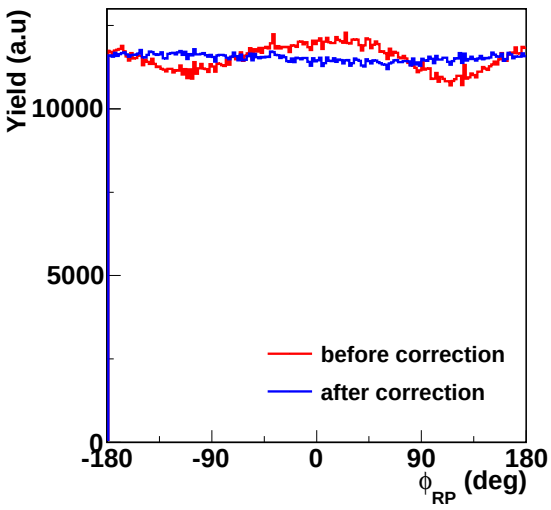

Figure 9.2: Distribution of the estimated azimuthal angle, ϕ_{RP}, of the reaction plane before (red) and after (blue) corrections.

Chapter 10

Rejection of non-target events

In order to recognize and reject events due to the reactions of Au projectiles with non-target material, the correlation between the Q-vector orientations obtained from the CHIMERA data and from the μ-Ball data was used. Figure 10.1 presents the correlation between the $\vec{Q}_{\mathrm{CHI}}$ and $\vec{Q}_{\mu\text{-Ball}}$ azimuthal directions, ϕ_{CHI} and $\phi_{\mu\text{-Ball}}$, from measurements with (top left) and without (top right) the target. As expected, a strong anti-correlation for on-target reactions is observed, since CHIMERA covers the forward hemisphere while the μ-Ball mainly the backward hemisphere in the CM frame. In the case of empty frame runs only a weak positive correlation is observed. The bottom panel shows the distribution of the differences between the two Q-vector orientations. To minimize the contribution of non-target reactions, the anti-correlation condition $|\phi_{\mathrm{CHI}} - \phi_{\mu\text{-Ball}}| > 90^{\circ}$ was required in the analysis of Au+Au data.

The correction factors for the remaining contribution of non-target events can be estimated on the basis of data taken without the target (empty frame runs). Our aim is to determine the number of specified particles registered with a detector which originate from reactions within the target, n_t, normalized with respect to the number of these reactions, N_t. This ratio can be written as

$$\frac{n_t}{N_t} \equiv \frac{(n_t + n_e) - n_e}{(N_t + N_e) - N_e}, \tag{10.1}$$

where n_e is the number of the detected particles that originate from non-target reactions. The number of such reactions is denoted by N_e. The measurements with the target only provide the quantities $(n_t + n_e)$ and $(N_t + N_e)$ which can be substituted by the total number of events registered with the reaction trigger. Assuming that the probabilities of reactions inside and outside the target are small and independent, the ratio of interest can be estimated as follows. The probabilities of non-target reactions are expected to be the same in measurements with and without the target, thus approximately

$$\frac{N_e}{N_0} = \frac{N_{e*}}{N_{0*}}, \tag{10.2}$$

where N_0 is the number of incoming beam particles in the measurement with target, and the symbols with an additional star are for the corresponding quantities in the case of empty frame measurement (see Fig. 10.2). The numbers of beam particles were measured with the start detector. From the above relation one gets

$$N_e = \frac{N_0}{N_{0*}} N_{e*} = k N_{e*} \tag{10.3}$$

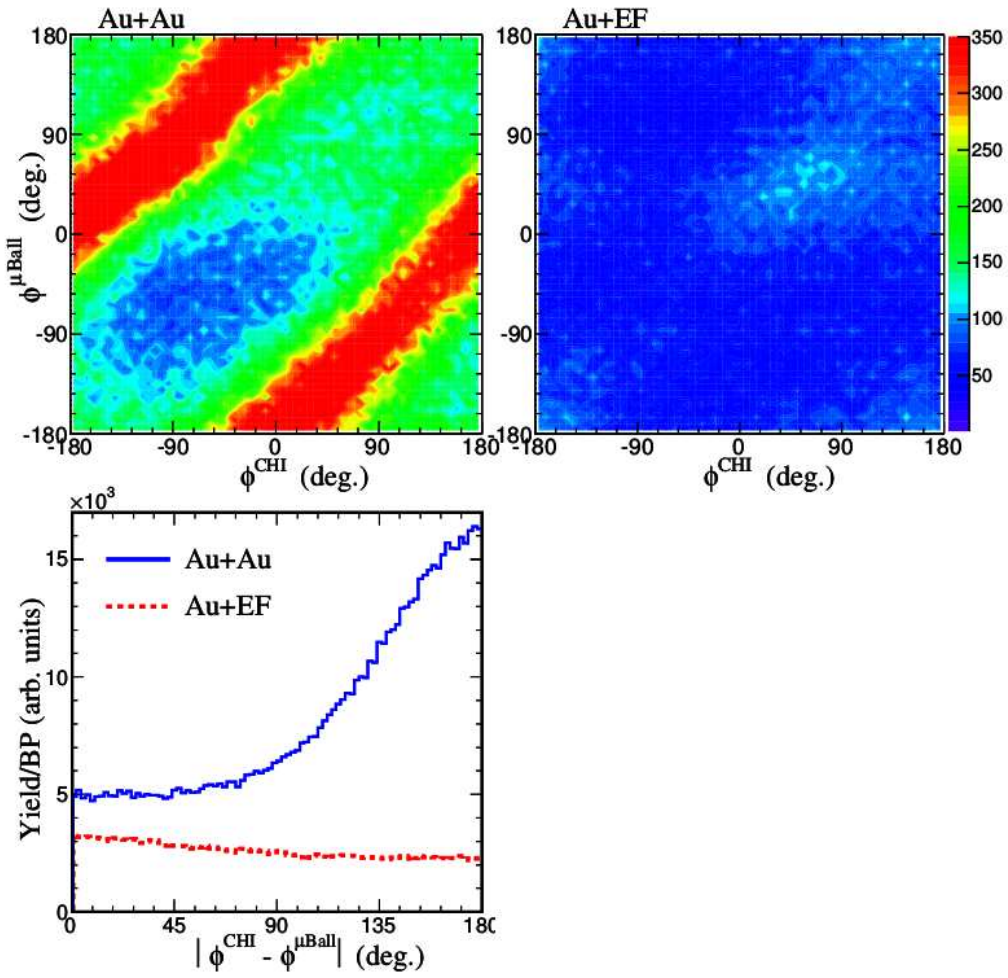

Figure 10.1: Top row: Correlation between the $\vec{Q}$ azimuthal orientations determined with the μ-Ball and with CHIMERA from data taken with (left panel) and without (right panel) the target. Bottom panel: Difference of the $\vec{Q}_{\mathrm{CHI}}$ and $\vec{Q}_{\mu\text{-Ball}}$ orientations, normalized with respect to the integrated beam intensity (BP). Reprinted from [101].

where k is introduced as

$$k \equiv \frac{N_0}{N_{0*}}. \tag{10.4}$$

The characteristics of non-target reactions are the same regardless of the presence of the target. Thus, within the statistical accuracy

$$\frac{n_e}{N_e} = \frac{n_{e*}}{N_{e*}} \tag{10.5}$$

From this, and using Eq. 10.3

$$n_e = N_e \frac{n_{e*}}{N_{e*}} = k n_{e*} \tag{10.6}$$

Finally, the desired ratio can be determined by using the relation

$$\frac{n_t}{N_t} = \frac{(n_t + n_e) - k n_{e*}}{(N_t + N_e) - k N_{e*}}. \tag{10.7}$$

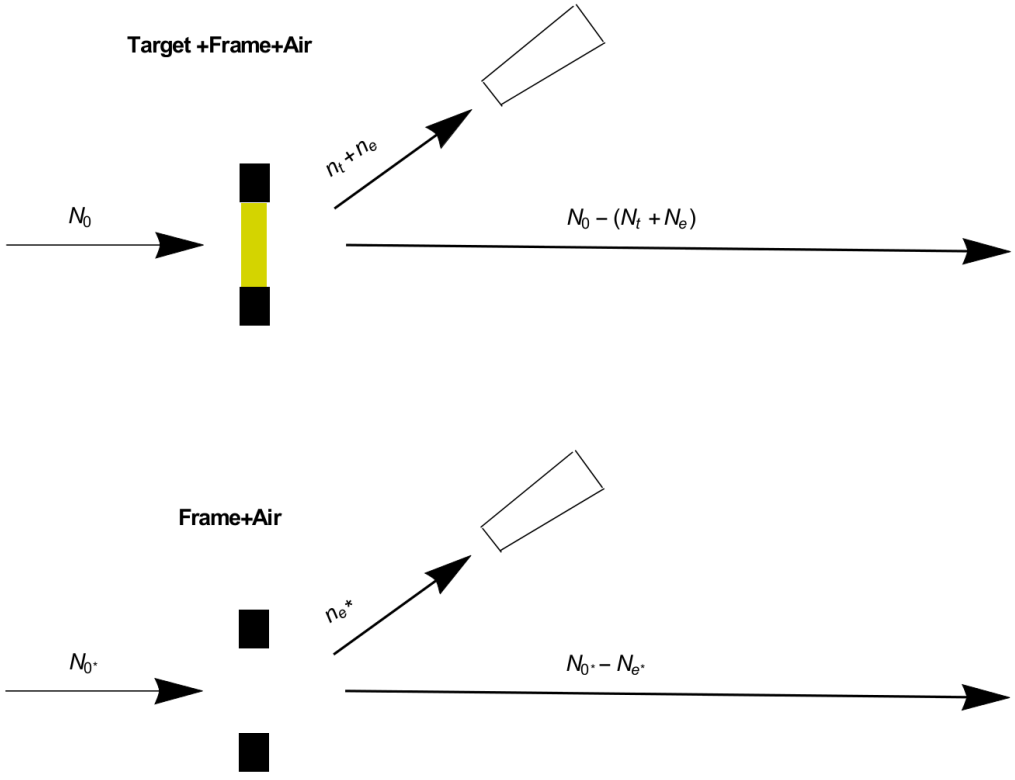

Figure 10.2: Sketch illustrating the symbols used in Eqs. 10.1-10.7.

The methods presented above were used in the KRATTA data analysis to eliminate non-target contributions to the measured spectra of light charged particles.

Chapter 11

Results of KRATTA data analysis

The developed data analysis procedures allowed to obtain precise energy spectra, isotopic ratios and azimuthal angular distributions for light charged particles. Below, some exemplary results are presented for moderately central ($b < 7.5$ fm) ^{197}Au+^{197}Au collisions at 400 MeV/nucleon.

Figure 11.1 shows the energy-per-nucleon spectra of H and He isotopes at two laboratory polar angles 32° and 56°. The different energy ranges for different particles are due to the upper energy detection limits (punch-through energies). With these distributions one can calculate various isotopic yield ratios, in which experimental uncertainties are reduced. Of particular interest is the isobaric ratio t/^{3}He which, as it was shown in theoretical studies [102, 103], is a useful observable to gain information about the density and momentum dependence of the symmetry energy potential. The momentum dependence of the isovector potential leads to a splitting of the effective masses of protons and neutrons that are poorly known at present. The t/^{3}He spectra have also been proposed as a more accurate surrogate for the n/p yield ratios because of difficulties in performing precise neutron measurements [104]. However, the equivalence of the two ratios has not been experimentally demonstrated until now. Figure 11.2 shows the KRATTA result on the ratio of triton to ^{3}He yields as a function of their energy per nucleon. The ratio initially decreases with increasing energy and then stabilizes at the level of about 2.5 for $\theta = 32°$ and about 2 for $\theta = 56°$.

Another important observable is the azimuthal angle distribution with respect to the reaction plane, which allows the determination of flow parameters. Examples of the azimuthal angle distribution of protons measured with the KRATTA detector with respect to the reaction plane estimated from the CHIMERA and ATOF data are shown in Fig. 11.3 for target rapidity, mid-rapidity and projectile rapidity regions. The angular distribution of particles emitted at mid-rapidity shows two maxima at directions perpendicular to the reaction plane characteristic of the squeeze-out effect (negative elliptic flow). In the projectile and target rapidity regions the particle emissions exhibit in-plane patterns i.e. the dominance of directed flow. The directed and elliptic flow parameters v_1 and v_2 were determined by fitting

$$\frac{dN}{d\left(\phi - \phi_R\right)} = \frac{N_0}{2\pi}\left(1 + 2v_1 \cos\left(\phi - \phi_R\right) + 2v_2 \cos 2\left(\phi - \phi_R\right)\right) \tag{11.1}$$

to the experimental azimuthal angle distribution. The results of fitting are shown in Fig. 11.3 by the red lines.

The resolution of the reconstructed reaction plane has an important impact on the flow determination [105]. Hence, a proper correction procedure has to be applied to the flow parameters. The resolution of the reconstructed reaction plane was calculated using the sub-event

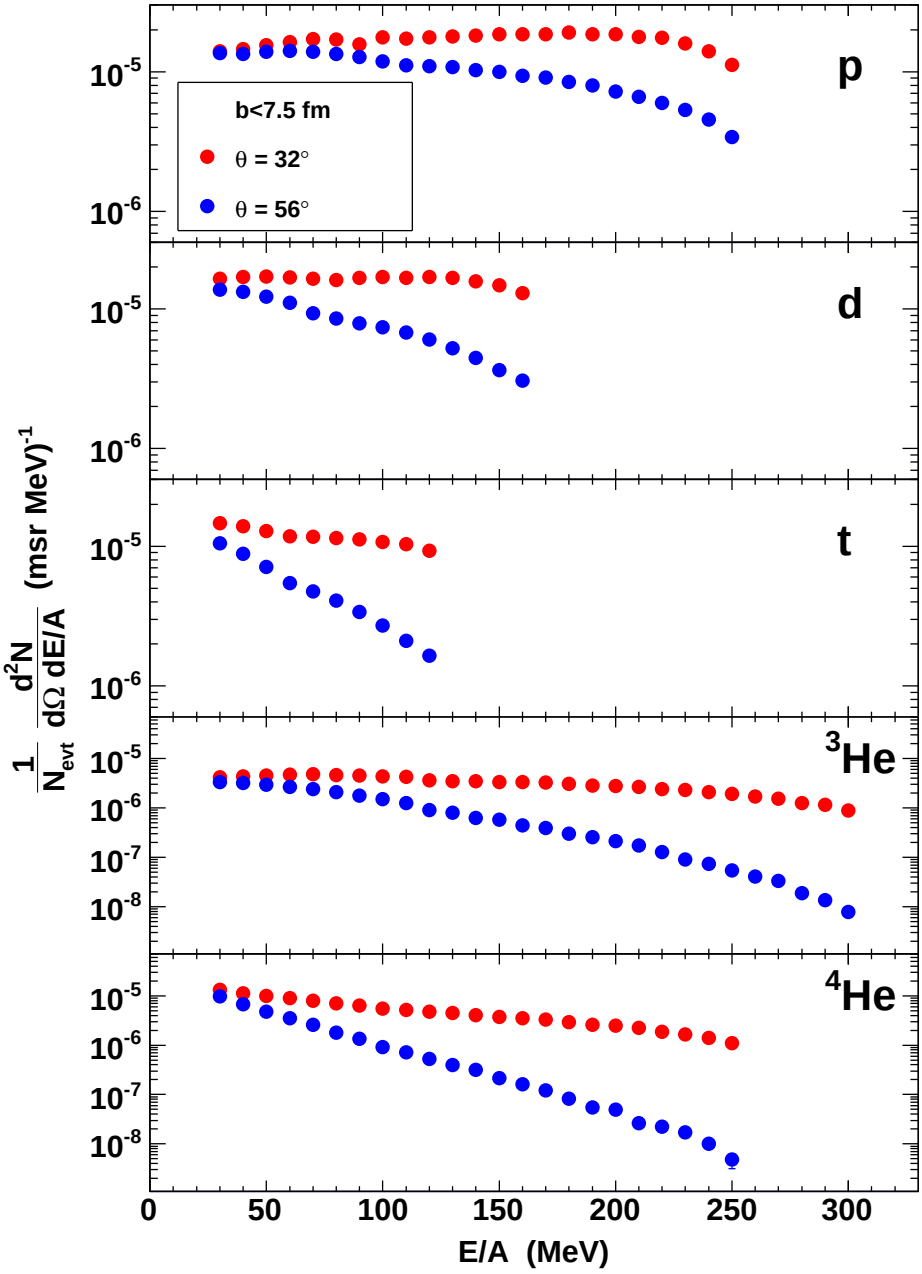

Figure 11.1: Experimental results obtained with KRATTA for the ^{197}Au+^{197}Au system at 400 MeV/nucleon: Energy spectra of light charged particles for impact parameters $b < 7.5$ fm at two polar angles. The yields are normalized to the number of triggered events (reaction trigger) and to the solid angle. Statistical errors are smaller than the symbols.

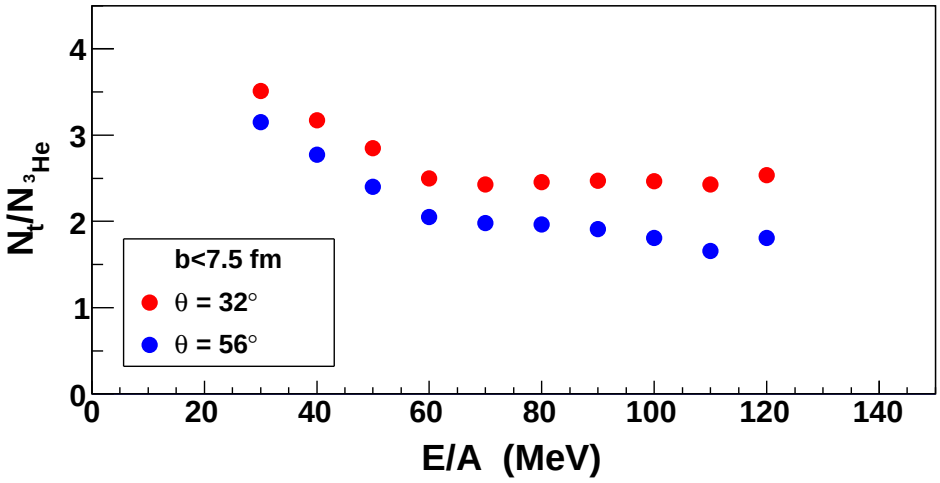

Figure 11.2: Ratio of the t/^{3}He yields as a function of their kinetic energy per nucleon.

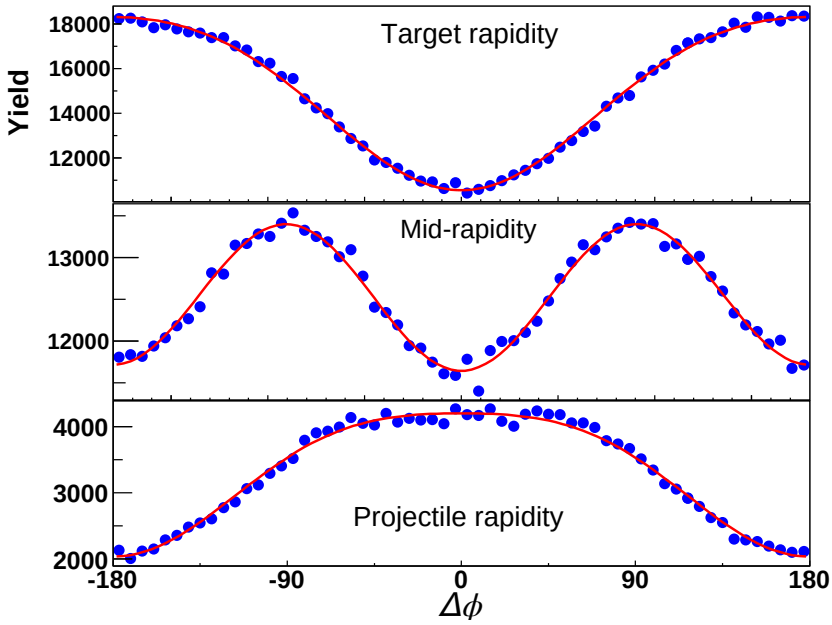

Figure 11.3: Azimuthal angle distribution measured with respect to the reaction plane for protons in three different rapidity regions. The red lines show the result of fitting Eq. 11.1 to the data.

mixing technique of Ref. [105]. This method is based on a random division of the event into two so called sub-events and then extracting the reaction plane orientation for each of them separately. Then the azimuthal angle, $\Delta\phi_{RP}$, between these two sub-events was calculated. The distribution of $\Delta\phi_{RP}$ is shown in Fig. 11.4. The figure also shows a fitted function (red) according to the Eq. (12) of Ref. [105]. The resolution parameter χ has been extracted from the fit of the theoretical function to the experimental distribution. It allowed to determine the dispersion corrections, $\langle\cos(\Delta\phi)\rangle$ and $\langle\cos(2\Delta\phi)\rangle$, for the v_1 and v_2 parameters, respectively. In our case, the resolution parameter and the corrections are:

$$\begin{aligned} \chi &= 1.14, \\ \langle\cos(\Delta\phi)\rangle &= 0.76, \\ \langle\cos(2\Delta\phi)\rangle &= 0.44. \end{aligned}$$

Since the real values of v_1 and v_2 are estimated by dividing the measured ones by the corrections, the actual values will increase by about 30% in case of v_1 and by more than a factor of 2 in case of v_2. It is worth mentioning that the procedure used here has an improved version reported in [47]. The first method was chosen in order to be consistent with the FOPI analysis [106] for the purpose of comparing the flow results obtained for the same reaction in different experiments with different detectors.

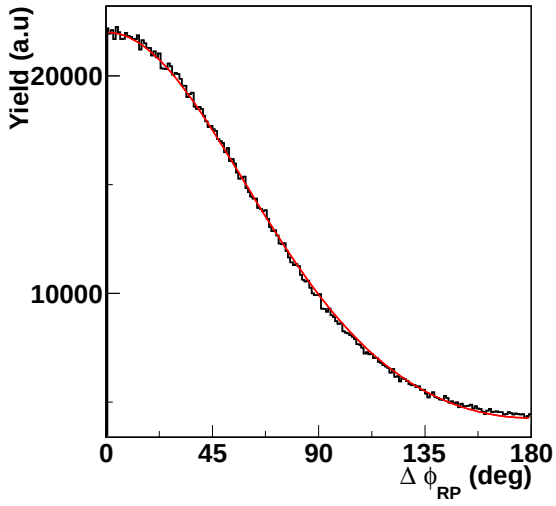

Figure 11.4: Distribution of the relative angle, $\Delta\phi_{RP}$, between the reaction planes in sub-events.

For the desired comparison with the FOPI results, in order to ensure the same angular acceptances, the KRATTA polar angle acceptance was reduced in the analysis to the range $38.5° < \theta < 56.5°$. Figure 11.5 shows the KRATTA kinematic acceptance (for protons) with two angular limits (lines) which correspond to the acceptance cuts imposed in the analysis of the FOPI data. Figure 11.6 presents the flow parameters v_1 and v_2 for light charged particles as a function of the scaled center of mass rapidity for mid-central collisions, obtained with the KRATTA detector (circles) and from the FOPI measurement (stars) [107]. Due to the restriction of the polar angle range and the KRATTA upper energy detection limits, the range of the available rapidities was smaller than in case of the FOPI data. The comparison shows a

very good agreement between the two measurements, confirming the reliability of the obtained results. It supports the soft nature of the symmetric-matter NEOS that was deduced from the FOPI data set.

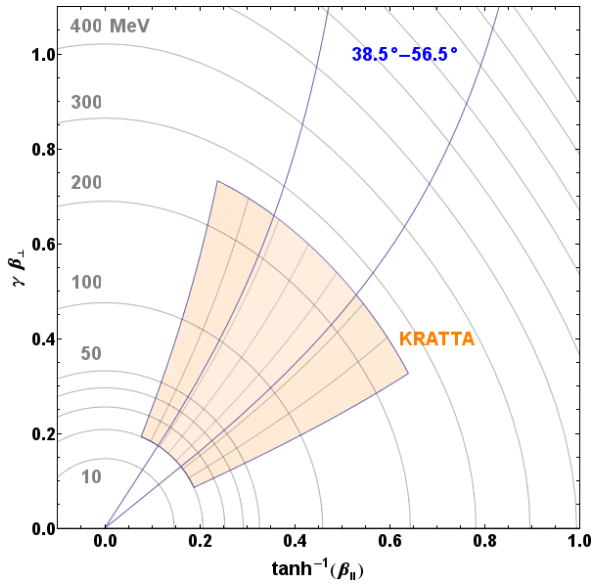

Figure 11.5: Kinematic acceptance and angular limits used for the KRATTA-FOPI flow comparison.

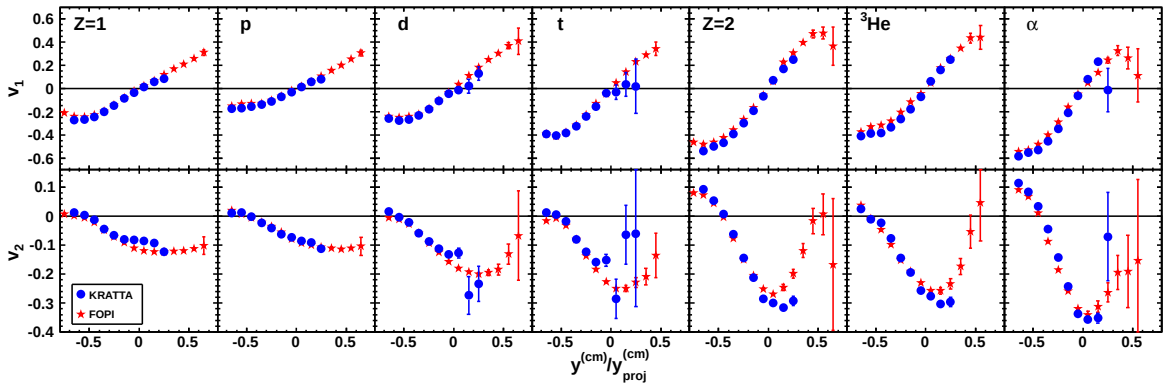

Figure 11.6: Directed and elliptic flow parameters determined from the KRATTA data and from the FOPI data for the Au+Au reaction at 400 MeV/nucleon.

Chapter 12

Comparisons with UrQMD model predictions

The provided precise KRATTA experimental data will be useful for validation of current theoretical transport models which are required for the interpretation of the symmetry energy observables. We have performed initial comparisons between the KRATTA results and the results of simulations with the UrQMD model.

The Ultra-relativistic Quantum Molecular Dynamics model (UrQMD) was developed to provide a description of various aspects of nuclear reactions at high energies [49, 108, 109]. It has been adapted to intermediate energy heavy-ion collisions by incorporating a nuclear mean field, the Yukawa and Coulomb interactions, and a Pauli-blocking procedure [110, 111]. In order to study the symmetry energy effects, the density-dependent symmetry energy was introduced in the form of a two component power-law function:

$$\begin{aligned} E_{sym} &= E_{sym}^{kin} + E_{sym}^{pot} = \\ &= 12MeV \cdot (\rho/\rho_0)^{2/3} + 22MeV \cdot (\rho/\rho_0)^{\gamma} . \end{aligned} \tag{12.1}$$

The first term with an exponent of 2/3 is the kinetic contribution to the symmetry energy and it results from the two component Fermi-gas model. It is responsible for only about $^1/_3$ of the total volume symmetry energy E_{sym} which amounts to approximately 32 MeV for nuclear matter at the saturation density. The major contribution is given by the potential term reflecting the properties of the nuclear forces. The potential part of the symmetry energy was parametrized in analogy to the kinetic term by applying the γ parameter as an exponent of the reduced density. It should be stressed that this parametrization leads to momentum independent potential. Nevertheless, it has been shown that the momentum dependence or independence of the isovector potential has a weak influence on the elliptic flow [112].

The present simulations were performed for $\gamma = 0.5$ and $\gamma = 1.5$ corresponding to a soft and a stiff density dependence of the symmetry energy. In each simulated event, the UrQMD calculations were stopped at a collision time of 150 fm/c, at which a clustering algorithm was applied to the phase space distribution of nucleons. The clusters were identified by examining the proximity of nucleons in phase space with two parameters, Δr and Δp, for the relative nucleon coordinates and momenta, respectively. The proximity limits $\Delta r = 2.5$ fm and $\Delta p = 290$ MeV/c, that are typical of QMD models, were chosen as standard parameters. In order to evaluate the significance of the parameter values for different observables, the simulations were also performed for $\Delta r = 3$ fm and $\Delta p = 100$ MeV/c, which lead to a "weaker" clusterization.

The analysis was carried out for semi-central collisions of ^{197}Au+^{197}Au at 400 MeV/nucleon, for the impact parameter window $5.5 < b < 7.5$ fm. The simulation results were filtered by the detector acceptance:

- polar angle in the laboratory system $24^\circ < \theta_{LAB} < 62^\circ$,
- kinetic energy:

  $20 < E_{kin}/A < 250$ MeV for protons,

  $20 < E_{kin}/A < 160$ MeV for deuterons,

  $20 < E_{kin}/A < 133$ MeV for tritons.

For observables which involve various particles, the maximum common energy (per nucleon) range was used.

In the following figures showing comparisons between the KRATTA data and the simulation results, the former will be represented by points, and the latter by lines:

- asy-soft with $\gamma = 0.5$ - blue lines,
- asy-stiff with $\gamma = 1.5$ - red lines,
- standard clusterization - solid lines,
- weaker clusterization - dashed lines.

The statistical errors will be shown when they exceed the symbol size.

Figure 12.1 compares the charge distribution. The model with the standard clusterization procedure well reproduces the mean multiplicity of $Z = 1$ particles, however, discrepancies by a factor of 2 to 4 are observed for heavier particles. It is seen that the predicted multiplicities are insensitive to the specific choice of γ. A significant sensitivity to the symmetry term stiffness is predicted for the t/^{3}He yield ratio, which is shown in Figs. 12.2 and 12.3. It confirms that this is a valuable observable in probing the symmetry energy. However, the experimental ratios are largely underestimated, especially for smaller rapidities and transverse momenta, which indicates that significant improvements for the model and/or the clusterization procedure are required. One of the possible reasons of this disagreement may be the momentum dependence of the isovector potential, which was not taken into account in this model [113, 114].

The experimental and UrQMD results on the directed and elliptic flow of protons and deuterons are shown in Fig. 12.4. The measured directed flow is very well described by the model with the standard clustering procedure. Some discrepancies are observed for the elliptic flow, particularly in the case of protons. Nevertheless the trends are rather well reproduced. The predicted flow parameters for charged particles show no significant sensitivity to the symmetry energy stiffness.

The uncertainties associated with the clusterization procedure can be eliminated within a coalescence-invariant approach, by examining flow of all (both free and bound in clusters) protons or all neutrons [23, 104]. In such an analysis, the yields of protons and neutrons in a given kinematic bin, are calculated as

$$\begin{aligned} N_p^{Tot} &= N_p + N_d + N_t + 2N_{^3He} + 2N_\alpha + \cdots , \\ N_n^{Tot} &= N_n + N_d + 2N_t + N_{^3He} + 2N_\alpha + \cdots . \end{aligned}$$

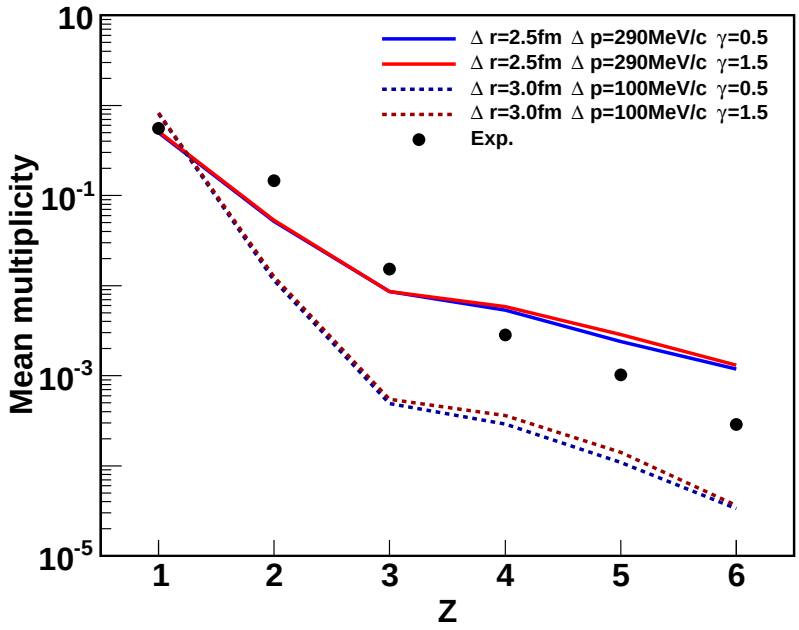

Figure 12.1: Comparison of the KRATTA data with the UrQMD model predictions: the average multiplicity of charged particles per event as a function of the atomic number.

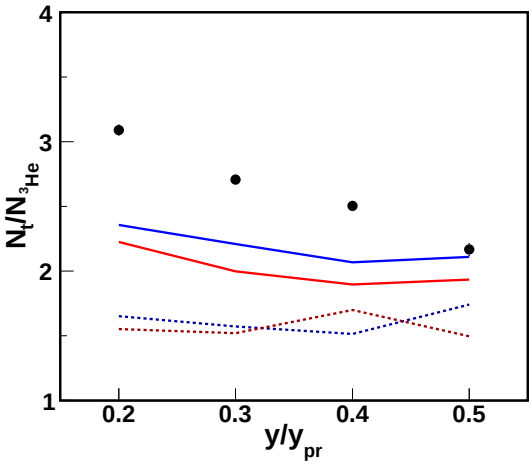

Figure 12.2: The t/^{3}He ratio as a function of normalized rapidity.

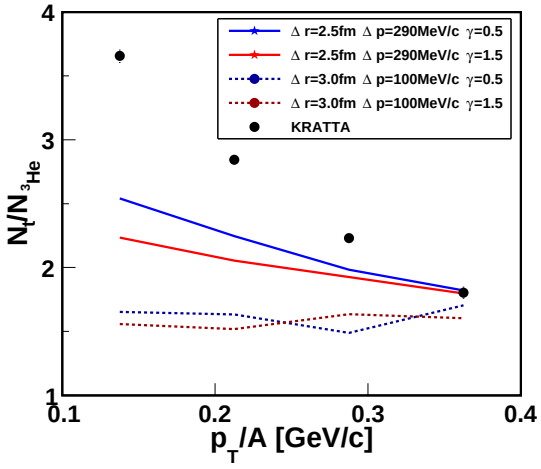

Figure 12.3: The t/^{3}He ratio as a function of transverse momentum per nucleon.

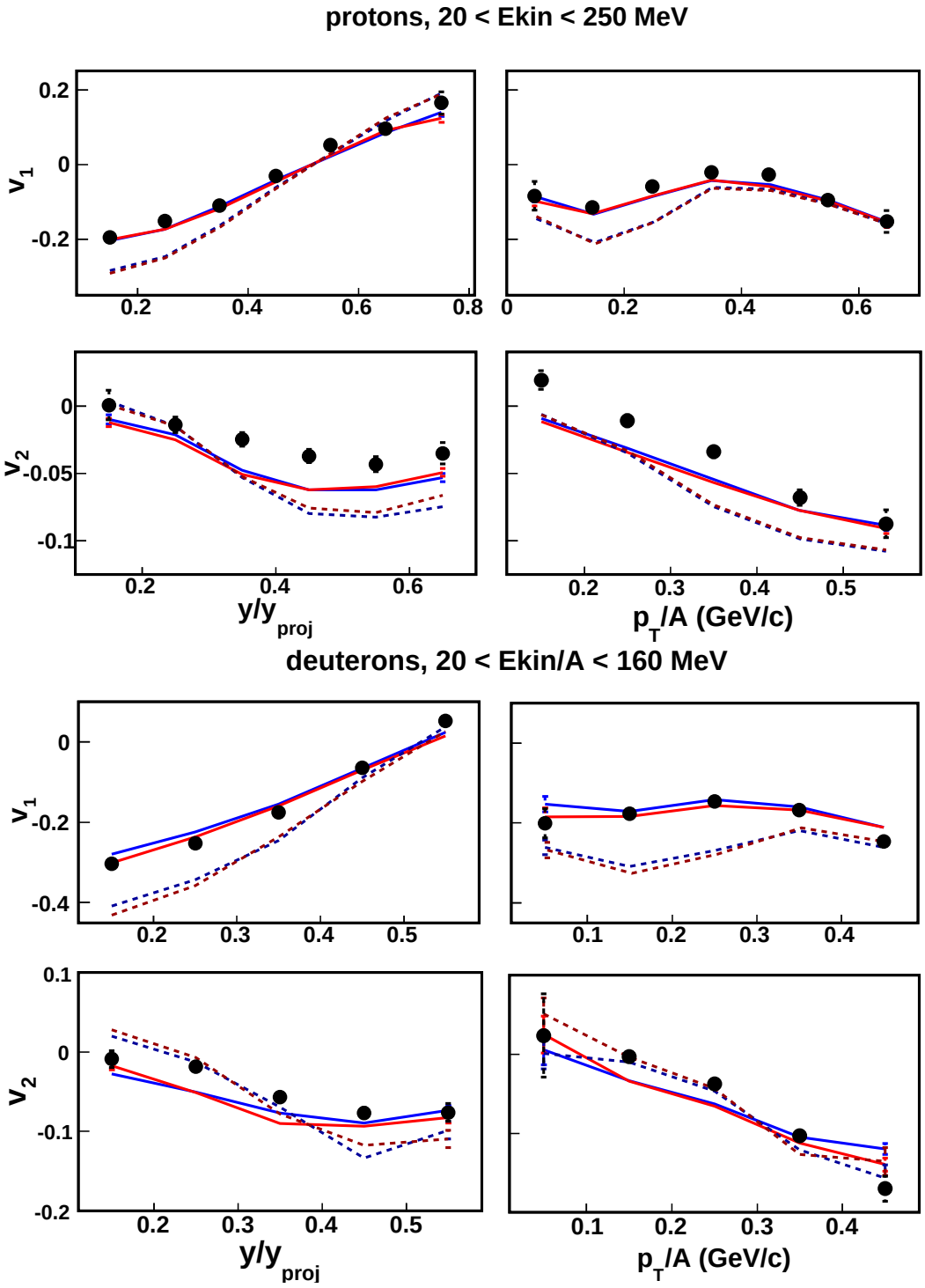

Figure 12.4: Directed v_1 and elliptic v_2 flow of protons and deuterons as a function of rapidity (left panels) and transverse momentum per nucleon (right panels).

The top panels of Fig. 12.5 show the elliptic flow of all protons plotted as a function of rapidity and transverse momentum. The results of simulations are nearly the same for the soft and stiff options. They qualitatively follow the experimental data, however the predicted elliptic flow from squeeze-out is weaker than that observed. The bottom panels in the figure present the predicted elliptic flow for all neutrons, which shows significant sensitivity to the symmetry energy. In this case the experimental data are not available yet, since the analysis requires the inclusion of the data from LAND.

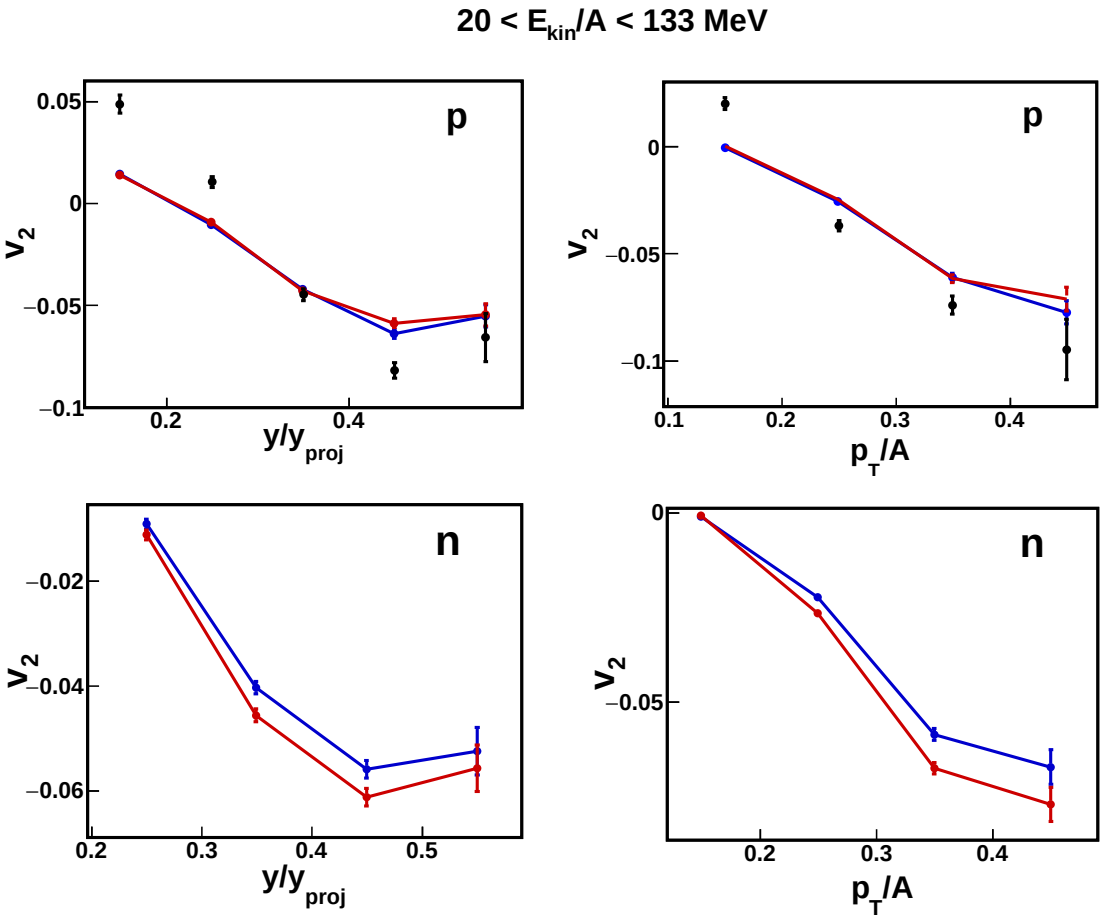

Figure 12.5: Elliptic flow of all (both free and bound) protons (top panels) and all neutrons (bottom panels) as a function of rapidity (left panels) and transverse momentum (right panels). The KRATTA data for protons are shown as points, the red and blue lines represent the stiff and soft assumptions in UrQMD calculations.

Investigations of the symmetry energy at high densities rely mainly on measurements of the neutron elliptic flow. However, additional information on the flow of charged particles will allow to examine the elliptic flow ratios that are more reliable due to canceling systematic errors associated with the corrections for the reaction plane dispersion, as well as to perform the coalescence-invariant analysis.

Chapter 13

Symmetry energy constraint based on LAND data

The main goal of the ASY-EOS experiment was to provide a new constraints for the symmetry energy at supra saturation densities. It required the use of LAND, a detector capable of measuring neutrons and charged particles produced in the reactions. Due to some technical problems, the desired elemental and isotopic identification of light charged particles detected with LAND was not possible. Thus, the further analysis was limited to neutrons and to all charged particles only. For both of the groups the directed and elliptic flows were determined. The reaction plane orientation and the impact parameter were estimated with the use of the procedures described in previous chapters. The details of the analysis procedure are given in [115].

Figure 13.1 presents the elliptic flow ratio of neutrons and charged particles as a function of the transverse momentum per nucleon, p_t/A. The experimental results are compared with the UrQMD predictions for soft (γ=0.5) and stiff (γ=1.5) symmetry energy potentials. The model calculations were adapted to the experimental conditions. From linearly interpolating between the two predictions, the best description of the data was obtained with the power-law coefficient $\gamma = 0.75 \pm 0.10$ where the error is the statistical uncertainty from the fit [101]. After incorporating the estimated systematic uncertainty, the total error is $\Delta\gamma \simeq 0.2$. It confirms the moderately soft to linear density dependence of the symmetry energy deduced previously from the FOPI-LAND data [48].

Figure 13.2 shows the new ASY-EOS constraint for the density dependence of the symmetry energy as a function of the reduced density ρ/ρ_0 in comparison with the earlier FOPI-LAND result [48]. This new result confirms the former but has a significantly smaller uncertainty. For reference, the figure includes low-density results of Refs. [116–119] which were obtained from investigations of the ground state properties of doubly magic nuclei (Brown), the neutron skin thicknesses (Zhang), the isospin diffusion (HIC Sn+Sn) and the excitation energies to isobaric analog states (IAS). Additionally, the figure shows the high-density result of Xiao et al. [31] obtained from analysis of the FOPI pion data which is in strong disagreement with the ASY-EOS and FOPI-LAND results.

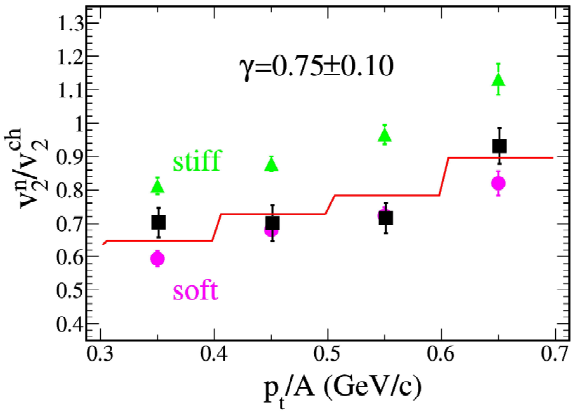

Figure 13.1: Elliptic flow ratio of neutrons and charged particles for moderately central ($b < 7.5$ fm) collisions of ^{197}Au+^{197}Au at 400 MeV/nucleon as a function of the transverse momentum per nucleon. The full squares represent the ASY-EOS experimental data, the triangles and dots represent the UrQMD predictions for stiff ($\gamma = 1.5$) and soft ($\gamma = 0.5$) power-law exponents of the symmetry-energy potential term. The full line is the result of a linear interpolation between the predictions, leading to the indicated $\gamma = 0.75 \pm 0.10$. Reprinted from [101].

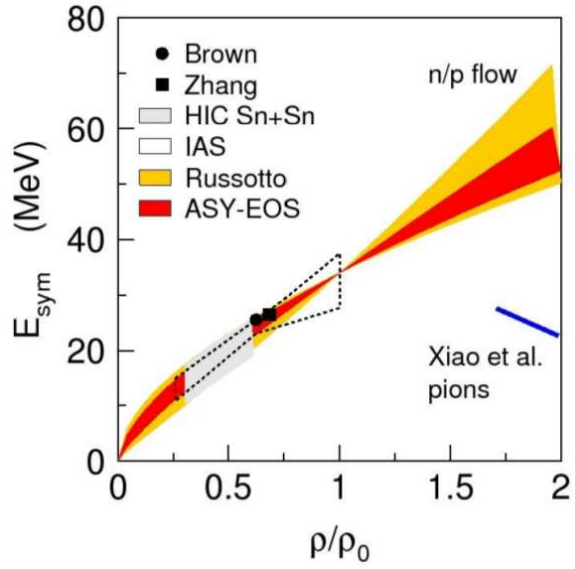

Figure 13.2: Constraints on the symmetry energy obtained from the ASY-EOS experiment in comparison with the FOPI-LAND result. For reference some low-density results are included (see text). Reprinted from [101].

Chapter 14

Summary and perspectives

The main aim of this dissertation was the development of digital pulse shape analysis methods, including neural networks, for particle identification and background suppression, which are necessary in the analysis of experimental data provided by the KRATTA multi-detector system. The KRATTA detector was used in the ASY-EOS experiment dedicated to the study of the symmetry energy term in the nuclear equation of state (NEOS) at supra-saturation densities, and conducted at the Heavy-Ion-Synchrotron SIS18 at the GSI laboratory in 2011. The collective flows of neutrons and light charged particles, measured with the Large Area Neutron Detector (LAND), are known to be sensitive probes of the symmetry energy. The reaction systems ^{197}Au+^{197}Au, ^{96}Ru+^{96}Ru, and ^{96}Zr+^{96}Zr, all at incident energy 400 MeV/nucleon, were chosen for this investigation. The KRATTA detector was included in the setup for providing information on charged particle yields and flows with higher precision than available with LAND.

The KRATTA (KRAków Triple Telescope Array) is a versatile broad energy range detection system for light charged particles. It consists of triple telescope modules with Si and CsI(Tl) elements. The silicon photodiodes serve as ΔE silicon detectors and simultaneously as detectors of the scintillation light produced by CsI(Tl) crystals. This novel detection technique requires decomposition of the photodiode signals into a direct ionization, and fast and slow scintillation components. It was successfully achieved by signal modeling and parametric fitting to the measured waveforms. The obtained parameters representing the actual amplitudes of the signal components allowed to construct various isotope identification maps, useful also for the reduction of punch-through and background events.

The KRATTA data contain a substantial background contribution, arising mainly from secondary reactions generated in the detector material by energetic particles. The fraction of background events exceeds even 50% in some parts of the isotope distributions. Thus, the recognition and rejection of background events was of special importance and one of the main objectives of the present research. For this purpose, a pulse shape analysis method based on an artificial neural network, namely a Kohonen self-organizing map, has been proposed and investigated. Performed tests have shown that this approach provides satisfactory results, reducing the background by a factor of about 2 for H isotopes and by a factor of 3-6 for He isotopes. In addition, punch-through events can be removed together with background events. The advantage of using the self-organizing map is that this network is trained in an unsupervised manner directly from unlabeled data, and thus no additional calibration procedures are needed. It has been shown that this method can be applied for raw data processing, which opens the perspective of eliminating the time consuming fitting procedure, reducing the pro-

cessing time by at least an order of magnitude. Moreover, this method provides the possibility of using a fast on-line preprocessing to extract few relevant waveform parameters, instead of acquiring the whole waveforms. It would greatly reduce the amount of data transferred to the acquisition system and the storage volume in future KRATTA measurements.

The events associated with the secondary nuclear reactions in the detector material are observed in the identification maps as background events, which leads to significant losses in the isotopic yields. The necessary corrections for those event losses were determined from Monte Carlo simulations performed with Geant4.

Other data analysis procedures that were employed for the energy calibration, corrections for the remaining background, recognition and rejection of non-target events, estimations of the impact parameter and the reaction plane orientation, have also been presented in this thesis.

With those procedures, precise energy spectra, isotopic ratios and azimuthal angular distributions were produced for charged reaction products with atomic number up to $Z = 4$. These results were obtained for the ^{197}Au+^{197}Au reaction whose analysis has been completed. The directed and elliptic flows of light particles deduced from the data were found to agree to high precision with previously obtained results of the FOPI collaboration. It supports the soft nature of the symmetric-matter NEOS that was deduced from the FOPI data set.

These KRATTA results are expected to aid in the development and test of transport theories required for the interpretation of the symmetry energy observables, and in particular for resolving existing ambiguities regarding the role of the nuclear effective mass and momentum dependent forces in the reaction process. Initial comparisons between the experimental results and the results of calculations performed with the UrQMD model showed a significant disagreement in the isobaric t/^{3}He yield ratio, indicating the need of improvements for the model and particularly for the clusterization procedure.

The analysis of the LAND data for the ^{197}Au+^{197}Au system allowed to determine the elliptic flow ratio of neutrons versus charged particles. Based on the comparison with UrQMD predictions, a new constraint for the symmetry energy at supra-saturation densities was obtained. The power-law coefficient of the symmetry energy potential was estimated to be about 0.75. This new result confirms the moderately soft to linear density dependence of the symmetry energy deduced previously from the FOPI-LAND data.

Further analysis of the ^{96}Ru+^{96}Ru and ^{96}Zr+^{96}Zr data is expected to provide interesting new results enabling better insight into the isospin effects. It will allow to compare neutron-rich and neutron-deficient systems of the same mass and construct double ratios, such as the double neutron-proton differential elliptic flow. The gained knowledge and experience from the ASY-EOS experiment will be a base for future investigations of the symmetry energy planned at the FAIR facility.

The author of this thesis contributed to the KRATTA detector construction, to performing the ASY-EOS experiment, to the analysis of the KRATTA data as well as to the software development for on-line detector monitoring and cross-detector data analysis.

Appendix: Asyeosroot

The experimental data analysis was performed using the FairRoot framework [98]. The developed project was named *Asyeosroot*. In this section the Asyeosroot project will be described with a brief overview of some of the used FairRoot framework features.

FairRoot

The FairRoot is a simulation and analysis framework for the experiments at the upcoming accelerator centre FAIR. This framework in its first concept was designed to be a base for three experiments at GSI/FAIR: CBM, R^3B and the ASY-EOS.

The growing popularity of the FairRoot made the system become an independent software (of those experiments) and now (2016) it can be freely used under the GNU Lesser General Public License (LGPL) version 3 [120]. The FairRoot can operate on a standard desktop computer which meets suggested requirements. All the installation details are available on the FairRoot home page [98].

The FairRoot is provided in two packages. The first is the FairSoft and it is a set of scripts which download and install all the necessary tools for the FairRoot such as: compilers, libraries, Monte Carlo engines etc. The second part consists of the main FairRoot framework which is ready for the development. Empty FairRoot framework allows to build and develop the whole experimental data analysis chain and perform Monte Carlo simulations.

The FairRoot itself is based on the ROOT class library [94]. One of the main ideas which stand behind the FairRoot framework development was to unify interfaces of various and alternative tools commonly used in the experimental physics. FairRoot integrates the way of using some of them. The role which the FairRoot plays e.g. for the CBM, Panda and R^3B experiments is shown in Fig. 14.1. From the user point of view the FairRoot is an abstract layer which serves mechanisms for an easy construction of experimental analysis chain and performing simulations.

Nowadays, in all large experimental projects, an efficient, flexible and fast method of software developing is very important. The continuously growing amount of data produced in the modern nuclear/high energy physics (HEP) experiments creates high requirements for the hardware as well as for the software. FairRoot is a base which adapts some of the software tools to make the software developing for particular experiments easier and in a more controlled way and thus it satisfies some of the software requirements.

One of the most important FairRoot's features is its architecture. It is flexible and can be easily extended for required functionalities. FairRoot allows to make the experimental data analysis and perform Monte Carlo simulations with using once defined sort of objects (such

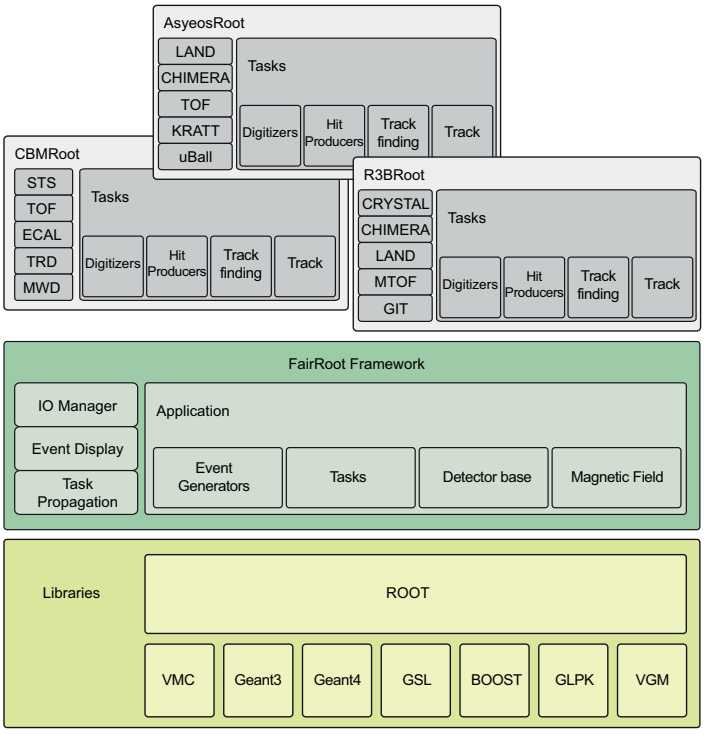

Figure 14.1: FairRoot framework design chart. Reprinted after adaptation from [98].

as plots) and moreover, even whole parts of the analysis chain. FairRoot allows to use the same sort of data containers to present the experimental and simulated data analysis results. The input data source can be changed while the analysis procedures can be reused again. This idea is presented schematically in Fig. 14.2, where an exemplary data analysis flow is presented.

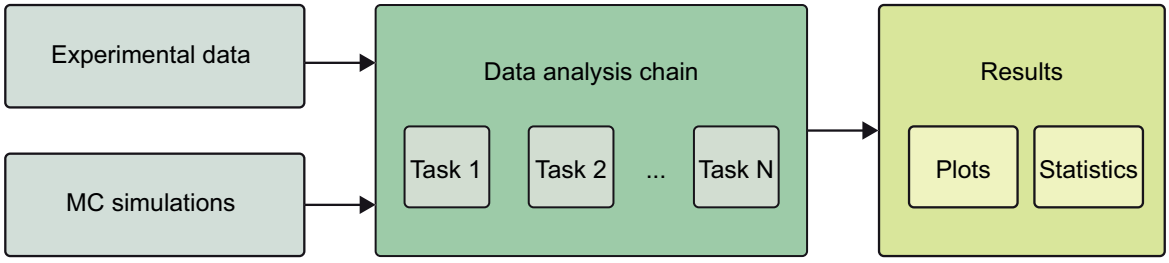

Figure 14.2: The concept of the FairRoot data flow chain.

Another FairRoot's feature is that it provides an interface for using various Monte Carlo engines (Fluka, Geant3, Genat4). It allows the user to save time when switching between them. For a given study case the simulation results can be easily compared. Another FairRoot feature is allowing computing parallelization (PROOF is supported).

FairRoot offers various particle generators to perform simulations. For example, simula-

tions can be realized with a single particle (of a given type and momentum) emission from a given point (source). This scenario is realized with so-called *Box* generator. Simulated events can also be read from the ASCII file. It should be emphasized that the ASCII data structure needs to meet the ASCII reader requirements. Other generators are also available.

An important FairRoot's advantage is providing a track viewer which allows to visualize the results of the simulated event - particles produced in the event with their tracks. In this way, the simulations' results can be controlled and studied more deeply and thus they can be understood better.

The data analysis chain is designed as a queue. As usual in HEP, each kind of the experimental data analysis can be split into a set of processes which are performed in a given order. One separate part of analysis in the FairRoot is called "Task" (`TTask` class). Tasks can be easily managed by the user. They can be added to the analysis chain or removed when they are currently unnecessary.

In addition, some of them can be encapsulated which means that a set of subtasks can be grouped in one super-task. Analysis scenarios are defined in short and legible root macros. The flexibility of analysis performing is another advantage of the FairRoot.

Asyeosroot takes benefits from the FairRoot since it is built on this framework.

KRATTA analysis chain in the Asyeosroot

The Asyeosroot project started after conducting the S394 experiment. Asyeosroot is a name for the project of the software development for the purpose of the ASY-EOS experimental data analysis. It is worth noticing that the ASY-EOS experiment was the first which used the FairRoot for the real experimental data analysis.

All the data collected during the S394 experiment were saved in the `lmd` files. The standard file size is around 1GB. In total, there are 2115 `lmd` files. Many of them contain data from the test runs or calibration. The data of the studied systems are stored in a given number of files:

- Au+Au campaign: 495 files
- Zr+Zr campaign: 200 files
- Ru+Ru campaign: 124 files

All the data are available in the GSI data storage system.

The Asyeosroot construction is organized according to the the FairRoot concept.

The Asyeosroot project is supported with the SVN control version system and can be freely reviewed [121]. Below the KRATTA data flow is described and it is schematically presented in Fig. 14.3.

The Asyeosroot analysis chain starts with a task which reads the data from the `lmd` files and which uses two detector identification numbers. This task locates data buffer which is next served for the unpacking classes dedicated for each detector. In case of KRATTA detector this role is played by `KRATUnpack`. Later, various tasks can be included in the analysis chain. For the purpose of the standard analysis, a set of main tasks was designed and implemented. They are presented in Fig. 14.3.

Below there is a short description of the most important tasks dedicated to the KRATTA data analysis:

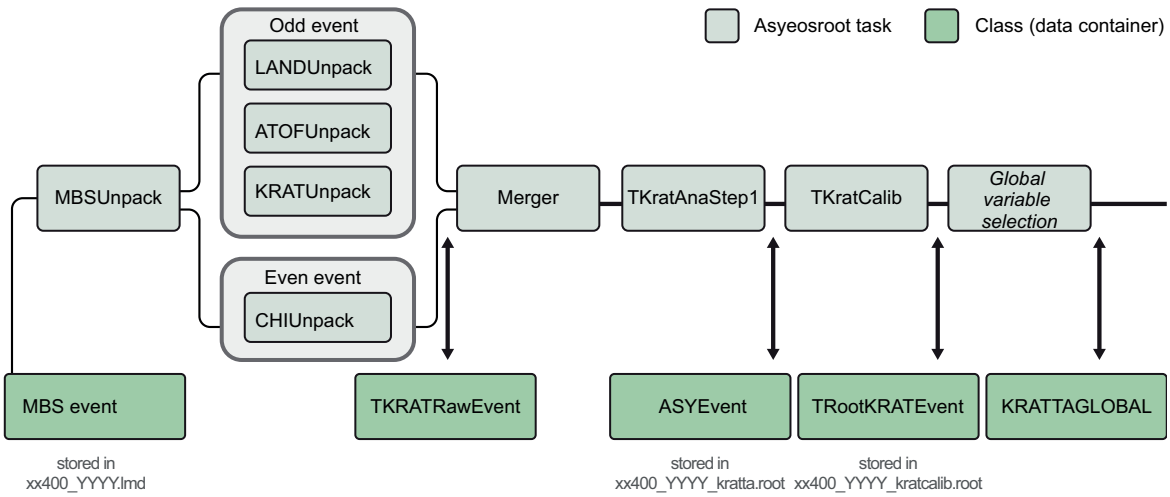

Figure 14.3: Data flow chart for the KRATTA data implemented in the Asyeosroot.

- `KRATUnpack` - reads raw data from the buffer and decodes them using the implemented decoding algorithm. The decoded data are saved in the class container `TKRATRawEvent`.
- `TKratAnaStep1` - in this task the first step of decoded data analysis is implemented. The raw pulse shapes are read from the `TKRATRawEvent` class, then the following procedures are called: pulse probing, moment calculations, decomposition. The results are saved in another class container `ASYEvent`.
- `TKratCalib` - in this class the identification and energy calibration procedures are implemented. For this purpose external tables and data files are used. Information on identified particles is stored in the class container `KrattaParticle`. In contrast to other tasks, this task's inner structure is more complex e.g. it uses separately developed classes `Swiatowid`, `Target`, `KrattaEne`. The first is used for the particle identification and the last two for calibration.
- `TKratDstReader` - this task allows to read already preprocessed data with the task `TKratAnaStep1` which are stored in standalone `root` files. This can be the first step of the analysis, which makes it possible to avoid the raw data reading and time expensive pulse shape decomposition.
- `TKratMerger` - this task provides a mechanism for merging KRATTA preprocessed data (stored in the class `ASYEvent`) which are read from `root` files with the rest ASY-EOS data analysis flow. The merging procedure is based on matching the run number and the event number obtained from the `lmd` files and given for each event in the `ASYEvent` data container.

Tasks for the Monte Carlo simulations data analysis:

- `TKratSimKapReader` - this task was designed for the analysis of the simulated data. Data are taken from the `root` files and are stored in container class `TKratSimKapReaderDataContainer`.

- `TKratSimKapAna1` and `TKratSimKapAna2` - are tasks used for determining the reaction probability.
- `TKratTreat` - in this task an algorithm for the energy to light (which can be produced in the CsI scintillator crystals) conversion is implemented. It can be used for the data analysis of the results obtained from Monte Carlo simulations.

There was also a need of developing a number of other tasks, not described here, which support the analysis.

Acknowledgements

I would like to acknowledge support by the Foundation for Polish Science - MPD program, co-financed by the European Union within the European Regional Development Fund and Prof. Paweł Moskal, the project coordinator. Part of the numerical calculations were performed on the computing cluster of the GSI, Darmstadt, Germany. I would like to thank professor Janusz Brzychczyk and Jerzy Łukasik for a fruitful collaboration over the course of my PhD studies. Special thanks are addressed to Wolfgang Trautmann and Paolo Russotto for thier continous help and assistance which cannot be overestimated. I would also like to thank collaboration co-workers: Piotr Pawłowski, Arnaud Le Fevre, Yvonne Leifels, Simon Gannon, Mladen Kiš, Angelo Pagano and all the other ASY-EOS collaboration members. I'd like to take this opportunity to thank my academic colleagues, especially Piotr and Paweł, Krzysztof, Yasir. Finally, I would like to thank my loving family to which I'm dedicating this work.

List of Figures

List of Tables

References

[1] A. B. Brown, Phys. Rev. Lett. **85**, 5296 (2000). 1

[2] B.-A. Li, L.-W. Chen, and C. M. Ko, Phys. Rep. **464**, 113 (2008). 1, 6, 95

[3] M. B. Tsang *et al.*, Phys. Rev. C **86**, 015803 (2012). 1, 7, 8, 95

[4] J. Piekarewicz, arXiv:1307.7746[nucl-th] (2013). 1, 7

[5] X. Liu *et al.*, Nucl. Phys. A **933**, 290 (2014), 1409.4140. 1, 7

[6] K. Hebeler, J. M. Lattimer, C. J. Pethick, and A. Schwenk, Astrophys. J. **773**, 11 (2013), 1303.4662. 1, 7

[7] A. W. Steiner, J. M. Lattimer, and E. F. Brown, Astrophys. J. **765**, L5 (2013), 1205.6871. 1, 7

[8] T. Fischer, M. Hempel, I. Sagert, Y. Suwa, and J. Schaffner-Bielich, Eur. Phys. J. **A50**, 46 (2014), 1307.6190. 1, 7

[9] S. Rafi and Y. K. Gambhir, Proceedings of the DAE Symp. on Nucl. Phys. **58**, 140 (2013). 1

[10] J. M. Lattimer and A. W. Steiner, Eur. Phys. J. **A50**, 40 (2014), 1403.1186. 1, 7

[11] C. J. Horowitz *et al.*, J. Phys. G **41**, 093001 (2014). 1, 11

[12] B.-A. Li and X. Han, Phys. Lett. B **727**, 276 (2013). 1, 7, 8, 95

[13] P. Russotto *et al.*, J. Phys.: Conf. Ser. **420**, 012092 (2013). 1, 11, 15

[14] P. Russotto *et al.*, EPJ Web of Conferences **88**, 00022 (2015). 1, 15, 63, 64, 98

[15] Łukasik, J. *et al.*, Nucl. Instr. and Meth. **A709**, 120 (2013). 1, 16, 17, 19, 22, 96

[16] C. v. Weizsäcker, Physikalische Zeitschrift **96**, 431 (1935). 3

[17] H. A. Bethe and R. F. Bacher, Rev. Mod. Phys. **8**, 82 (1936). 3

[18] G. Royer, Rom. Rep. Phys. **59**, 625 (2007). 3

[19] T. Mayer-Kuckuk, *Kernphysik* (B.G. Teubner Verlag, Stuttgart, 1984). 3

[20] G. Giuliani, H. Zheng, and A. Bonasera, Prog. Part. Nucl. Phys. **76**, 116 (2014). 4

[21] P. Danielewicz, arXiv:0512009[nucl-th] (2005). 4, 5, 95

[22] P. Danielewicz, P. Gossiaux, and R. Lacey, arXiv:nucl-th/9808013 (1998). 5

[23] P. Danielewicz *et al.*, Science **298**, 1592 (2002). 6, 11, 78

[24] C. Sturm *et al.*, Phys. Rev. Lett. **86**, 39 (2001). 6

[25] C. Hartnack, H. Oeschler, and J. Aichelin, Phys. Rev. Lett. **96**, 012302 (2006). 6

[26] W. Reisdorf, arXiv:1307.4210[nucl-ex] (2013). 6

[27] A. Le Fevre *et al.*, Nucl. Phys. A **945**, 112 (2016). 6

[28] J. Piekarewicz, Phys. Rev. C **69**, 041301 (2004). 6

[29] G. Colò, N. Van Giai, J. Meyer, K. Bennaceur, and P. Bonche, Phys. Rev. C **70**, 024307 (2004). 6

[30] C. Fuchs and H. H. Wolter, Eur. Phys. Jour. **A30**, 5 (2006). 6, 95

[31] Z. Xiao, B.-A. Li, L.-W. Chen, G.-C. Yong, and M. Zhang, Phys. Rev. Lett. **102**, 062502 (2009). 6, 13, 83

[32] A. Klimkiewicz *et al.*, Phys. Rev. C **76**, 051603 (2007). 7

[33] V. Baran, B. Frecus, M. Colonna, and M. Di Toro, Phys. Rev. C **85**, 051601 (2012). 7

[34] L. Trippa, G. Colo, and E. Vigezzi, Phys. Rev. **C77**, 061304 (2008). 7

[35] A. Krasznahorkay *et al.*, arXiv:1311.1456[nucl-ex] (2013). 7

[36] P. Danielewicz, Nucl. Phys. A **727**, 233 (2003). 7

[37] Z. Zhang and L.-W. Chen, Phys. Rev. **C90**, 064317 (2014), 1407.8054. 7

[38] D. V. Shetty and S. J. Yennello. 7

[39] M. Huang *et al.*, Phys. Rev. C **81**, 044620 (2010). 7

[40] S. Kowalski *et al.*, Phys. Rev. C **75**, 014601 (2007). 7, 9, 95

[41] R. Wada *et al.*, Phys. Rev. C **85**, 064618 (2012). 7

[42] C. J. Horowitz and A. Schwenk, Phys. Lett. B **638**, 153 (2006). 9

[43] Z.-Q. Feng and G.-M. Jin, Phys. Lett. B **683**, 140 (2010). 11, 13, 95

[44] A. Andronic *et al.*, Phys. Lett. B **612**, 173 (2005). 13, 95

[45] C. Pinkenburg *et al.*, Phys. Rev. Lett. **83**, 1295 (1999). 13, 95

[46] P. Braun-Munzinger and J. Stachel, Nucl. Phys. A **638**, 3c (1998). 13, 95

[47] A. Andronic, J. Łukasik, W. Reisdorf, and W. Trautmann, Eur. Phys. Jour. **A30**, 31 (2006). 13, 74, 95

[48] P. Russotto *et al.*, Phys. Lett. B **697**, 471 (2011). 13, 83

[49] UrQMD Collaboration, http://urqmd.org/, 2014. 13, 77

[50] Q. Li, Z. Li, E. Zhao, and R. K. Gupta, Phys. Rev. C **71**, 054907 (2005). 13

[51] Q. Li *et al.*, J. Phys. G **31**, 1359 (2005). 13

[52] W. Reisdorf *et al.*, Nucl. Phys. A **781**, 459 (2007). 13

[53] W.-J. Xie, J. Su, L. Zhu, and F.-S. Zhang, Phys. Lett. B **718**, 1510 (2013). 13

[54] H. Hong and P. Danielewicz. 13

[55] Y. Leifels *et al.*, Phys. Rev. Lett. **71**, 963 (1993). 15

[56] T. Blaich *et al.*, Nucl. Instr. and Meth. **A314**, 136 (1992). 16

[57] A. Pagano *et al.*, Nucl. Phys. A **734**, 504 (2004). 16, 18

[58] A. Schüttauf *et al.*, Nucl. Phys. A **607**, 457 (1996). 16, 18

[59] D. Sarantites *et al.*, Nucl. Instr. and Meth. **A381**, 418 (1996). 16, 18

[60] P. Pawlowski *et al.*, Nucl. Instr. Meth. **A694**, 47 (2012), 1203.5608. 17

[61] G. Pasquali *et al.*, Nucl. Instr. and Meth. **A301**, 101 (1991). 19, 21

[62] CAEN, *Technical Information Manual Mod. V1724 8 Channel 14 bit 100 MS/S Digitizer*, CAEN publ., , 30 ed., 2014. 21, 25

[63] GSI Multi Branch System, http://www-win.gsi.de/daq/, 2014. 21

[64] GSI Go4, http://www-win.gsi.de/go4/, 2014. 21

[65] C. Ammerlaan, R. Rumphorst, and L. Koerst, Nucl. Instr. and Meth. **A22**, 189 (1962). 23

[66] G. Knoll, *Radiation Detection and Measurement*, 4 ed. (Wiley, 2010), ISBN-13: 978-0470131480. 28, 36

[67] H. Weick, ATIMA, http://www-linux.gsi.de/ weick/atima, 2014. 28, 36

[68] W. S. McCulloch and W. Pitts, Bulletin of Math. Biophys. **5**, 115 (1943). 39

[69] A. K. Jain, J. Mao, and K. Jianchang, IEEE Comput. Sci. & Eng. **29**, 31 (1996). 40

[70] F. Rosenblatt, Psych. Rev. **65**, 386 (1958). 41

[71] T. Kohonen, Biological Cybernetics **43**, 59 (1982). 41

[72] C. Iacono Manno *et al.*, Nucl. Instr. and Meth. **A443**, 503 (2000). 43

[73] H. Kolanoski, Lect Not. Comp. Sci. **1112**, 1 (1996). 43

[74] C. S. Lindsey, B. Denby, and T. Lindblad, http://neuralnets.web.cern.ch/neuralnets/nnwinhep.html, 2014. 43

[75] U. Müller, Nucl. Instr. and Meth. **A502**, 811 (2003). 43

[76] S. Akkoyun *et al.*, J. Phys. G **40**, 055106 (2013). 43

[77] N. Costiris *et al.*, arXiv:nucl-th/0701096 (2007). 43

[78] C. David, M. Freslier, and J. Aichelin, Phys. Rev. C **51**, 1453 (1995). 43

[79] S. Bass *et al.*, Phys. Rev. C **53**, 2358 (1996). 43

[80] F. Haddad *et al.*, Phys. Rev. C **55**, 1371 (1997). 43

[81] B. Bouriquet, *Relaxation en forme et multifragemntation nucléaire*, PhD thesis, University of Caen, 2001. 43

[82] M. Alderighi *et al.*, IEEE Trans. Nucl. Sci. **49**, 1661 (2002). 43

[83] B. Majorovits *et al.*, Eur. Phys. Jour. **A6**, 463 (1999). 44

[84] I. Abt *et al.*, Eur. Phys. Jour. **C52**, 19 (2007). 44

[85] I. Abt *et al.*, Eur. Phys. Jour. **C54**, 425 (2008). 44

[86] P. Cennini *et al.*, Nucl. Instr. And Meth. **A356**, 507 (1995). 44

[87] Z. Cao, L. Miller, and M. Buckner, Nucl. Instr. and Meth. **A416**, 438 (1998). 44

[88] B. B. Esposito, L. Fortuna, and R. A., IEEE Int. Joint Conference on Neural Networks **4**, 2931 (2004). 44

[89] G. Liu *et al.*, Nucl. Instr. and Meth. **A607**, 620 (2009). 44

[90] E. Ronchi *et al.*, Nucl. Instr. and Meth. **A610**, 534 (2009). 44

[91] T. Tambouratzis, D. Chernikova, and P. I., Journal of Artificial Intelligence and Soft Computing Research **3**, 77 (2013). 44

[92] T. Kohonen, Helisinki Univ. Report TKK-F-A601 (1986). 44

[93] R. Jimenez *et al.*, Nucl. Instr. and Meth. **A674**, 99 (2012). 44

[94] CERN ROOT, http://root.cern.ch/, 2016. 50, 87

[95] C. G. Ryan *et al.*, Nucl. Instr. and Meth. **B34**, 396 (1988). 50

[96] J. Łukasik *et al.*, EPJ Web of Conferences **88**, 01017 (2015). 52

[97] Geant4 Collaboration, Geant4, http://geant4.web.cern.ch, 2014. 55

[98] GSI FairRoot, http://fairroot.gsi.de/, 2016. 55, 87, 88, 99

[99] W. R. Leo, *Techniques For Nuclear And Particle Physics Experiments*, 2 ed. (Springer-Verlag, 1994), ISBN 0-387-57280-5. 55

[100] P. Danielewicz *et al.*, Phys. Lett. B **157**, 146 (1985). 65

[101] P. Russotto *et al.*, The ASY-EOS experiment at GSI: investigating symmetry energy at supra-saturation densities, 5th International Symposium on Nuclear Symmetry Energy, Kraków, Poland, 2015. 68, 83, 84, 98, 99

[102] L.-W. Chen, C. M. Ko, and B.-A. Li, Phys. Rev. C **69**, 054606 (2004). 71

[103] Wolter, H.H. *et al.*, EPJ Web of Conferences **66**, 03097 (2014). 71

[104] Z. Chajecki *et al.*, arXiv:1402.5216[nucl-ex] (2014). 71, 78

[105] J.-Y. Ollitrault, arXiv:nucl-ex/9711003 (1997). 71, 74

[106] W. Reisdorf, private communication, 2014. 74

[107] S. Kupny, J. Brzychczyk, J. Łukasik, and P. Pawłowski, EPJ Web of Conferences **88**, 01010 (2015). 74

[108] S. A. Bass *et al.*, Prog. Part. Nucl. Phys. **41**, 255 (1998). 77

[109] Q. Li *et al.*, J. Phys. G **31**, 1359 (2005). 77

[110] Q. Li and M. Bleicher, J. Phys. G **36**, 015111 (2009). 77

[111] Q. Li *et al.*, Phys. Rev. C **83**, 044617 (2011). 77

[112] M. Cozma, Y. Leifels, W. Trautmann, Q. Li, and P. Russotto, Phys. Rev. **C88**, 044912 (2013). 77

[113] V. Baran, M. Colonna, V. Greco, and M. D. Toro, Phys. Rep. **410**, 335 (2005). 78

[114] D. D. S. Coupland *et al.*, arXiv:1406.4546[nucl-ex] (2014). 78

[115] P. Russotto *et al.*, ASY-EOS at GSI: constraining the symmetry energy at supra-saturation densities, In preparation, to be sent to Phys. Rev. C. 83

[116] M. B. Tsang *et al.*, Phys. Rev. Lett. **102**, 122701 (2009). 83

[117] P. Danielewicz and J. Lee, Nucl. Phys. A **922**, 1 (2014). 83

[118] B. A. Brown, Phys. Rev. Lett. **111**, 232502 (2013). 83

[119] Z. Zhang and L. W. Chen, Phys Lett. **B726**, 234 (2013). 83

[120] GSI FairRoot, Git hub repository https://github.com/fairrootgroup/fairroot, 2016. 87

[121] Trac of the Asyeosroot project, https://subversion.gsi.de/trac/fairroot/browser/asyeosroot/trunk/, 2015. 89